NUMERICAL MODELING OF ROCK DRILLING WITH FINITE ELEMENTS

by

Yaneng Zhou

BE in Hydraulic Engineering, Wuhan University, China, 2006

MS in Hydraulic Engineering, Tsinghua University, China, 2009

Submitted to the Graduate Faculty of

Swanson School of Engineering in partial fulfillment

of the requirements for the degree of

Doctor of Philosophy

University of Pittsburgh

2013

UNIVERSITY OF PITTSBURGH

SWANSON SCHOOL OF ENGINEERING

This dissertation was presented

by

Yaneng Zhou

It was defended on

March 21st, 2013

and approved by

Jeen-Shang Lin, ScD, Associate Professor, Department of Civil and Environmental Engineering

Albert C. To, PhD, Assistant Professor, Department of Mechanical Engineering and Materials Science

Isaac K. Gamwo, PhD, Researcher, National Energy Technology Laboratory

Luis E. Vallejo, PhD, Professor, Department of Civil and Environmental Engineering

Qiang Yu, PhD, Assistant Professor, Department of Civil and Environmental Engineering

Dissertation Director: Jeen-Shang Lin, ScD, Associate Professor, Department of Civil and Environmental Engineering

NUMERICAL MODELING OF ROCK DRILLING WITH FINITE ELEMENTS

Yaneng Zhou, PhD

University of Pittsburgh, 2013

Rock drilling is the process employed to retrieve both the conventional and the unconventional resources, such as gas and oil buried deep under the ground. This study attempts to improve the understanding of the interaction between the drilling bit and rock by investigating the mechanics involved. In terms of achieving such a goal, a numerical modeling, if successful, can provide insights that are not possible through either field tests or laboratory experiments.

When the cutting depth progresses from shallow to deep, there is a failure mode transition from ductile to brittle, and a critical depth that governs this transition. This study introduced Bažant's simple size effect law into interpreting the transition process of rock cutting. By treating the cutting depth as a measure of size, the law was found applied well to rock cutting based upon the data available in the literature, and the Finite Element Method (FEM) modeling results. By introducing the concept of characteristic length, this study also reinterpreted the previous understanding of the critical depth in rock cutting, by introducing the concept of characteristic length, and obtained the influence of characteristic length on critical depth through numerical modeling.

The Mechanical Specific Energy (MSE) and the Rate of Penetration (ROP) are two key factors for evaluating the efficiency of a drilling process and together they form a good base for strategizing a desirable drilling operation. In the absence of cutter wear rate, a relationship between MSE and ROP for a rectangular cutter has previously been suggested. This study

presented a simple model for a circular cutter that includes the wear progression, which could explain the laboratory result of cutting high strength rock under high pressure.

The operation of a drilling bit in the field is mainly achieved through circular cutting action. This study extended the previous efforts and modeled first the circular cutting of a single disc cutter. This effort then formed the basis of a full drilling bit modeling presented at the end.

TABLE OF CONTENTS

LIST OF TABLES

LIST OF FIGURES

PREFACE

I am indebted to my advisor, Professor Jeen-Shang Lin. He constantly challenges me with new topics, in addition to training me to deal with problems with insights. Professor Lin also guides me to think deeply and critically throughout my research.

I would like to express my gratitude to members of my thesis committee, Professor Albert C. To, Dr. Isaac K. Gamwo, Professor Luis E. Vallejo, and Professor Qiang Yu, for their invaluable assistance in preparing and reviewing this thesis.

I would like to thank my coworkers in Professor Jeen-Shang Lin's group, Maria C. Jaime, Jorge A. Mendoza, and all my friends in Pittsburgh, for their help and encouragement during my PhD study.

Special thanks are given to my wife and my parents, for their love, support and understanding.

Finally, I would also like to acknowledge the support that made the study presented possible by the National Energy Technology Laboratory of the United States Department of Energy under the RDS contract DE-AC26-04NT41817 and RES contract DE-FE0004000.

1.0 INTRODUCTION

1.1 BACKGROUND

Rock drilling is the process employed to retrieve both the conventional and the unconventional resources, such as gas and oil buried deep under the ground. From the mechanics point of view, it represents a complex interaction among the drilling bit, rock and drilling fluid. This study attempts to improve the understanding of the interaction between the drilling bit and rock by investigating the mechanics involved. Many methods have been used to study the cutting and drilling process, including field test[1], laboratory experiments [2-13], analytical models[13-17], and numerical modeling [17-30]. In terms of getting a better understanding of what happens when a cutter advances against a rock, a numerical modeling, if successful, can provides insights that are not possible through either field tests or laboratory experiments . First of all, a numerical modeling allows one to obtain a comprehensive picture of the stress and strain field, and examine the failure mechanism at play. It also enables the isolation of key parameters and investigation of their roles on the drilling mechanics. To top it off, it is also much cheaper in terms of the cost of analysis. Thus, this study focuses on the development of numerical modeling of rock drilling.

1.2 OBJECTIVES AND METHODOLOGY

The main objectives of this study are to obtain a better understanding of the mechanics of drilling, and to develop a finite element model for a full drilling Polycrystalline Diamond Compact(PDC) bit. This study adopted a ground up approach by building the basic modeling components first, namely, first from slab cutting to groove cutting, then from linear cutting to circular cutting, and finally from a single cutter to a full drilling bit.

The failure mode and the failure mode transition in rock cutting have important practical implications. For instance, an efficient drilling or tunneling operation would dictate that rock be cut away in a ductile mode so as to keep the amount of rock removed minimum; while an efficient mining operation might require the rock be cut in a brittle mode so as to keep the energy of mining minimum. The ductile brittle transition will be studied from the theory and modeling perspectives. For simplicity, the modeling for this purpose is restricted to linear cutting by a single cutter.

During a drilling operation by a drilling bit, each cutter on the bit undergoes a circular motion, and each cutter cuts a groove into a rock. In order to build the components that lead to a credible drilling bit modeling, this study first modeled a groove cut through orthogonal linear cut. This is followed by extending the model to circular cut.

The friction between the drilling bit and the rock may significantly affect the performance of the bit. This friction may be introduced because of the geometry of the cutter or of the bit wear during the drilling. For a new drilling bit, each cutter on the bit is usually chamfered, and the chamfer may increase during drilling under high temperature high pressure (HTHP) environment. How the wear influences the cutting process for a single circular cutter was investigated.

Finally, in an effort to build a virtual drilling machine, a full drilling bit model was built, and some preliminary results were obtained.

1.3 ORGANIZATION OF THE THESIS

This thesis consists of 8 chapters. Chapter 2 presents a selected review of the mechanics of rock cutting and drilling. The review focused on the mechanics of ductile-brittle failure transition, and the implications on the scratch test. Some numerical approaches of rock cutting and drilling were briefly described.

Chapter 3 introduces Bažant's simple size effect law into interpreting the result of rock cutting obtained by FEM modeling. This study first established credence of the continuum damage model in fracture analysis under mode I loading, by comparing its FEM results with those from the cohesive model. The size effect was then modeled for structures with similar cracks using the damage model. Finally, the damage model was extended to rock cutting without pre-existing cracks, and Bažant's simple size effect law was employed in interpreting the result. By treating the cutting depth as a measure of size, this study found Bažant's simple size effect law could explain well the cutting result through numerical modeling based on damage model.

Chapter 4 further interpreted the laboratory cutting data in the literature with Bažant's simple size effect law. This led to a further exploration of a characteristic length measure that has been widely used in the concrete fracture research. With the aid of finite element analysis and few rock cutting test data points, the critical failure mode transition depth was expressed in terms of the rock characteristic length. Further aided by empirical relationships, this critical depth was shown to be a function of rock uniaxial compressive strength.

Chapter 5 focuses on the FEM modeling of groove cutting. 3D effect in groove cutting by a rectangular cutter was modeled and compared to the experiment. The modeling was then extended to circular cutting by a single PDC cutter.

Chapter 6 investigates the influence of the wear on the cutting and drilling performance. A model considering the evolution of cutter wear was proposed for a circular disc cutter, which was an extension of a model for a rectangular cutter with fixed wear length. A simple function form was derived between MSE and ROP, and was evaluated with results from numerical analysis and laboratory tests.

Chapter 7 presents some analytical models and physical tests regarding the mechanics of rock drilling, and some preliminary work on rock drilling by a full drilling bit was presented.

Chapter 8 summarizes main contributions of the thesis and recommendation for future work.

2.0 LITERATURE REVIEW

2.1 INTRODUCTION

There are two important observations regarding linear orthogonal rock cutting in the laboratory obtained by the University of Minnesota group led by Professor Detournay[4-7, 19]. First, rock cutting induced two distinct failure modes. Specifically, rock fails dominantly by crushing in shallow cuts, with cutting depth typically less than 1mm. This mode of failure is referred to as the ductile failure mode. For deeper cuts, a crack initializes, propagates, and dynamic chip occurs. This is referred to as the brittle failure mode [6]. The second important observation is that the Mechanical Specific Energy (MSE), defined as the energy to remove a unit volume of rock [31], is approximately equal to the uniaxial compressive strength σ_c, of rock in ductile failure mode[6, 7]. Here, we have initially reviewed the mechanics governing the failure mode transition.

2.2 DUCTILE TO BRITTLE FAILURE TRANSITION

The phenomenon of ductile to brittle transition is widely observed in rock cutting, in contrary, as well as in other materials and other loading conditions. In the framework of elastoplastic fracture mechanics, the energy is stored or dissipated by volume when plastic failure takes place.

However, the energy required for crack propagation depends on area, thus there must exist a cubic-square scaling effect[18]. Many researchers[6, 17, 19, 32-34] show that there is a material parameter, $G_f E / \sigma_y^2$, in the dimension of length, which controls the cubic-square scaling effect, or the transition from ductile to brittle. Here, G_f refers to the fracture energy, E the Young's modulus, and σ_y a yield strength.

The parameter $G_f E / \sigma_y^2$, or equivalently K_c^2 / σ_y^2, was first recognized by Irwin[34] to measure the crack tip plasticity for metallic material. It was found to be a governing factor for the transition from plane stress to plane strain fracture. Specially, for a steel sample with crack subjected to two-dimensional loading, when the sample width was smaller than $3G_f E / \sigma_y^2$, large fracture process zone was observed, and the plane stress condition dominated. Otherwise, the plane strain condition predominated.

The general importance of the parameter $G_f E / \sigma_y^2$ in ductile-brittle failure transition has been pointed out by Gurney et al. [32]. By studying a number of materials including glass, timber, polymers, and steel, they concluded that for small structure disseminated yielding occur before crack, that is the smaller structure was more ductile because of significant yielding; while for the geometrically similar larger structures with the same material properties, crack occurred before yielding, or the larger structure was more brittle.

Puttick [33] further put forward that the critical length in ductile brittle transition was also a function of test, and the critical length was expressed as $G_f E / \sigma_y^2 \phi$, where ϕ is a dimensional parameter characteristic of the test, in which σ_y is the yield stress in uniaxial test, covering cases both in uniaxial tension and in shear.

Bažant[35, 36] proposed a scaling law for transition from ductile to brittle for concrete, rock and steel. The transition is controlled by a critical structure size $D_0 = G_f E \big/ f_t^2 B^2 k_0^2$, in which f_t is the tensile strength, and B ,k_0 are dimensionless parameters related to geometry shape and loading condition. For geometrically similar structures, when the structure size is smaller than the critical structure size, fracture process zone is significant and the strength theory governs the failure of the structure. The failure mechanism will shift to fracture as the structure size increases.

Richard[6] found the parameter $\left(K_{IC}/\sigma_c\right)^2$, controls the transition from ductile to brittle failure mode in rock cutting. Figure 2.1 is a schematic description from ductile to brittle transition. When the cutting depth is smaller than a critical transition depth d_c, the energy dissipates through the volume of crushed rock. Thus the cutting force is expected to be proportional to the uniaxial compression strength σ_c and cutting depth. Otherwise, the energy dissipates through the area of the crack, thus the cutting force is expected to be proportional to the fracture toughness K_{IC} and the square root of cutting depth.

Huang and Detournay [19], took up a different approach using dimensional analysis and obtained a similar relationship. They defined an *intrinsic length scale*, $l_i = K_{IC}^2 \big/ \pi\sigma_c^2$, and with the aid of discrete element simulation they further proposed that the governing mode of failure is determined by this intrinsic length scale. In essence, they affirmed the earlier results of Richard[6].

Atkins[17] found a relevant length scale, $G_f E' \big/ \tau_y^2$, controled the ductile brittle transition by cutting polymers, where E' is the plain strain Young's modulus, τ_y is the shear yield strength.

Specifically, when the cutting depth is much smaller than $0.1G_f E' / \tau_y^2$, the behavior is ductile; when the cutting depth is much larger than $0.1G_f E' / \tau_y^2$, the behavior is brittle.

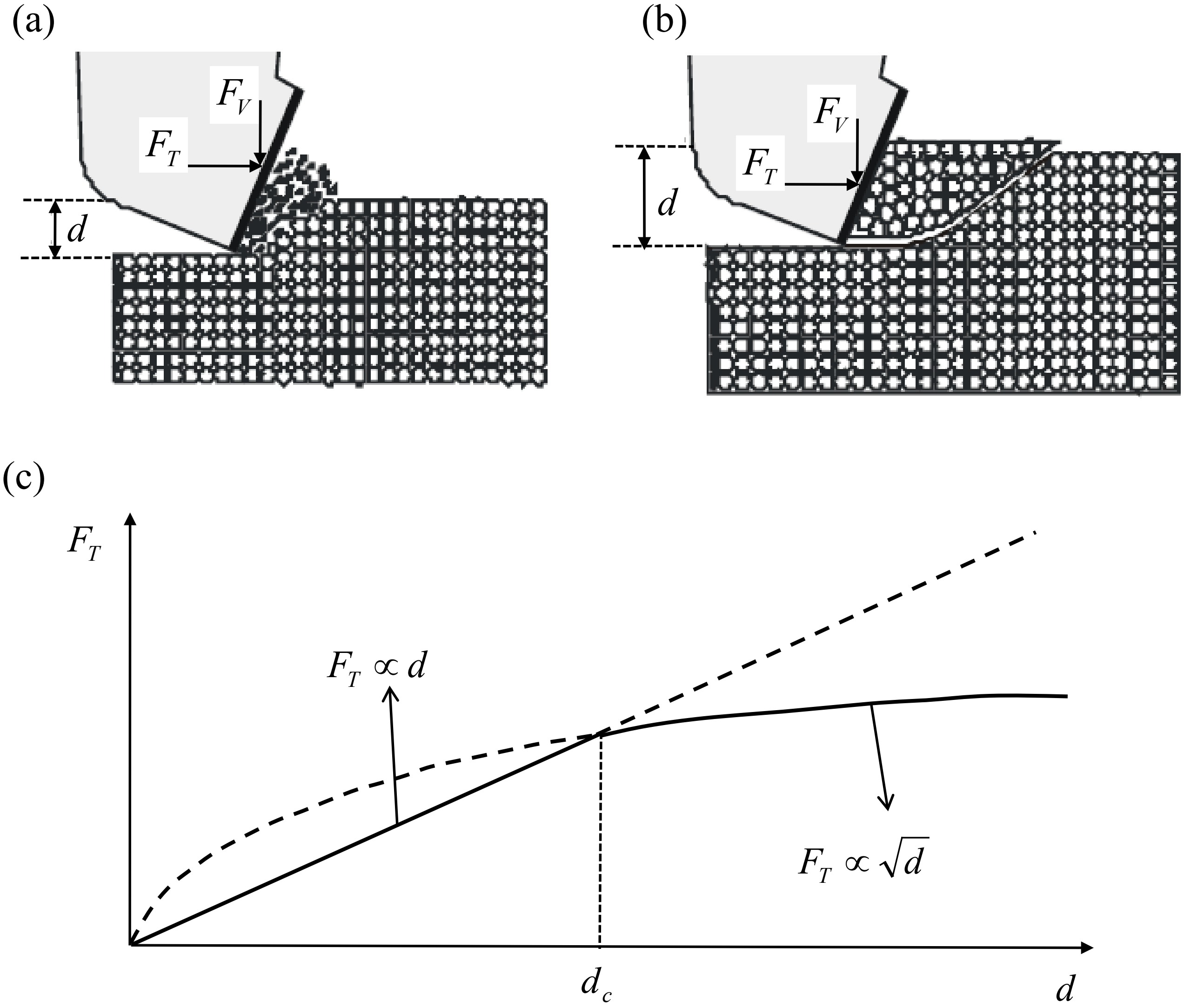

Figure 2.1 Schematic description of transition from ductile to brittle mode (a) energy dissipates through volume in ductile range (b) energy dissipates through crack surface in brittle range (c) relationship between cutting force and cutting depth[6]

2.3 SCRATCH TEST AS A MEANS TO MEASURE ROCK STRENGTH

Detournay and Defournay[15] proposed a 2D phenomenological cutting model for a blunt rectangular cutter, in which the forces applied on the cutting face and the wear face are independent. This cutting model only applies to ductile mode of failure, and using the average of forces along a distance that is far longer than the cutting depth. On the cutting face, the average force is assumed to be proportional to the cutting area. The intrinsic specific energy, ε, is introduced to emphasize that the energy consumed on the cutting face, rather than on the wear face. By plotting the cutting force versus the cutting area, the slope of a linear fit gives the intrinsic specific energy. Such a fit is illustrated in as shown in Figure 2.2[7] .

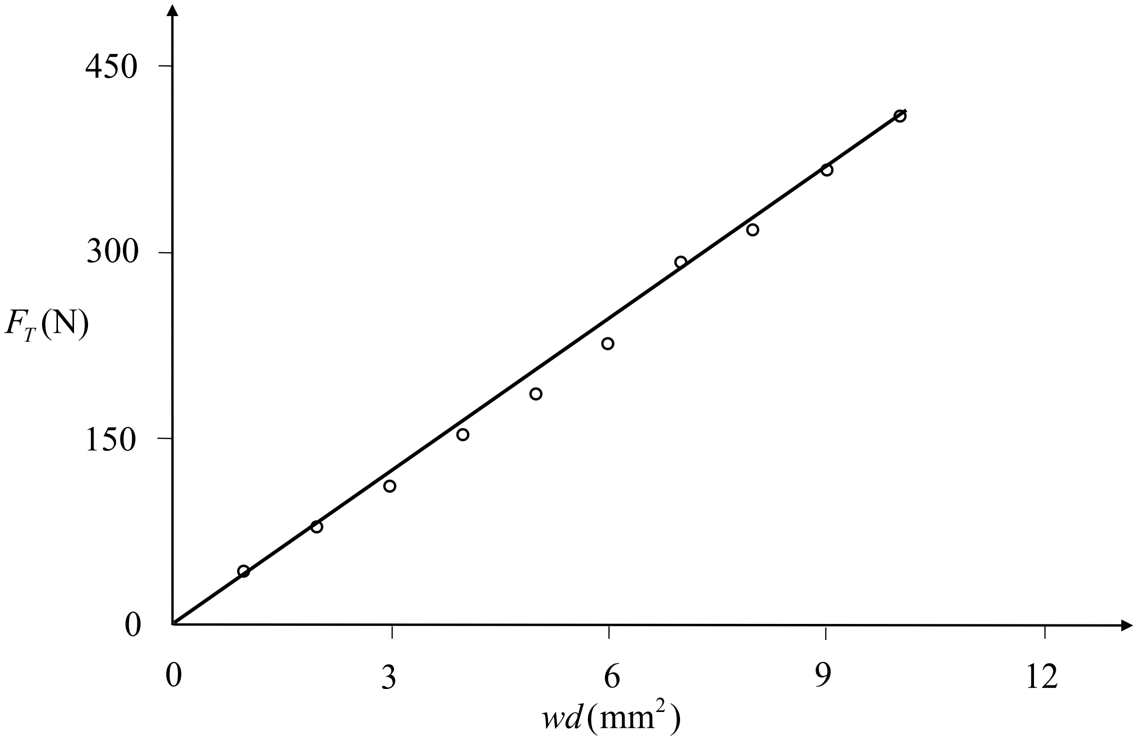

Figure 2.2 Determination of uniaxial compressive strength from scratch test on Lens limestone [7]

When the cutting depth was shallow, typically less than 1mm, the intrinsic specific energy was found approximately equal to the uniaxial compressive strength, σ_c, of sedimentary rocks[6, 7]. Figure 2.3 shows the relationship between ε and σ_c for a wide range of rocks.

The scratch test as a measure of the rock strength was developed based on sharp cutters. However, there is usually a small wear flat area on the edge of cutter even for nominal sharp cutters. This flat area might induce extra force during cutting[6]. Based on Detournay and Defournay's model[15], The total energy *MSE* from a blunt cutter is related to the intrinsic specific energy ε as follows:

$$MSE \approx \varepsilon(1 + \mu l/d) \tag{2.1}$$

where μ is the coefficient of friction in the flat area, l is the wear flat length, the contact stress on the flat area was assumed to be approximately equaled to the intrinsic specific energy.

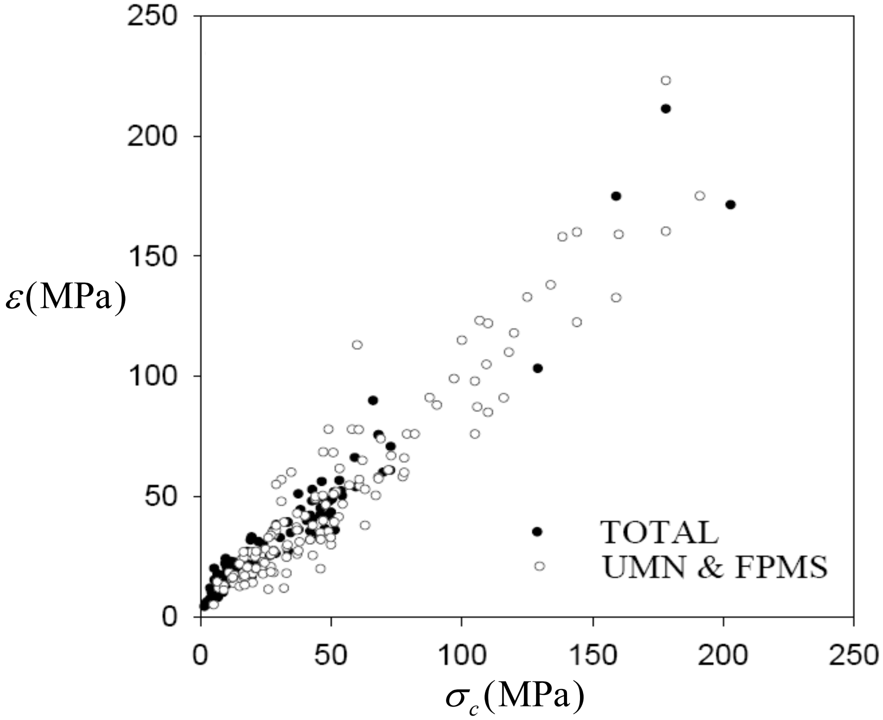

Figure 2.3 Relationship between intrinsic specific energy and uniaxial compressive strength[7]

2.4 NUMERICAL APPROACHES

Numerical modeling of rock cutting and drilling is a complicated task due to a diversity of physical phenomena involved, including the different failure mechanism, tool rock interaction and interaction between separated rocks, complex properties of the rock and downhole conditions, among others[37].

Different ways of cutting are possible, for example: (1) linear cutting versus circular cutting -- a difference in the relative motion between the cutter and rock; (2) slab cutting versus groove cutting -- a difference in the relative width of the cutter and the rock. Most literature was focusing on the modeling of the linear slab cutting, due to its simplicity. Discrete Element Method (DEM) and Finite Element Method (FEM) are the most widely used numerical methods for rock cutting analysis are. Other methods have also been used in the cutting process, such as Finite Differential Method (FDM), Displacement Discontinuity Method (DDM).

Tulu and Heasley[20] adopted the commercial 3D FDM code FLAC^{3D} to simulate circular groove cutting, as shown in Figure 2.4. A special “null’ element was adopted upon reaching failure based on Mohr-Coulomb criterion. This method focused on the interaction between tool and rock within ductile range, where there was no crack propagation and chip formation.

Guo[21] used the DDM to model the crack propagation in linear cutting, as shown in Figure 2.5. A special crack tip element was developed to simulate the crack tip stress singularity, thus the energy release rate and stress intensity factor could be accurately determined at the crack tip. The crack path was determined by the maximum strain energy release criterion[38], or the maximum stress criterion[39]. This study was limited to the initial stage of brittle failure mode, and could not provide dynamic chips, and was not applicable to ductile failure mode.

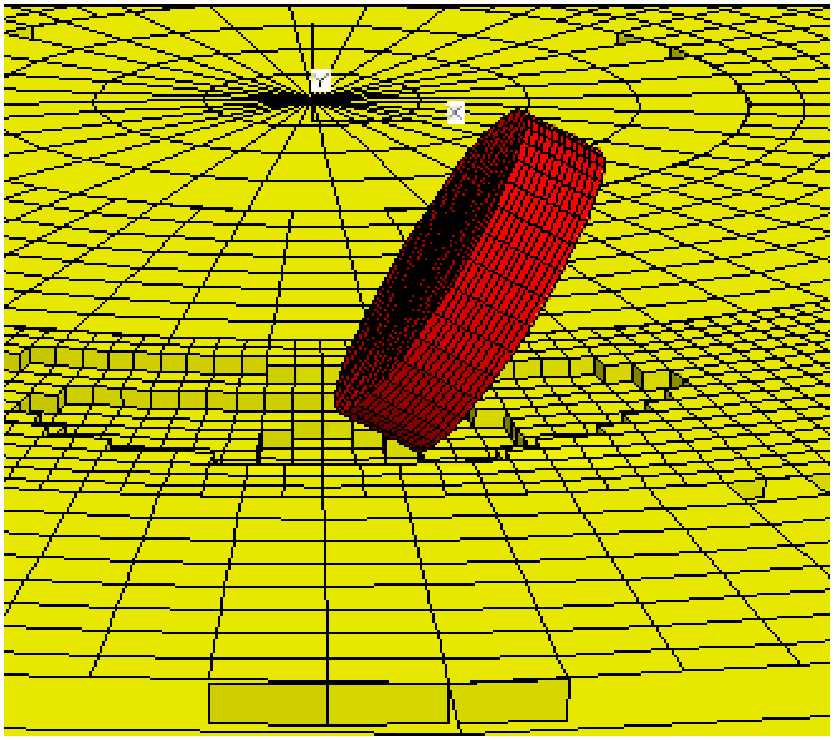

Figure 2.4 Modeling circular groove cutting with FDM[20]

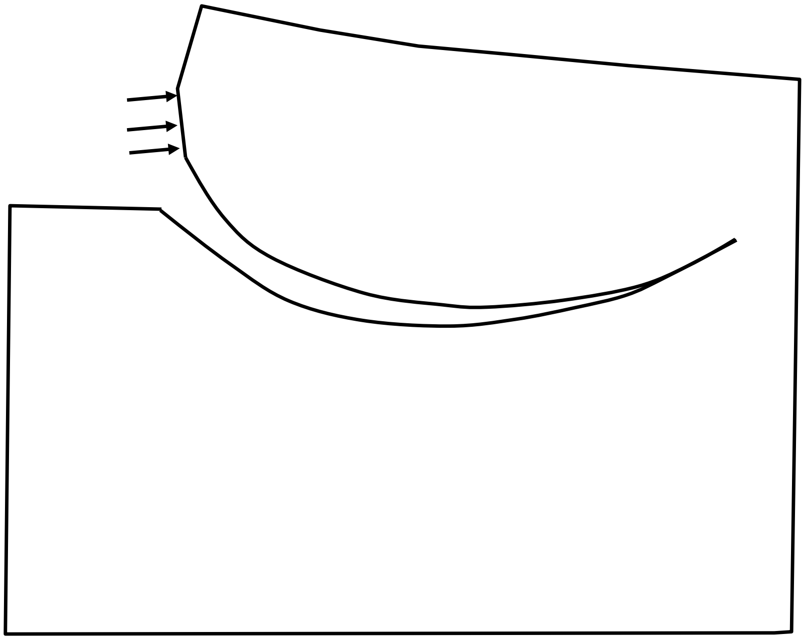

Figure 2.5 Crack propagation in rock cutting with DDM[21]

Huang [22] used a commercial 2D DEM code PFC^{2D} to model the linear slab cutting. Both the ductile and brittle failure mode were duplicated, as shown in Figure 2.6(a), and Figure 2.6(b). Mendoza [23] introduced the crushable particles in rock cutting, by considering the difference of strength of particle size, and concluded that the failure pattern and cutting force would be affected. The linear relationship between MSE and uniaxial compressive strength was also partially reproduced in this study. Lin et al.[24] used a commercial 3D DEM code PFC^{3D} to model shallow linear slab cutting, as shown in Figure 2.6(c). They found the forces obtained were smoother and closer to laboratory tests than those from 2D DEM. As the two failure modes could be well reproduced, and the MSE was well related to the uniaxial compressive strength. Hence, it appears that the DEM has become a mature tool to model rock cutting.

In contrast, FEM modeling is much harder to carry out for it has to resolve a host of difficult problems: the problem of when and how a cutter comes into contact with the rock. The contact problem arises first when the cutter interacts with the rock, followed by the material constitutive problem that determines how the material fails. One of the most challenging problems is how to relate the material failure mechanism to the two failure modes observed in laboratory test is without *a priori* knowledge of the failure mechanism. These problems then repeat during the whole cutting process [29].

Early on, Saouma and Kleinosky[25], Ingraffea [26] used 2D FEM to study the brittle failure of rock cutting, based on Linear Elastic Fracture Mechanics(LEFM). Singularity in the crack tip was considered, and the direction of crack propagation was determined by the maximum energy release criterion, and by the maximum stress criterion, respectively. Figure 2.7 is an illustration of crack propagation under different boundary conditions. Because of the nature of LEFM, these two studies were limited to the initial stage of brittle failure mode, without introducing dynamic chips, and are not applicable to ductile failure mode.

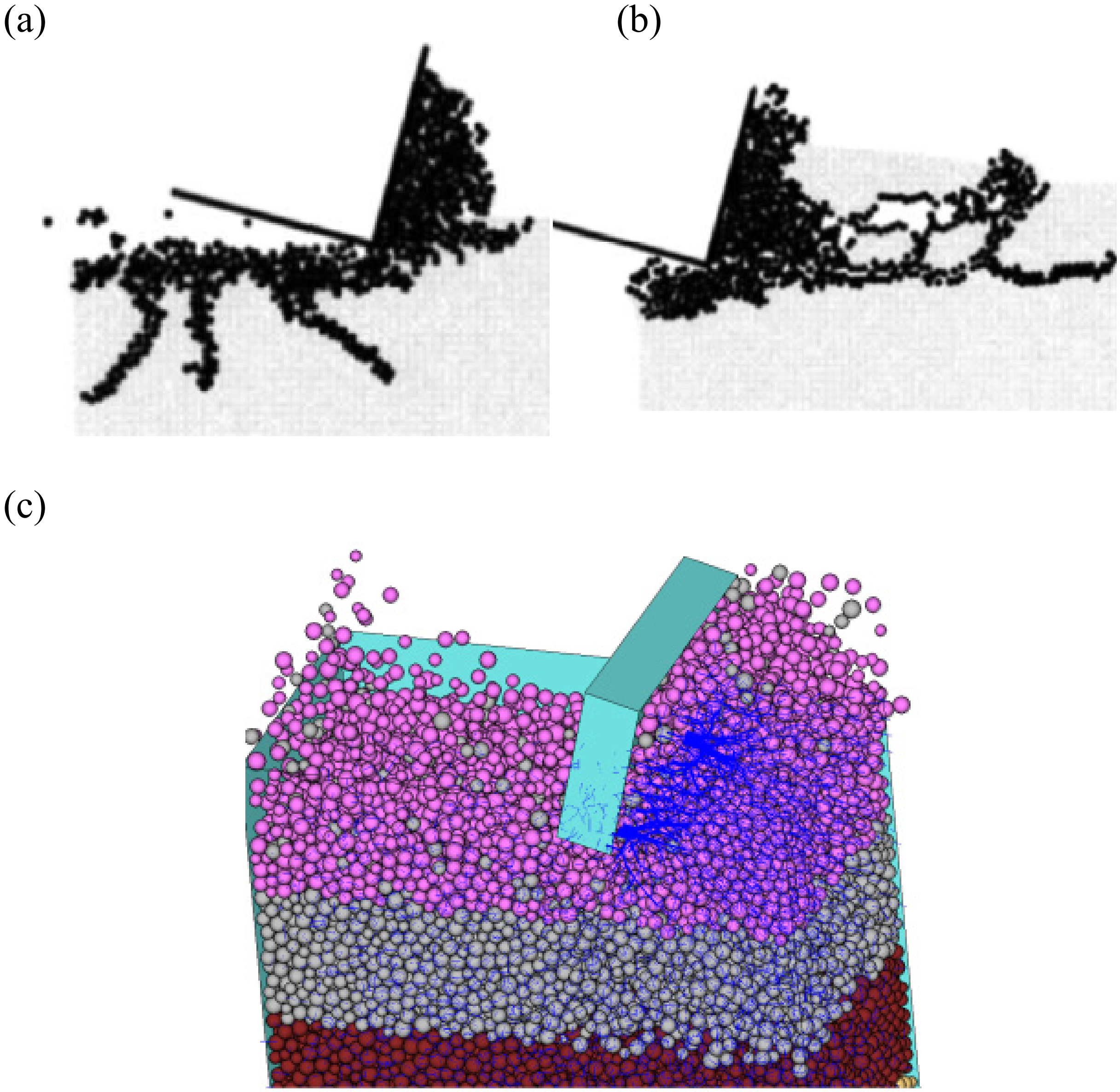

Figure 2.6 Numerical modeling of linear slab cutting with DEM (a) ductile mode with 2D DEM (b) brittle mode with 2D DEM (c) ductile mode with 3D DEM[22, 24]

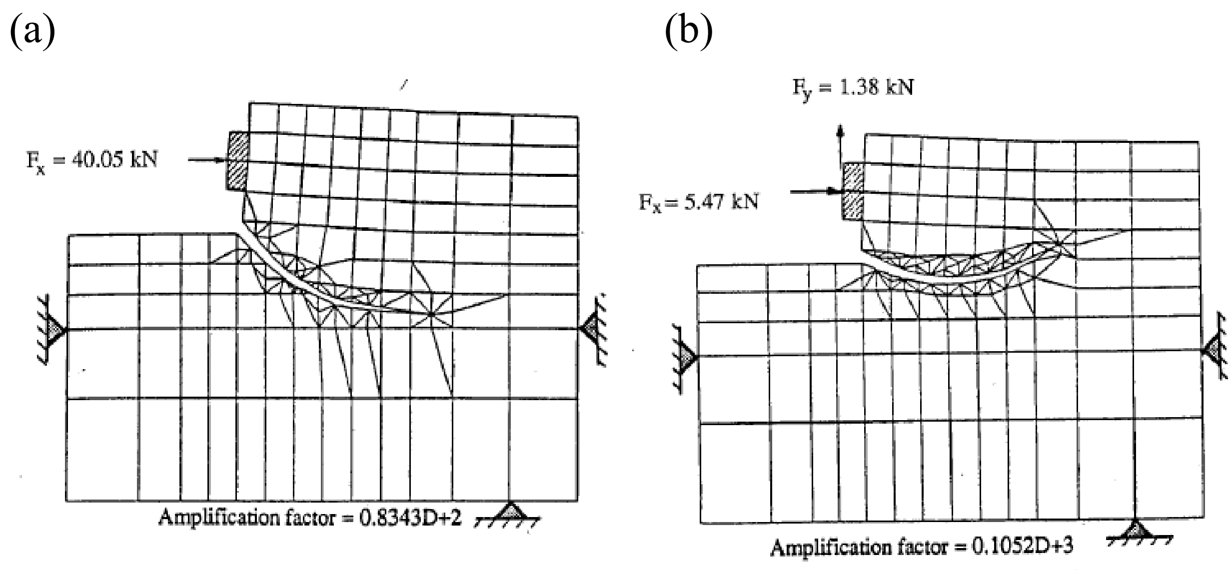

Figure 2.7 Crack propagation with FEM based on LEFM (a) the cutter has only horizontal force, (b) the cutter has both horizontal and upward vertical forces[26]

Liu *et al.* [27] simulated rock cutting with a FEM code R-T^{2D}. This model considered the heterogeneity of the rock material, and the material properties degraded with failure and the degraded materials were highlighted in darker colors, illustrated in Figure 2.8. A smeared crack approach was used, and the modulus was keeping reducing during the failure process of an element. There was no explicit crack or dynamic crack, and this study was limited to the initial stage of cutting.

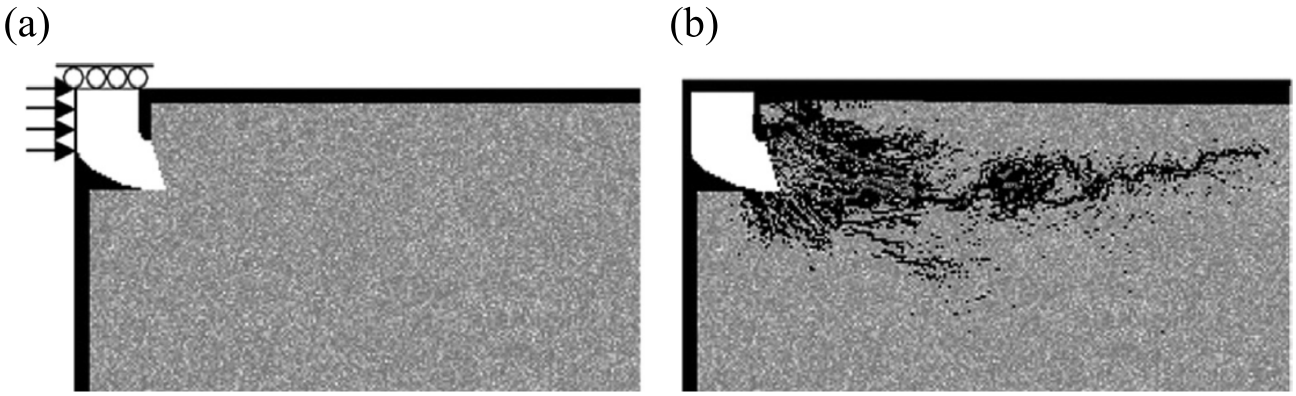

Figure 2.8 Linear rock cuting with 2D FEM based on smeared crack (a) Initial setup, (b) Smeared crack after some advance of the cutter[27]

Yu [28] modeled the continuous mining of coal by a rotary cutting drum with 3D FEM, by using the commercial code LS-DYNA, as shown in Figure 2.9. An element erosion algorithm was adopted, and element was eroded when reaching certain failure criterion. This study showed the force in ductile failure mode, and no crack was presented.

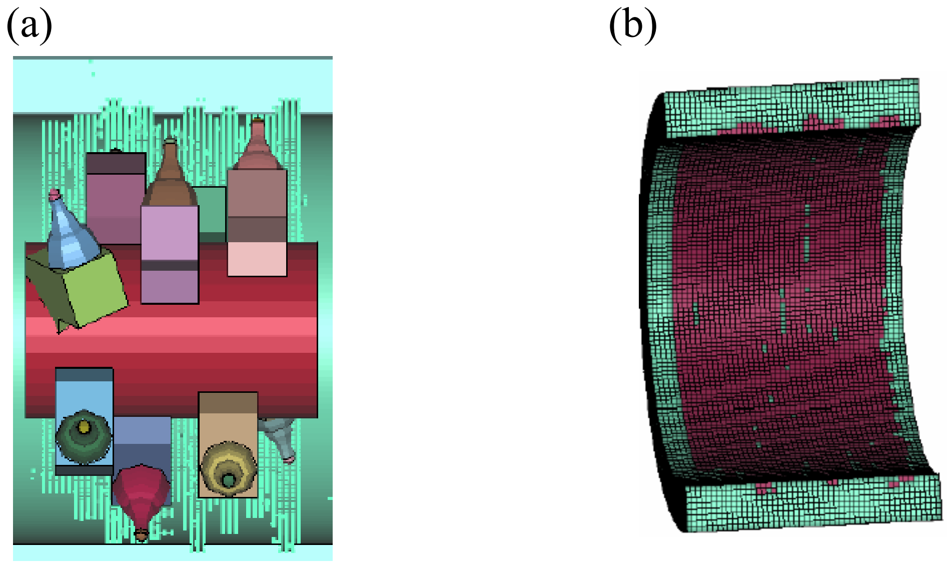

Figure 2.9 Coal mining with 3D FEM (a) A rotary cutter and coal, (b) highlighted elements after cutting[28]

Jaime et al. [24, 29] were the first to reproduce the two failure mode in linear cutting by 3D FEM using LS-DYNA. Specifically, they successfully modeled the crushing failure mode in shallow cutting, and the crack initialization, crack propagation, and dynamic fragmentation in deep cutting, as shown in Figure 2.10. Their study incorporated a robust continuum damage material model MAT159 [40], capable of modeling the elastic and plastic deformation, as well as damage under static and dynamic loading condition. They also found the predicted forces under brittle mode compares well with the laboratory result. However, in ductile mode of failure, their study showed the MSE was approximately constant, but the value was much smaller than the uniaxial compressive strength. This might be attributed to the fact that the erosion algorithm that deletes the rock elements after failure, and the presence of debris of crushed rock in front of cutter [41] could not be well modeled, resulting in smaller estimates of forces.

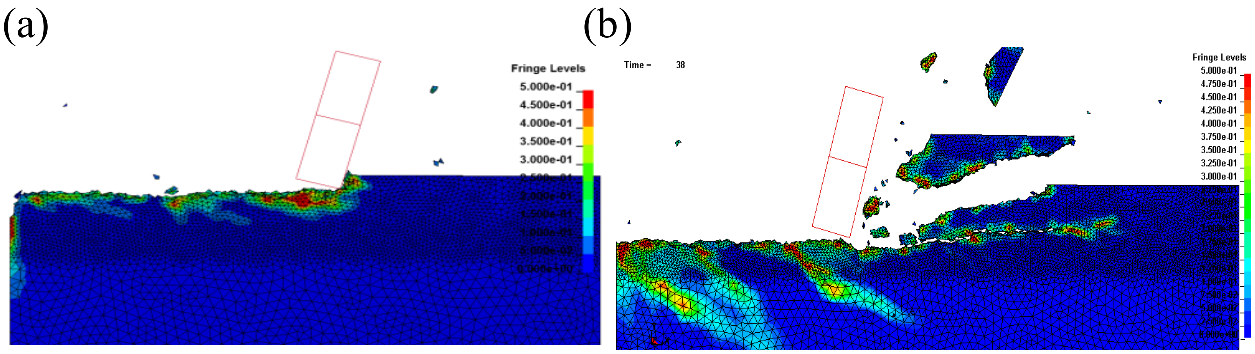

Figure 2.10 Linear slab cutting with 3D FEM (a) ductile mode (b) brittle mode [24, 29]

Fontoura *et al*. [30] also adopted an element erosion criterion to model rock cutting based on commercial code ABAQUS. Both the 2D linear slab cutting and 3D circular groove cutting was conducted, as shown in Figure 2.11. An element erosion algorithm was also used in this study, and it was limited to the ductile mode. Their predicted force pattern and magnitude deviated substantially from the experimentally determined forces. For the mechanical modeling of rock drilling with a full drilling bit, our literature review shows there is as yet no prior work that uses DEM or FEM.

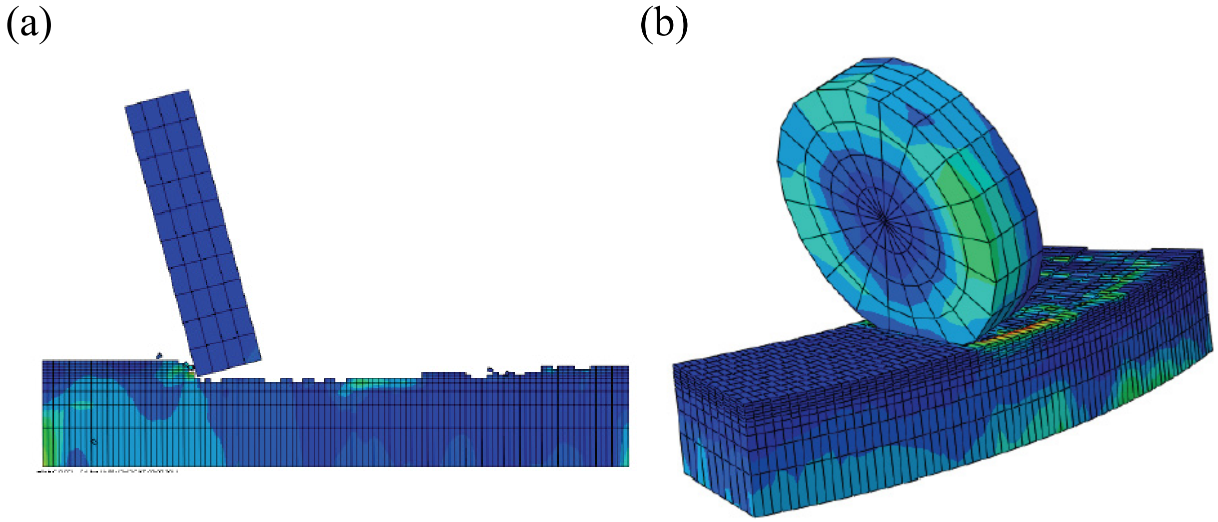

Figure 2.11 Cutting in ductile mode with FEM (a) 2D linear slab cutting (b) 3D circular groove cutting [30]

2.5 SUMMARY

The brittle-ductile failure transition is a widely observed phenomenon in nonlinear elastic fracture mechanics. Several theoretical results show that the transition is controlled by an important parameter associated with the dimension of a problem. The key governing parameter is affected by the fracture energy, Young's modulus, yield strength, geometry and loading configuration. The yield strength in play may be the tensile yield strength, the shear yield strength, or the compressive yield strength depending on loading configurations.

Extensive experiment results have shown that the intrinsic specific energy obtained in a scratch test is well related to the uniaxial compressive strength of rocks, provided that the depth of cut is shallow.

Among the various numerical approaches, the DEM and FEM are the most popular methods to model rock cutting. DEM is able to capture most of the key phenomena in rock cutting. One major down side of DEM is that any material model employed has to be built from a micro level, and thus limits its versatility. Also the size of particles used introduced an artificial length scale into the analysis. As for the FEM modeling, the conventional LEFM and smeared crack based FEM are limited to the brittle mode or to the initial stage of cutting. Continuum damage model based FEM, on the other hand, is able to model both the ductile and brittle mode, capture chips during cutting. Hence, it is adopted in this study.

3.0 MODELING THE SIZE EFFECT OF ROCK CUTTING WITH DAMAGE MODEL

3.1 INTRODUCTION

Fracture process zone exists in the crack tip of quasibrittle material, such as concrete and rock[36]. Under various loading, the strength of quasibrittle material structures has been observed to follow a size effect law. Bažant derived a simple size effect law for quasibrittle material under mode I loading condition[35, 42] in terms of a strength σ_{Nu} is:

$$\sigma_{Nu} = \frac{Bf_t}{\sqrt{1+D/D_0}} \tag{3.1}$$

where *B* is a dimensionless factor related to the geometry of structures and loading configuration, f_t is a tensile strength, D is a characteristic structure size, and D_0 represents the structural transition structure size. The strength σ_{Nu} is defined as the nominal stress σ_N at peak load, and the nominal stress σ_N is determined as:

$$\sigma_N = c_n \frac{F}{bD} \tag{3.2}$$

where F is the applied force, *b* is the thickness of two dimension structure, and c_n is coefficient.

When the structure size is small, the fracture process zone is large in comparison with the crack size, the strength is governed by plastic failure. When the structure size is large, the fracture process zone is negligible with respect to the crack size, and the strength is controlled by fracture [36]. Experiments have shown concrete, mortar, and rocks follow this size effect law, under various loading conditions that, include direct tension and three point bending [36, 42-45].

After some simplifications, the transition size can be related to the material fracture energy and tensile strength[36] as follows:

$$D_0 = \frac{G_f E}{k_0^2 B^2 \kappa f_t^2} \tag{3.3}$$

where G_f is the fracture energy, E is the Elastic modulus, k_0 is a dimensionless parameter related to the energy release rate, $\kappa = 1$ for plane stress condition, and $\kappa = 1 - \nu^2$ for plane strain condition, and ν is the Poisson's ratio.

The phenomenon of ductile to brittle transition is not limited to quasibrittle material under mode I loading condition. Literatures show that it was also observed in other materials, such as steel, polymethyl methacrylate(PMMA) and glass, under different loading conditions besides tension, such as shear, compression, or a more complicated stress condition[6, 17, 19, 32, 33]. A general transition size could be expressed using a general strength measure besides tensile strength as follows,

$$D_0 = M \frac{G_f E}{\sigma_y^2} \tag{3.4}$$

where M is a dimensionless parameter related to the structure geometry and the loading condition, σ_y is a yield strength.

Irwin[34] first recognized the parameter $G_f E / \sigma_y^2$, or equivalently the ratio K_c^2 / σ_y^2, as a measure for the crack tip plasticity for metallic material, and found it to be a governing factor for the transition from plane stress to plane strain. Through studying a series of materials including glass, timber, polymers, and steel, Gurney et al. [32] pointed out its general importance in ductile brittle transition under mode I loading condition. Puttick [33] further put forward that the transition size was not restricted to mode I loading by studying the indentation on PMMA under different temperature. He concluded that the transition size to be a function of tests conducted, and suggested that shear strength might be used for σ_y. Richard[6], Huang and Detournay [19], used the compressive strength as σ_y in the analysis of rock cutting. Atkins[17] used shear strength as σ_y in the study of cutting polymers.

Bažant et al.[36, 46, 47] also derived a similar size effect law and the corresponding transition size for concrete under shear loading condition. In this case, the tensile fracture energy and tensile strength were replaced by the corresponding shear fracture energy and shear strength. The failure mechanism of cutting in brittle regime was generally regarded as mixed mode, as both tensile cracks and shear cracks were involved [17, 27]. The phenomenon of ductile brittle transition in cutting was widely observed in both laboratory test and numerical modeling, and the parameters controlling the transition have been studied [6, 17, 19]. However, there is no prior investigation on the application of such scaling law to rock cutting. Since Bažant's smiple size effect law applied to mode I and mode II condition, there is a good possibility of its application to rock cutting. This study investigated this possibility, and attempted to introduce Bažant's simple size effect law in interpreting the result of rock cutting first through numerical modeling.

A successful modeling of rock cutting requires modeling crack propagation in the brittle regime. The recent advance in singularity modeling using the meshless method[48], or the discontinuity representation using the numerical manifold method[49] have introduced important progress on the modeling of fracture. For quasibrittle materials with substantial fracture process zones during fracture, the cohesive crack model has been found effective in

FEM modeling the fractures[50, 51]. The cohesive crack model is basically an interface model that is placed at the crack tip along a perceived crack path.

However, there is one class of fracture problem for which no prior macro cracks are present. The use of the cohesive crack model for this type of problem becomes tedious: it has to work in conjunction with other numerical techniques, such as remeshing algorithm[52], or the Extend Finite Element Method[53], to keep placing new cohesive zone element as fractures progress. In this procedure, a crack propagation criterion has to be employed to determine the crack propagation direction. This can be problematic. The maximum stress criterion[39] is often adopted regardless of the actual mode of failure. For problems such as rock cutting, the cohesive crack model based on maximum stress criterion is found inadequate because it fails to account for the complexity of the stress environment. On the other hand, the continuum damage mechanics has been found to be useful in the rock cutting application, in which fractures and subsequently fragmentation process were successfully modeled [29].

Unlike the case with the cohesive crack model for which extensive numerical simulations regarding the size effect of concrete have been carried out [51, 54, 55], the credence of continuum damage model has to be established first. For this, the capacity of the continuum damage model in capturing the size effect was first investigated in mode I failure.

A basic question was addressed: How did a continuum damage model compared with the cohesive crack model in terms of fracture modeling when geometrical similar structures each with a crack were analyzed?

After this investigation, the continuum damage model was applied to rock cutting with an aim to see if the results follow Bažant’s simple size effect law.

3.2 A COMPARISON OF COHESIVE MODEL AND DAMAGE MODEL

3.2.1 Theoretical background

In the cohesive crack model[50], the strain softening is expressed as a traction separation curve. The continuum damage model can be viewed as a crack band model in mode I loading condition [36, 56], as the damage is occurs on an element basis and thus is localized within a finite width band. Bažant showed that the soften curve of a crack band model is equivalent to that of a cohesive crack model, if the displacement due to stress softening in the crack band model is regarded as the crack mouth opening displacement in the cohesive crack model. The crack mouth opening displacement, w, as shown in Figure 3.1 [36], can be expressed as:

$$w = h_c \varepsilon^p \tag{3.5}$$

where h_c is the crack band width, and ε^p is the inelastic fracturing strain beyond peak strength in the crack band model.

The inelastic fracturing strain can be extracted from the total stress strain curve by neglecting the nonlinearity before the strength is reached [36], namely:

$$\varepsilon^p = \varepsilon - \sigma / E \tag{3.6}$$

where ε is the total strain, σ is the stress, and E is the elastic modulus.

The fracture energy is defined as the integration of traction separation curve for cohesive model[50], or the integration of stress displacement in the crack band for the damage model [36].When they are set to the same, the equality gives:

$$G_f = \int_0^{\delta_f} \sigma\left(\varepsilon^p\right) dw = h_c \int_0^{\varepsilon_f^p} \sigma\left(\varepsilon^p\right) d\varepsilon^p \tag{3.7}$$

where δ_f is the displacement at final failure, ε_f^p is the fracture strain at final failure.

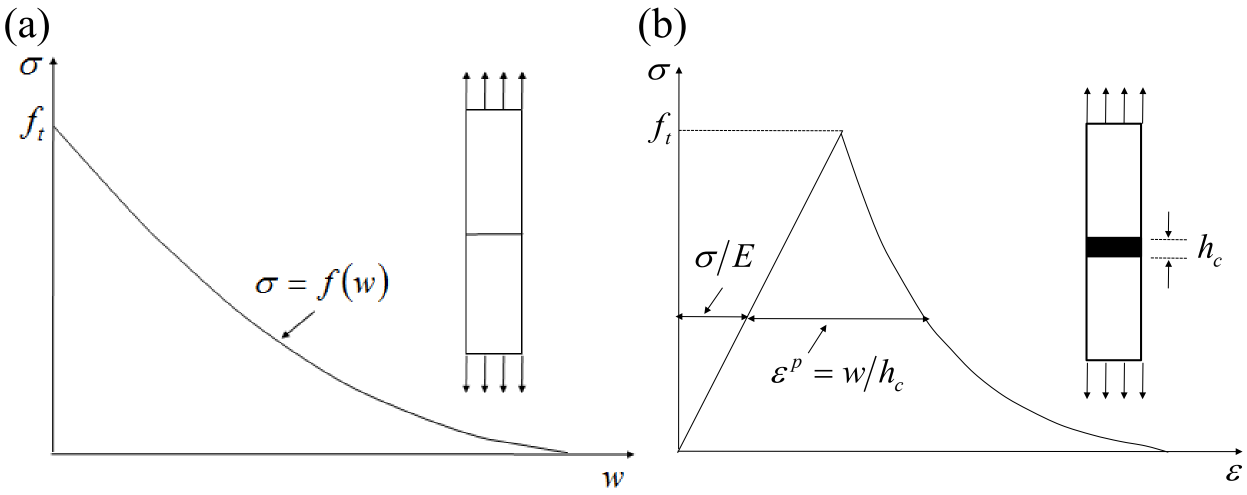

Figure 3.1 Correspondence between cohesive crack model and crack band model (a): cohesive crack model (b): crack band model[36]

3.2.2 Numerical implementation

Both the cohesive crack model and continuum damage model are implemented in the commercial software ABAQUS and LS-DYNA[57, 58]. Both material models are available for mode I, mode II and mixed mode loading conditions, and they have some common material properties: initial stiffness or elastic modulus, damage initialization threshold, and damage evolution properties. For simplicity, the comparison conducted here of the cohesive crack model and damage model was limited to the mode I loading condition. Implementations in the two commercial software were briefly discussed. Emphasis was placed on implementation in LS-DYNA, since this is the code with which the rest of the numerical modeling of the study used.

For the continuum damage model, the most important parameters are the elastic modulus E, the tensile strength f_t, the fracture energy G_f, and the shape of the softening curve. The shape of the softening curve is important, as it governs how the stress drops in the fracture process zone. It could be linear, exponential, and tabular in ABAQUS, and it is quasi-exponential in LS-DYNA.

There is a small deviation regarding the definition of fracture energy in the continuum damage model, i.e., model MAT159 implemented in LS-DYNA, The integration starts not from zero, but from the displacement corresponding to peak strength[40]:

$$G_f = \int_{\delta_0}^{\delta_f} \sigma\left(\varepsilon^p\right) dw \tag{3.8}$$

where δ_0 is the displacement at peak strength.

In this comparison, the continuum damage model used a single layer of cubic element, to represent the potential crack band, namely, the crack band width h_c equals to the element size l. The fracture energy could be expressed as: $G_f = lS_d$,where S_d is the area of stress strain curve after peak strength, as shown in Figure 3.2(a). The difference of the implementation with the original definition could be expressed as $\Delta G_f = f_t^2 l/(2E)$, and it is negligible as long as the mesh size, l , is relatively small.

The shape of the softening curve is defined by a damage parameter *d*, as shown in Figure 3.2(a). The damage *d* increases from an initial value of zero for intact condition towards a maximum value of 1 upon rapture[40].

$$d(\tau_b) = \frac{0.999}{A}\left[\frac{1+A}{1+A\exp^{-C(\tau_b-\tau_{0b})}} - 1\right] \tag{3.9}$$

where *A*, *C* are two constants controling the softening shape. τ_b is an energy type value to track the accumulation of damage, $\tau_b = \sqrt{E\varepsilon_{\max}^2}$. τ_{0b} is a threshold beyond which the damage will accumulate. The nonlinearity before peak strength is negligible for concrete [36], thus, $\tau_{0b} \approx \sqrt{E\varepsilon_0^2}$, where ε_0 is the maximum strain at peak load. The two parameters *A* and *C* are not independent, only parameter A is input, leaving parameter C calibrated automatically by the input fracture energy.

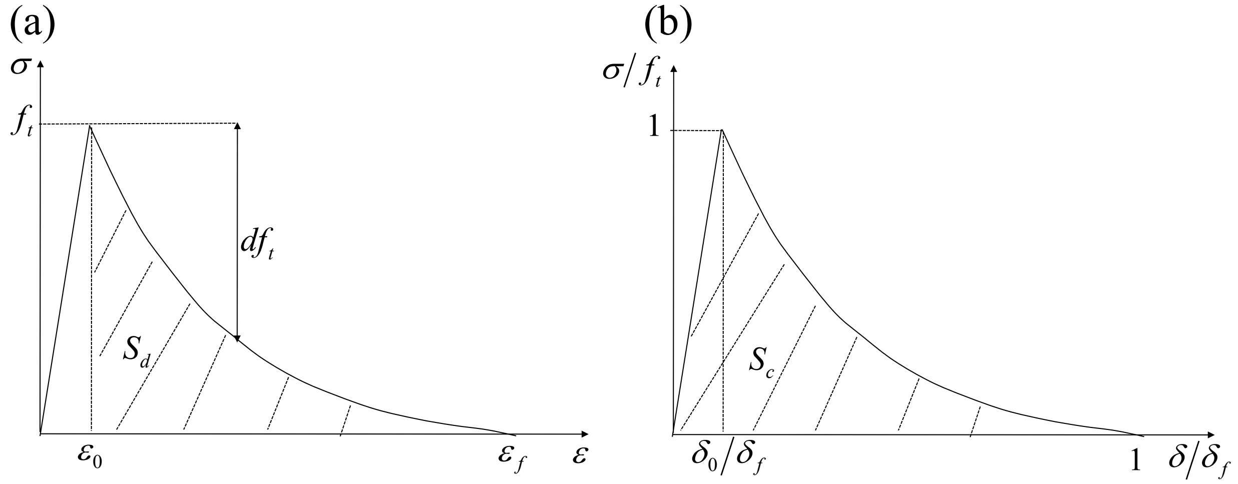

Figure 3.2 Implementation of cohesive model and damage model in LS-DYNA (a): damage model: MAT159 (b): cohesive crack model: MAT186[40, 57]

The cohesive crack model is typically implemented through a traction separation law curve in both ABAQUS and LS-DYNA. Comparing with the continuum damage model, it's the cohesive crack model uses of an initial stiffness K, rather than an elastic modulus E.

In ABAQUS, the cohesive element may have a finite thickness or zero thickness[58]. The zero thickness cohesive element, or interface element, is preferred as the actual physical thickness is usually ill-defined or unknown[59]. In this cases, the initial stiffness K has no physical meaning, as it does not correspond to any measurable physical parameter[59]. K should be infinite to avoid artificially compliance, but a finite value, considered as a penalty, is used in the numerical implementation. The finite value of K provides compliance to the interface element, thus contributes to the overall deformation[60]. Turon et al. [60] proposed a guideline to choose the initial stiffness for the interface element: it should be large enough to ensure the overall compliance, while it cannot be too large to cause numerical instability.

There are several implementations of the cohesive model in LS-DYNA. The implementation for material model MAT186 is discussed herein[57]. Only eight-node solid element with finite thickness is available, and the traction is assumed to be applied on the middle surface. An artificial length scale is introduced by the element thickness. The initial stiffness can be expressed as: $K = f_t / \delta_0$. By neglecting the nonlinearity before peak strength, the fracture energy can be found as: $G_f = S_c f_t \delta_f$. There is a default constraint in the implementation that $\delta_0 / \delta_f \geq 0.01$. Thus for fixed f_t and δ_f, this constraint on δ_0 affect the value K can reach. An alternative procedure was developed to circumvent this problem by modifying the modulus of the material lies next to the cohesive zone.

3.2.3 A calibration procedure

To make the overall compliance not affected by the interface element, Turon et al. [60] suggested an increase the stiffness of the cohesive element itself, and Tomar et al. [61] suggested instead an increase in the elastic modulus of the bulk material on the two sides of interface. For a cohesive element with finite thickness, and with the constraint that limits its initial stiffness, a general procedure is derived here by scaling the elastic modulus of the bulk material.

Consider the case of a plate under uniaxial tension in plain stress condition, in which the thickness of the cohesive zone is t, and the thickness of the adjacent bulk material is T, as shown in Figure 3.3

Before reaching the peak strength, the elastic stress and strain relationship gives :

$$\sigma = E\varepsilon = K\delta \tag{3.10}$$

where σ is the boundary traction, E is the elastic modulus of the bulk material, ε is the strain of the bulk material, δ is the elongation of the cohesive zone.

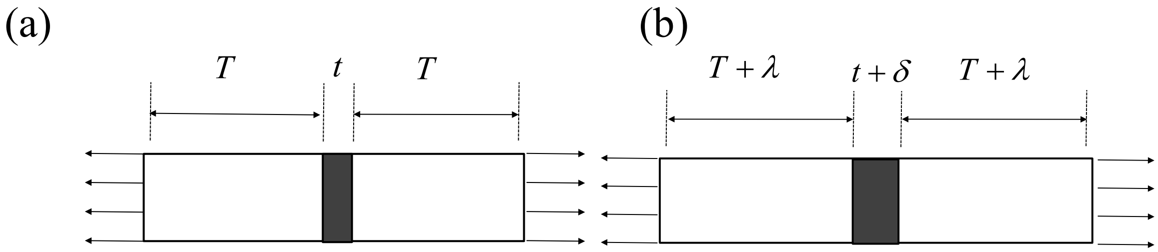

Figure 3.3 Influence of cohesive zone on the overall deformation:(a) initial condition; (b) deformation in the cohesive zone and overall deformation

The overall effective strain of the plate is:

$$\varepsilon_{eff} = \frac{2\lambda + \delta}{2T + t} = \varepsilon \left(\frac{2 + E/KT}{2 + t/T} \right) \tag{3.11}$$

where λ is the elongation of the bulk material on each side.

Thus the overall effective elastic modulus is:

$$E_{eff} = \frac{\sigma}{\varepsilon_{eff}} = E \left(\frac{2 + t/T}{2 + E/KT} \right) \tag{3.12}$$

It can readily be seen that $E_{eff} \approx E$ when K is large and that t is of negligible thickness, as indicated by Turon et al.[60]. For a cohesive zone when the thickness is not negligible, one can simply select $K = E/t$ to give $E_{eff} = E$.

But if the initial stiffness cannot satisfy $K = E/t$ because of constraint imposed, the elastic modulus of the bulk material could be scaled as follows:

$$\overline{E} = XE \tag{3.13}$$

where $\overline{E}$ is the elastic modulus of the bulk material after scaling, and X is a scaling factor.

Thus the overall effective Elastic modulus after scaling could be expressed as:

$$\overline{E}_{eff} = \overline{E}\left(\frac{2 + t/T}{2 + \overline{E}/KT}\right) \tag{3.14}$$

Making the overall stiffness equivalent, i.e., $\overline{E}_{eff} = E$, a scaling factor was obtained:

$$X = \frac{2}{2 + t/T - E/KT} \tag{3.15}$$

This equation is useful as it could be applicable to both zero thickness and finite thickness element, and allows the stiffness of the cohesive element to vary over a wider range without affecting the overall compliance. This calibration procedure was thus adopted in the cohesive model implemented in LS-DYNA.

3.2.4 Numerical study

In order to compare the effectiveness of fracture modeling using the cohesive zone versus the continuum damage models in LS-DYNA, a problem of a simple concrete plate under mode I loading condition was posed with no preexisting crack but with known crack path. The plate was subjected to a uniform tensile stress condition through the application of a uniform end displacement Δ, in a plane stress setting. Figure 3.4 shows the initial set up and the associated FEM mesh. The plate has a size of D=24mm, t=0.5mm, and T=72mm. A single layer of cubic element was used in the middle both for the cohesive crack and the continuum damage models. This layer represents a crack path should one develop. The element size in the middle is the same as the thickness, i.e., *l*=*t*. The material properties of the concrete modeled with the continuum damage model are listed in Table 3.1 [40, 62].

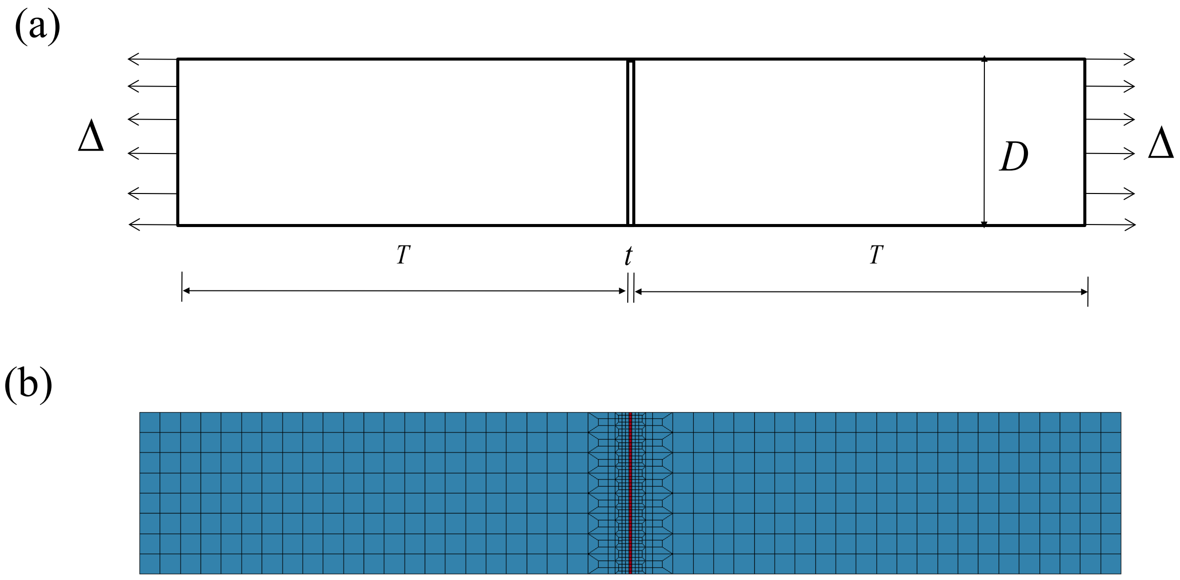

Figure 3.4 A plate under uniaxial tension: (a)initial set up (b) mesh

Table 3.1 Material properties of concrete and rock used in simulation[40, 62-64]

	E(GPa)	v	f_t(MPa)	σ_c(MPa)	G_f(N/m)	A	l_{ch}(mm)
Concrete	29.0	0.15	2.9	38.7	85	0.1	293
Rock	8.3	0.34	2.9	38.7	35	0.001	35

To compare the cohesive crack zone model and damage model, it is desirable to make the material properties the same, including stress displacement curve before and after peak strength. The cohesive zone material model MAT186 requires as input a normalized stress displacement curve, and it was derived from the stress strain curve of the continuum damage model. For this, a uniaxial tension test is conducted on a single element using the continuum damage material model, and the element size used was l=0.5mm. The stress strain curve obtained from FEM analysis is shown in Figure 3.5, with $\varepsilon_0 \approx 1\times10^{-4}$, and $\varepsilon_f \approx 0.3$. From this, the parameters for the cohesive model was derived, i.e., $\delta_0 = l\varepsilon_0 \approx 5\times10^{-5}mm$, and the displacement corresponding to final failure was found to be $\delta_f = l\varepsilon_f \approx 0.15mm$.

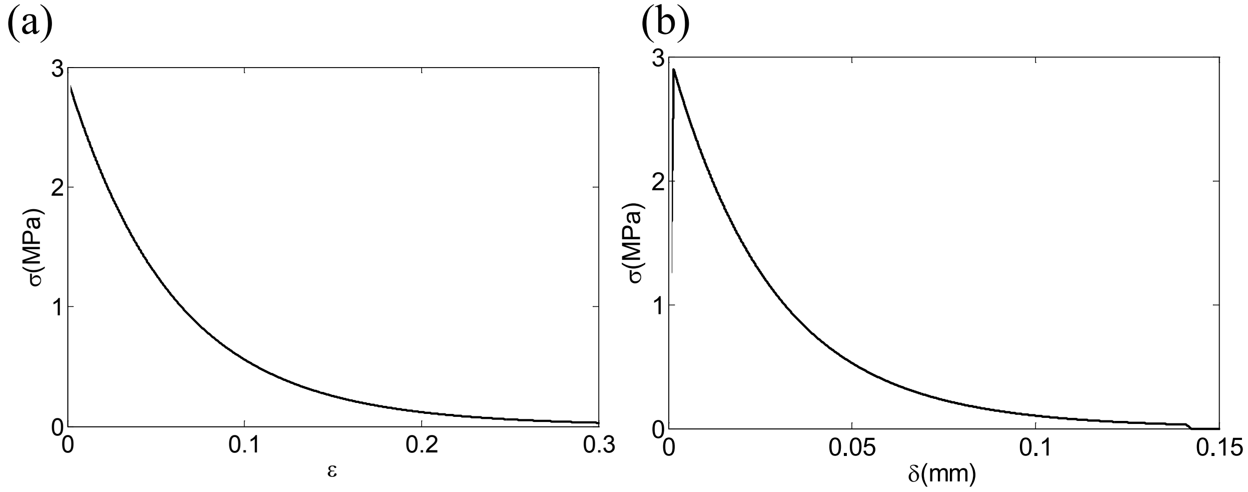

Figure 3.5 Representive curves in the two models (a) Stress strain curve in damage model; (b) stress displacement curve in cohesive model

However, there was a problem: the values of δ_0 and δ_f did not satisfy the default constraint: $\delta_0/\delta_f \geq 0.01$ because δ_0 was too small. The objectives were to set $K = E/t = 5.8\times10^4 N/mm^3$. However, the minimum constraint $\delta_0 = 0.01\delta_f$ gave a much smaller $K = f_t/\delta_0 \approx 1.9N/mm^3$, as shown in Figure 3.5. To overcome this problem, the elastic modulus of the bulk material was scaled based on Eqn. (3.15): $X \approx 1.1$, and the elastic modulus of the bulk material is $\overline{E} = 32.2GPa$. After adopting this calibrating procedure, the overall behavior of the two models matched very well, including behavior pre and post peak strength, as shown in Figure 3.6. Based on the accuracy of the continuum damage model in modeling unnotched concrete structure, this study further extends to model the size effect of notched concrete and rock structure under mode I condition.

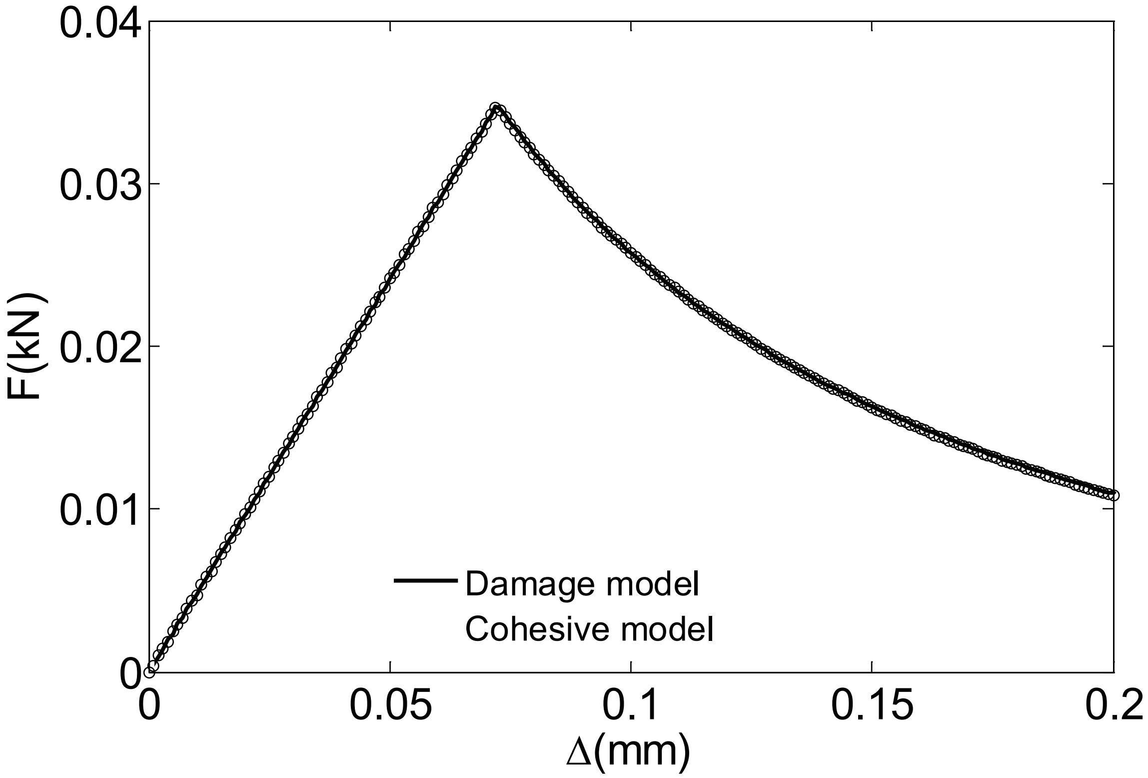

Figure 3.6 Force displacement curve of damage model and cohesive model

3.3 SIZE EFFECT FOR CONCRETE AND ROCK

3.3.1 Size effect for concrete

A plate with a single edge notch was studied under two common loading conditions: direct tension and three point bending. Displacement boundary condition was used to ensure computational stability, and plane strain condition was used to avoid possible warp. The testing configuration and a typical mesh are illustrated in Figure 3.7. The ratio of length over height was kept at *L/D*=6, relative initial crack length, defined as the ratio of initial crack length a_0 over the height of the plate D , i.e., $\alpha_0 = a_0 / D = 0.25$. The potential crack path ahead of the notch tip was modeled by a single column of cubic element with the continuum damage model. The bulk material was modeled by standard eight-node elastic material. The material properties were listed in Table 3.1[40, 62]. The element size for damage model material was kept constant, i.e., l=0.5mm, matching the accuracy requirement of the mesh size in cohesive crack model [54]. For the latter, the mesh size ranged from 0.5mm-1mm in the cohesive element ahead of the notch tip. There was a gradual transition to a larger mesh size into the elastic material to save computation cost.

For concrete, a series of plate with D=24, 48, 96, 192, 384, 768 mm were analyzed, with the maximum size used to be 32 times of the minimum size. As the element size in the middle cross section is kept constant, the corresponding number of element layers varied from N=36 to N=1152. The size effect results for tension and bending obtained are depicted in Figure 3.8. Even through a size effect law was typically applicable only to a range of structure size ratio of 1:20 [36], the simulated data with a larger ratio also fit well, with R^2 of the ratio to be 0.961 and 0.982 for tension and bending, respectively. A fit of Bažant's simple size effect law gave B=0.62, D_0=271mm for tension, and B=1.16, D_0=153mm for bending. The fitted values fall within the typical range in laboratory tests: Bf_t varies between 1.7 to 6.0MPa, and D_0 varies between 36 to 719mm from a variety of concrete, under different geometry shape and loading condition [36].

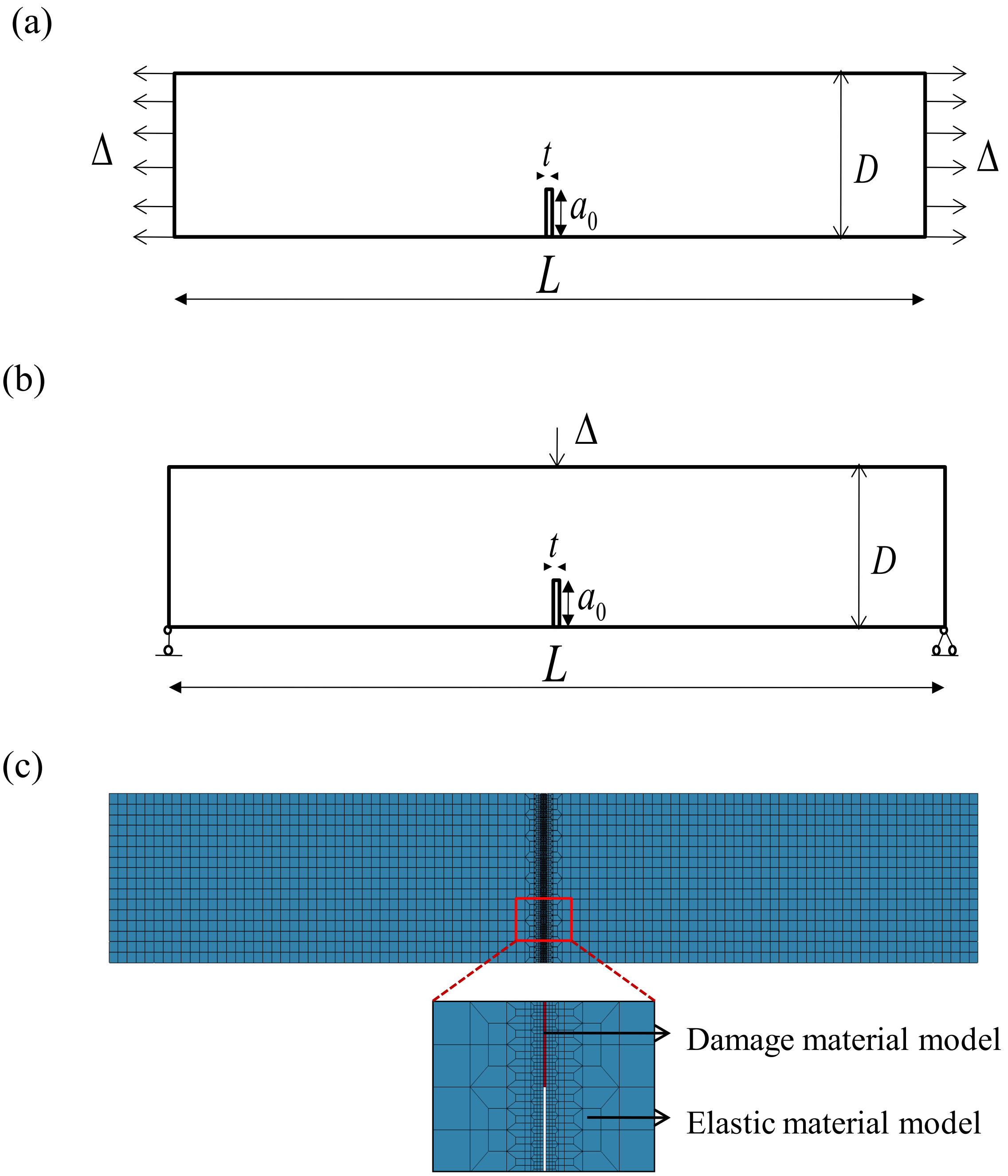

Figure 3.7 Test configurations and typical finite element mesh: (a) Test configuration for tension with single edge notch, (b) Test configuration for three point bending with single edge notch,(c) A typical finite element mesh with D=96mm

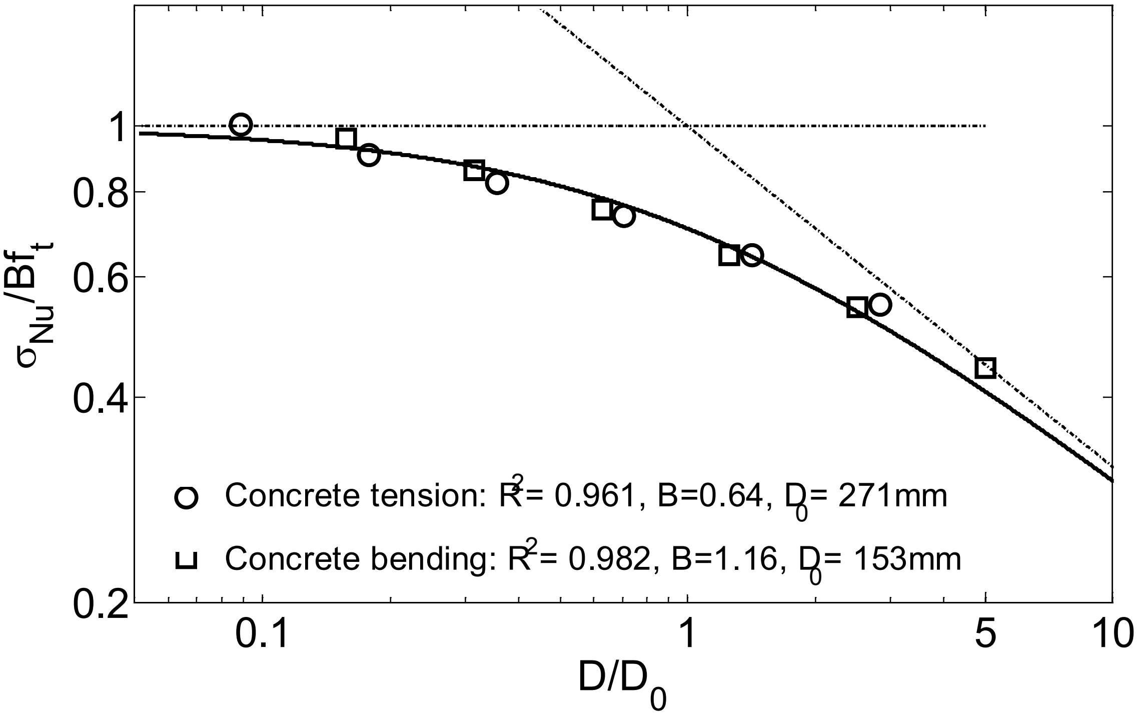

Figure 3.8 Size effect results for concrete under tension and bending

The load deformation characteristics from structure sizes are shown in Figure 3.9(a) and Figure 3.9(b), for tension and bending respectively. It is clear that as the structure size increases, the peak strength decreases, and the stress drops faster in the softening part [36]. Figure 3.9(c) and Figure 3.9(d) show, for tension and bending respectively, that the stress distribution in the middle cross section when the structure reached its peak strength. The range from the location with peak stress to initial notch tip is known as fracture process zone, where the stress decreases with increasing deformation [36]. It is shown that the relative fracture process zone decreases with structure size, indicating a transition from strength theory to linear elastic fracture mechanics.

(a)

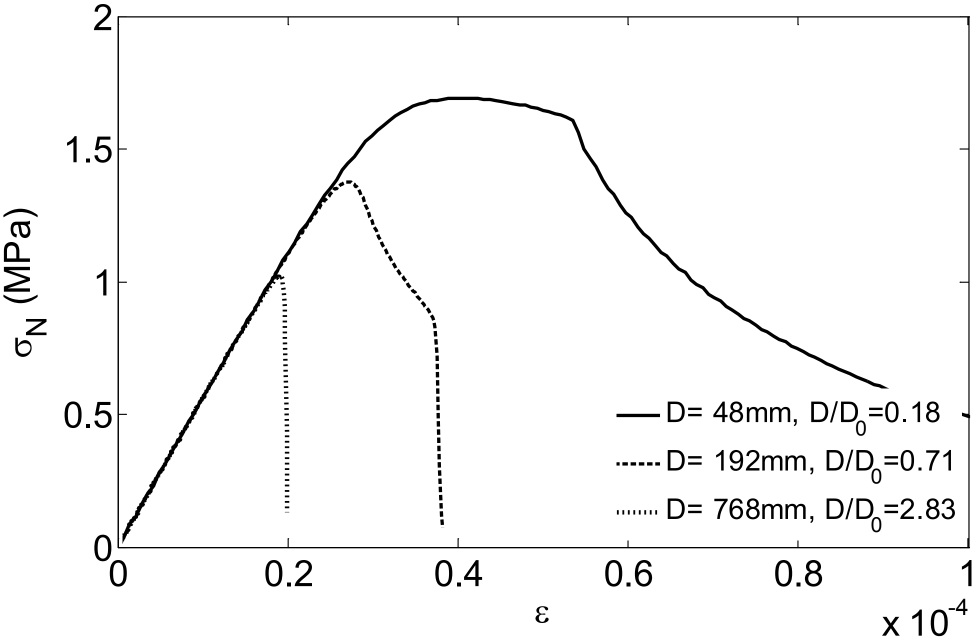

2
1.5
1
0.5
0
σ_N (MPa)
0
0.2
0.4
0.6
0.8
1
ε
x 10^-4
D= 48mm, D/D_0=0.18
D= 192mm, D/D_0=0.71
D= 768mm, D/D_0=2.83

(b)

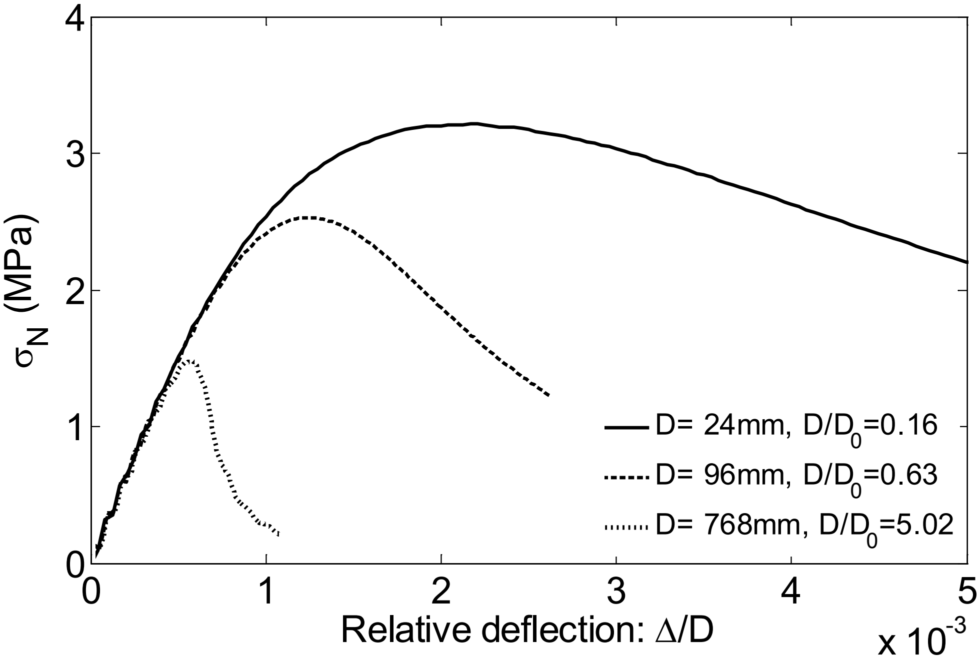

4
3
2
1
0
σ_N (MPa)
0
1
2
3
4
5
Relative deflection: Δ/D
x 10^-3
D= 24mm, D/D_0=0.16
D= 96mm, D/D_0=0.63
D= 768mm, D/D_0=5.02

(c)

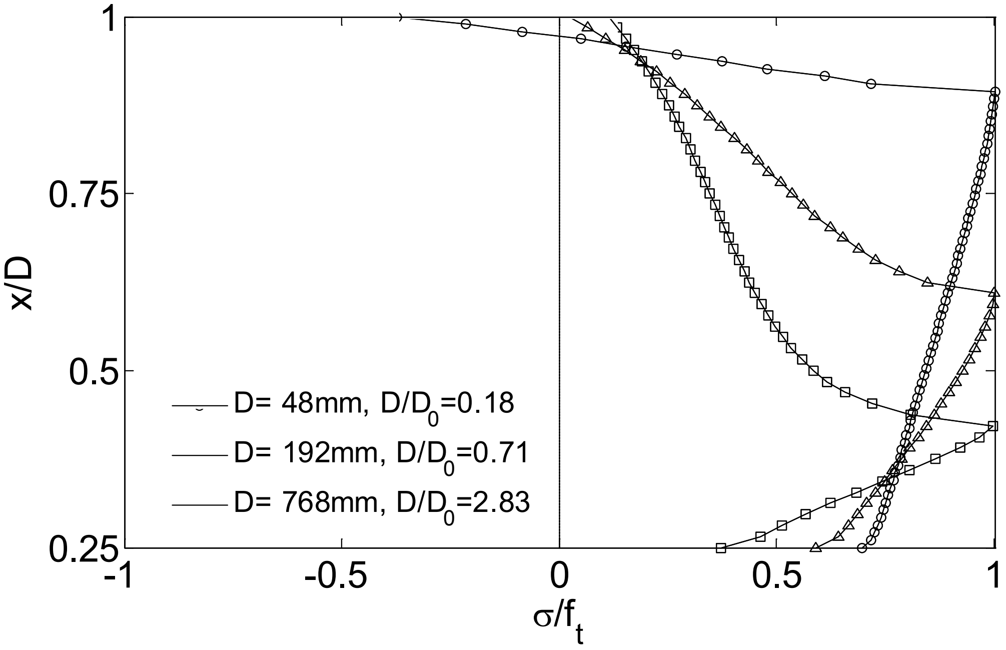

(d)

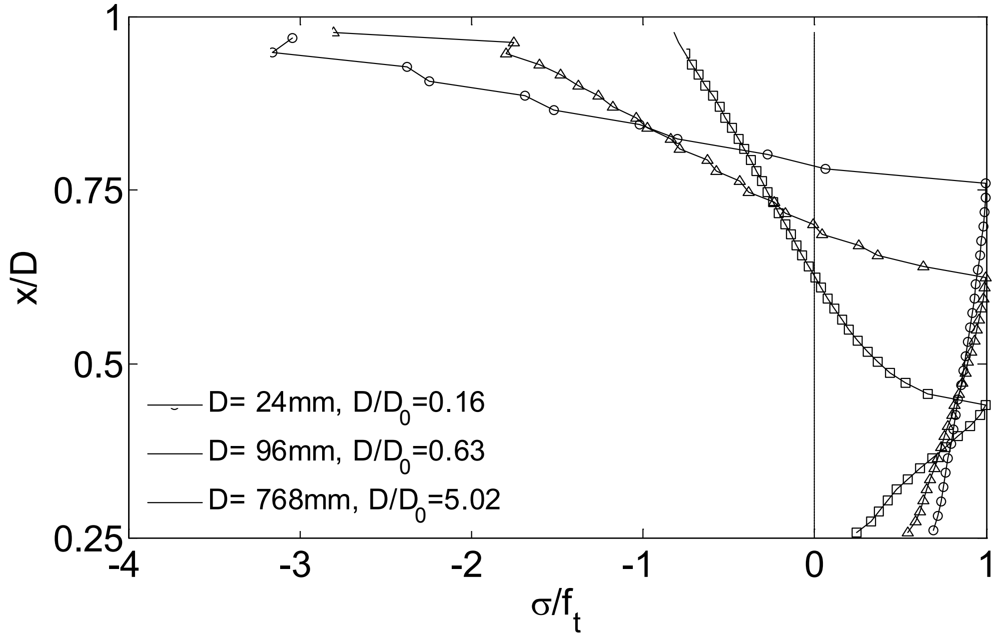

Figure 3.9 Typical stress strain curves, stress relative deflection curves, and stress distribution for concrete: (a) Typical stress strain curves under tension, (b) Typical stress relative displacement curves under bending, (c) Typical stress distribution under tension, (d) Typical stress distribution under bending(normal stress in the middle cross section)

3.3.2 Size effect for rock

Fracture process zone has also been observed in the crack tip of rocks[35]. For example, some experimental results of granite[42, 65, 66], limestone[45] and marble[44] have been found to follow the size effect law, under compact tension and three point bending test.

A soft Vosges sandstone was adopted for size effect simulation under direct tension and three point bending tests. The material parameters are listed in Table 3.1[40, 63, 64]. The geometries and FEM mesh for the rock were similar to that used concrete, except that the mesh size for the continuum damage material was much smaller with l=0.125mm, and the structure size range adopted was D=6,9,12,18,24,36,48,72,96,120mm, corresponding to 36 to 720 elements in the middle cross section of the FEM model. The size effect results for tension and bending are presented in Figure 3.10. These results were again fit well again with the Bažant's size effect law having a R^2 of 0.969 and 0.984 for tension and bending, respectively. The fitting gave B=0.61, D_0=68mm for tension, and B=1.10, D_0=39mm for bending. Some available experiment data showed Bf_t range from 3.3 to 5.1MPa, and D_0 range from 35 to 47mm for rocks under three point bending test [36].

The detailed load deformation characteristics of different structure sizes are shown in Figure 3.11(a) and Figure 3.11(b), for tension and bending respectively. Similar to the results for concrete, the structure is weaker and more brittle with an increasing in the structure size. Figure 3.11(c) and Figure 3.11(d) show the stress distribution in the middle when the structure reaches peak strength, for tension and bending respectively. The relative fracture process zone again decreases with structure size. Compared with concrete, the fracture process zone is much smaller for rock with the same testing configuration and structure size, reflecting a much smaller characteristic length for rocks. For example, when the structure size D was 48mm, the fracture process zones under tension test were approximately 31mm and 15mm, for concrete and rock, respectively, while their characteristic length were 293mm and 35mm.

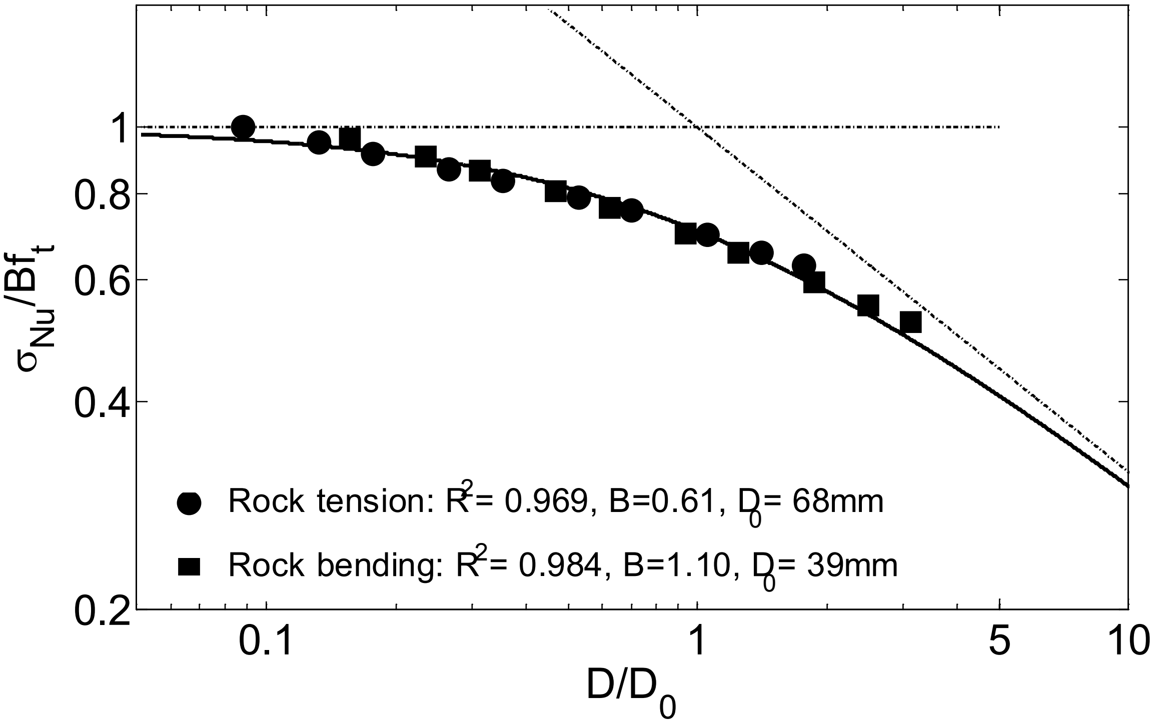

Figure 3.10 Size effect results for rock under tension and bending

(a)

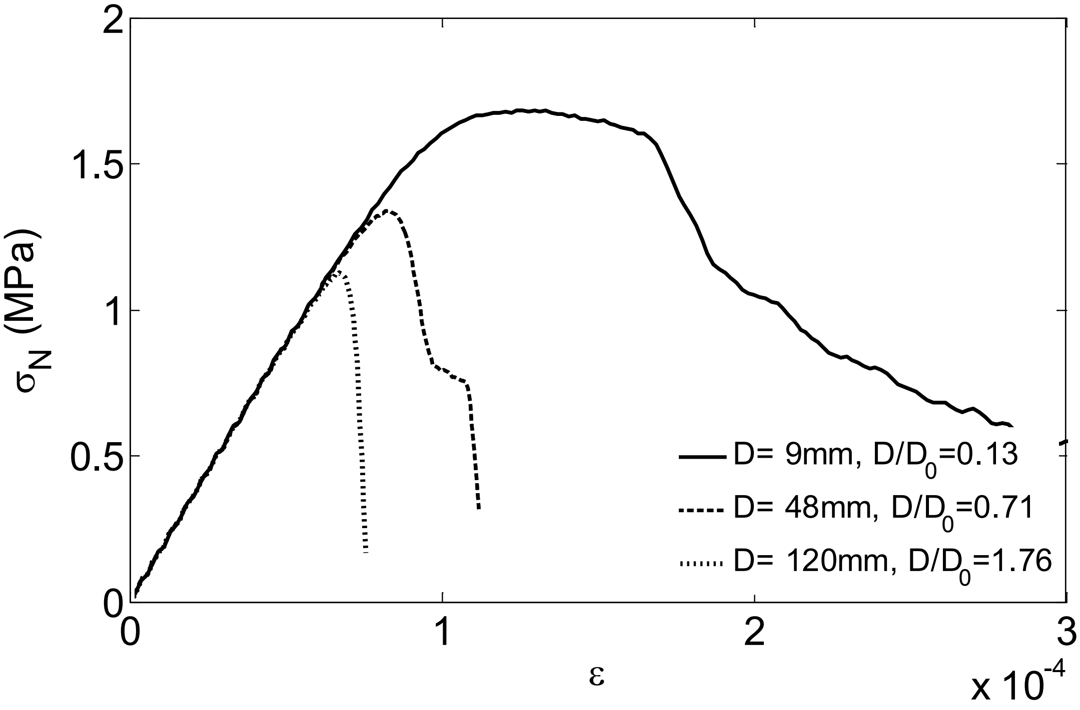

2
1.5
1
0.5
0
σ_N (MPa)
0
1
2
3
ε
x 10^{-4}
D= 9mm, D/D_0=0.13
D= 48mm, D/D_0=0.71
D= 120mm, D/D_0=1.76

(b)

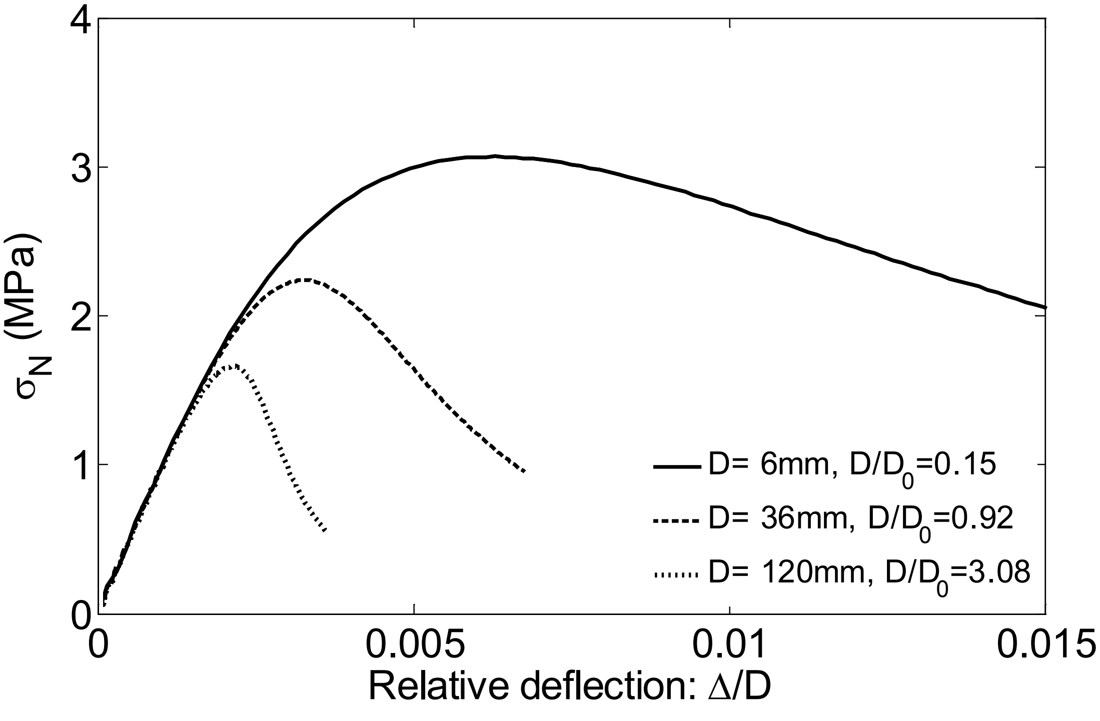

4
3
2
1
0
σ_N (MPa)
0
0.005
0.01
0.015
Relative deflection: Δ/D
D= 6mm, D/D_0=0.15
D= 36mm, D/D_0=0.92
D= 120mm, D/D_0=3.08

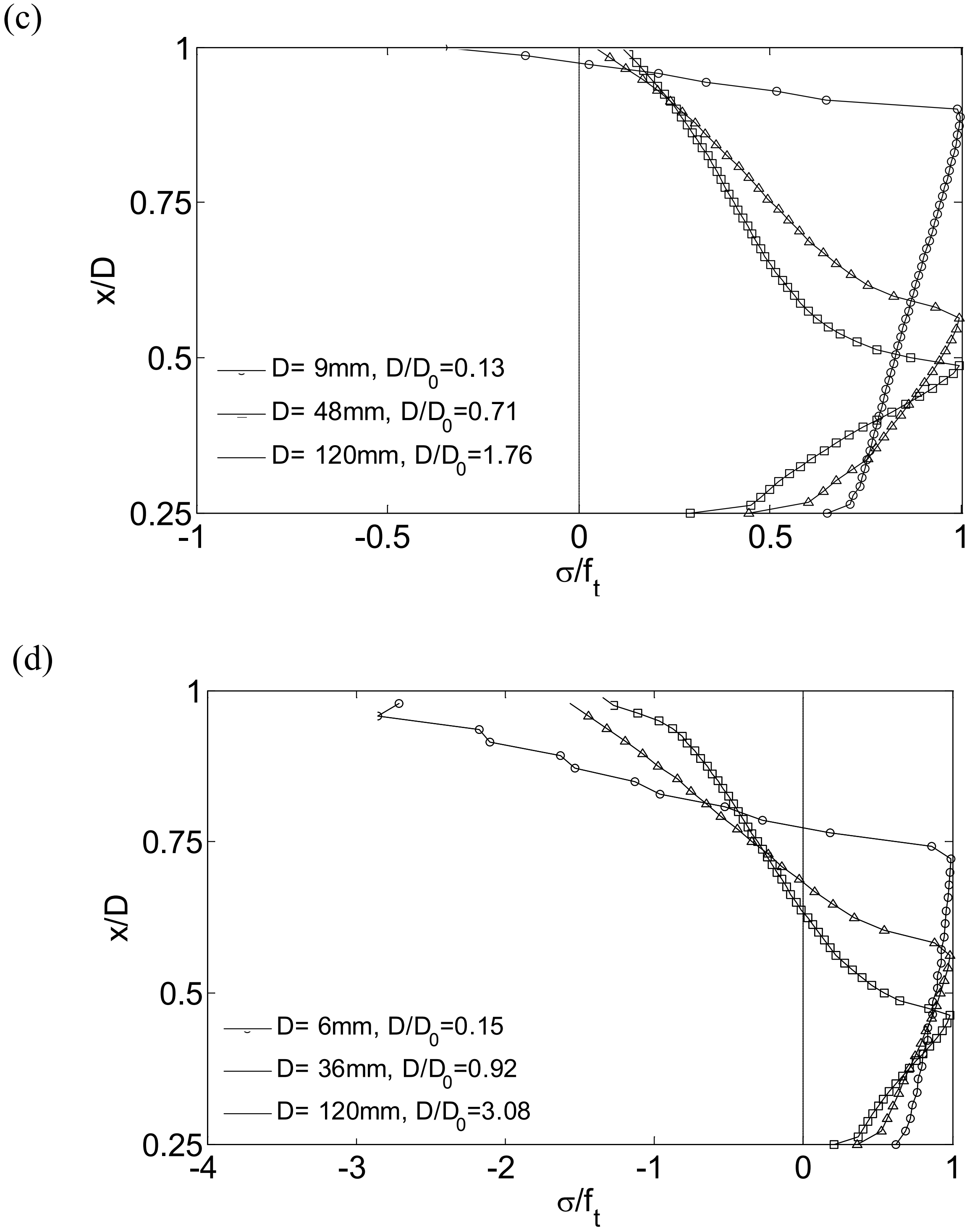

Figure 3.11 Typical stress strain curves, stress relative deflection curves, and stress distribution for rock:(a) Typical stress strain curves under tension, (b) Typical stress relative displacement curves under bending, (c) Typical stress distribution under tension, (d) Typical stress distribution under bending

3.3.3 Size effect independent of geometry

To facilitate the comparison of test results with different geometry shape and loading configuration, Planas and Elices[67], and Bažant, Kazemi and Gettu[68] independently introduced the concept of an intrinsic size:

$$\overline{D} = \frac{D}{2k_0^{'}/k_0} \tag{3.16}$$

where k_0 is a dimensionless parameter related to energy release rate for different geometry in LEFM[36],

$$k_0 = k(\alpha_0) = K_{IC} \Big/ \left(\sigma_{Nu}\sqrt{D}\right) \tag{3.17}$$

where K_{IC} is the fracture toughness, and $k_0^{'}$ is the derivative of k_0 at $\alpha = \alpha_0$.

For the problem studied here, the values used are listed in Table 3.2[69, 70].

Table 3.2 Dimensionless parameter related to energy release rate for different geometry[69, 70]

	Tension with single edge notch	Three point bending with single edge notch
k_0	1.33	0.91
$k_0^{'}$	5.26	2.36

The relationship between nominal fracture toughness and fracture toughness in large size range can be expressed as [36]:

$$\frac{K_{IC}^2}{K_{IN}^2} = 1 + \frac{c_f}{\overline{D}} \tag{3.18}$$

where, K_{IC} can be expressed as $\sigma_{Nu}\sqrt{D}k(\alpha_{ec})$, with α_{ec} represents a relative equivalent crack length for quasibrittle material, $\alpha_{ec} = \alpha_0 + c_f / D$., K_{IN} is a nominal fracture toughness, $K_{IN} = \sigma_{Nu}\sqrt{D}k(\alpha_0)$, and c_f is a limiting constant of critical crack extension for large size structure

Eqn. (3.18) shows that the nominal fracture toughness approaches the fracture toughness for large size structure. As both c_f and $\overline{D}$ are independent of geometry shape and loading configuration, Eqn. (3.18) is useful for checking results from different geometries [36]. Figure 3.12(a) depicts the size effect results for concrete and rock under tension and bending expressed in the form of intrinsic size. The results of tension and bending follow a similar trend for concrete, indicating the size effect is independent of loading configuration. Similar phenomenon was also observed for rock under tension and bending. This result compared well with the size effect result obtained by cohesive crack model, as shown in Figure 3.12(b), for concrete with different geometry shape and loading condition[71].

Eqn. (3.18) could also be expressed in the following form that is independent of geometry [42, 68]:

$$\overline{\sigma}_{Nu} = \frac{\overline{B} f_t}{\sqrt{1+\overline{D}/\overline{D}_0}} \tag{3.19}$$

where $\overline{\sigma}_{Nu} = \sigma_{Nu}\sqrt{2k_0k_0^{'}}, \overline{B} = B\sqrt{2k_0k_0^{'}}, \overline{D}_0 = c_f$ in the large size range.

Figure 3.13 shows the size effect study results for both concrete and rock under tension and bending after normalization. The results under tension and bending were combined for the same material and then fitted by Eqn. (3.19). The R^2 obtained was 0.970 for concrete and 0.972 for rock. The results fitted from combining tension and bending FEM results, compared well with the result by fitting tension and bending results separately, as listed in Table 3.3. As $\overline{B}, \overline{D}_0$ are material properties that should be independent of geometry, and the values of fitted three sets of $\overline{B}, \overline{D}_0$ were close for the same material, confirmed this point.

(a)

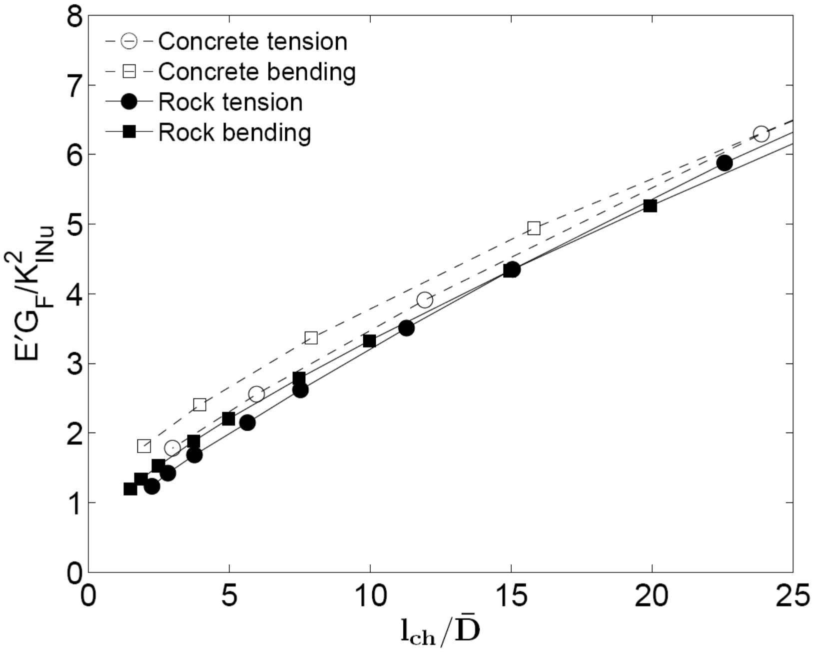

(b)

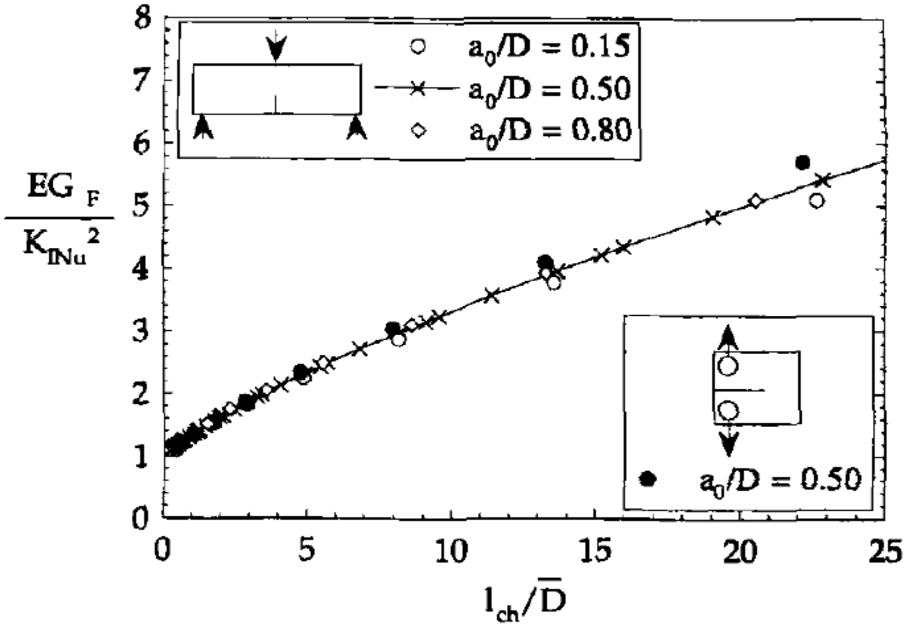

Figure 3.12 Size effects curves with different geometry expressed as a function of intrinsic size:(a) Size effects curves for concrete and rock under tension and bending, (b) Size effects curves for concrete with different geometries [71]

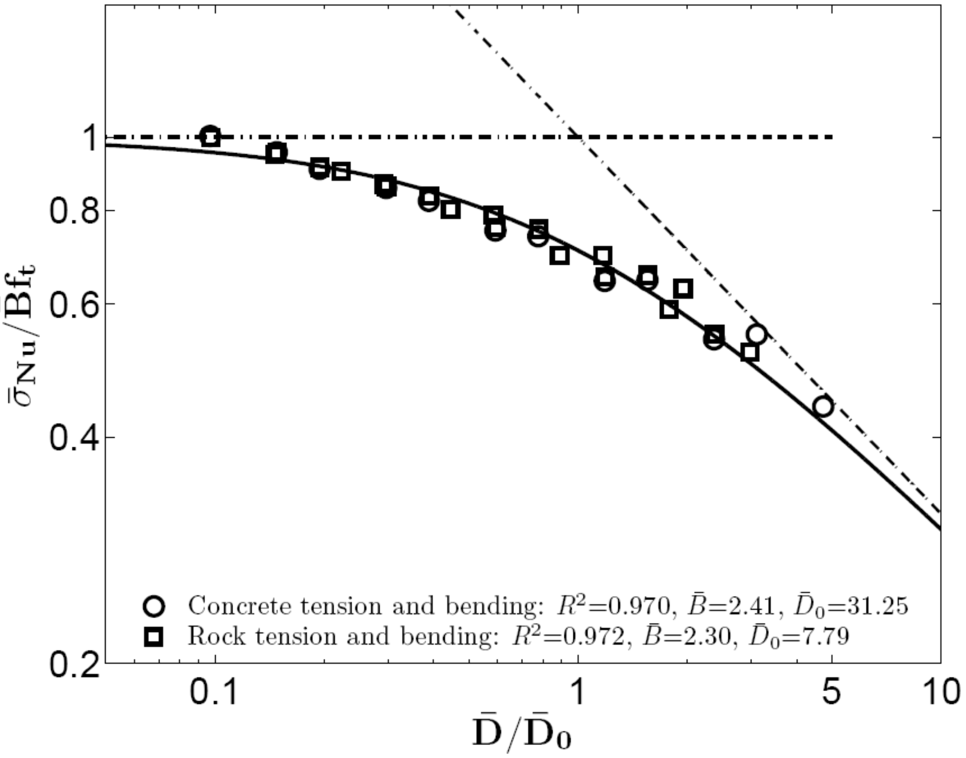

Figure 3.13 Size effects curves for concrete and rock under tension and bending after renormalization

Table 3.3 Regression results of concrete and rock independent of geometry

	R^2	$\bar{B}$	$\bar{D}_0(mm)$
Concrete tension	0.961	2.40	34.24
Concrete bending	0.982	2.39	29.51
Concrete tension and bending	0.970	2.41	31.25
Rock tension	0.969	2.29	8.62
Rock bending	0.984	2.28	7.43
Rock tension and bending	0.972	2.30	7.79

3.4 SENSITIVITY ANALYSIS

3.4.1 Mesh size sensitivity

For elastic material model, it is not difficult to get objective result by refining the mesh. However, it has been a challenging issue for softening material model. Bažant[72] indicated that a straightforward incorporation of stress strain relationship in FEM implementation gave mesh sensitive results, as smaller elements lead to smaller fracture energies, making fracture easier to occur. Recent study pointed to the use of the fracture energy as a material property. To minimize mesh size sensitivity, the softening branch was adjusted according to element size so that the same fracture energy would be maintained[50, 56, 73].

In the FEM formulation, one may first substitute the crack band width h_c with the element size *l*, and the fracture energy becomes:

$$G_f = h_c \int_0^{\varepsilon_f^p} \sigma(\varepsilon^p) d\varepsilon^p = l \int_0^{\varepsilon_f^p} \sigma(\varepsilon^p) d\varepsilon^p \qquad (3.20)$$

The mesh size sensitivity could then be minimized by adjusting the stress strain curve after peaks, to maintain the constant fracture energy for different element size *l*.

This scaling was implemented in MAT159[40, 57], also included is the triaxiality in more complicated stress state.

Figure 3.14 illustrated the stress displacement curves of concrete scaled by different mesh sizes, it is clear that there is only a small variation in the resulting softening curves even though the element sizes used were more than 100 times apart. To facilitate a comparison of the softening shapes, the original stress strain curves were converted to stress displacement curves based on Bažant's crack band model[56]:

$$w = l\left(\varepsilon - \frac{\sigma}{E}\right) \tag{3.21}$$

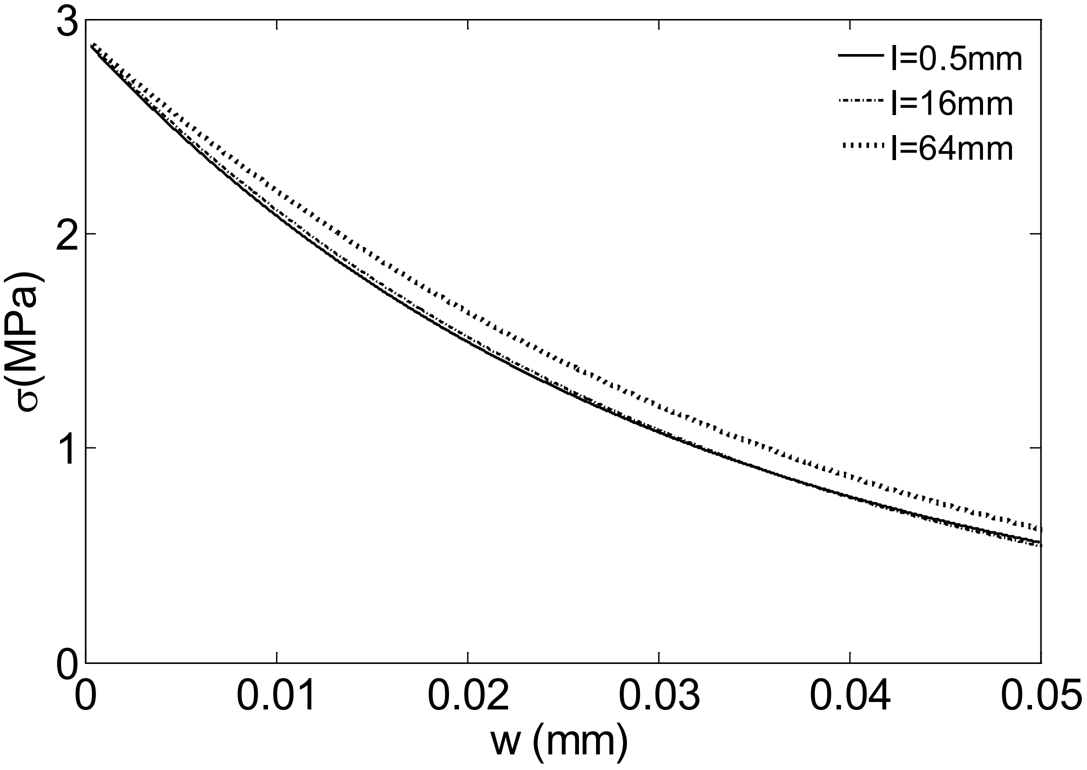

Figure 3.14 Softening curves of concrete with different mesh size (G_f=85Pa.m, A=0.1)

As the stress displacement curve of a single element is insensitive to the mesh size after scaling, larger elements might be acceptable.

It has been widely accepted that there is a minimum number of element that is required to accurately represent the stress distribution, in the cohesive zone using the cohesive crack model,. However, there is no consensus on the detailed number required: Moes and Belytschko[53] suggested the element size should be smaller than one tenth of the characteristic length, based on the work of Carpinteri et al.[74]; Tomar et al. [61] claimed that the element size should be much smaller than the size of cohesive zone, and suggested at least ten elements in a cohesive zone. Camanho et al. [75] and Turon et al. [60] used at least three elements in the cohesive zone. Most previous work was focusing on the required number of elements in the fracture process zone for a problem with a fixed structure size. This leaves an unsolved problem that how many elements are required in the whole cross section to model the size effect, especially that the fracture process zone is not known in advance for a given size of structure.

In this study, the influence of the number of elements was analyzed for a wide range of concrete structure sizes, based on the tension test of concrete. Besides the very fine mesh of *l*=0.5mm, a series of coarse mesh are employed, by setting the number of elements *N* to be 36, 18, 9, 6 and 3, respectively, in the middle section. Figure 3.15 shows three typical sets of meshes for a structure size *D* of 192mm, with *N*=9, 18 and 288, corresponding to the element sizes *l*=16mm, 1mm, 0.5mm, respectively.

Figure 3.16(a) shows that the influence of *N* on the stress distribution for concrete tension. With a structure size *D* of 24mm, N=3 was enough for obtaining accurate stress distribution. However, a different *N* was required for different structure size, *N*=6 and *N*=18 were required for *D*=192mm and *D*=768mm, respectively, as can be observed in Figure 3.16(b) and Figure 3.16(c). Even though different *Ns* were required for different structure sizes, there was something in common: at least three elements are required in the fracture process zone to represent the nonlinear stress distribution. Thus, for the size effect analysis with typical range of structure size, two opposite factors should be considered on choosing the mesh size or the number of element layers in the middle. One one hand, as the fracture process zone increases with the structure size, a larger mesh size can be used for large size structure. On the other hand, at the same time the relative fracture process zone decreases, and a larger number of elements is required.

To ensure the accuracy of stress distribution for all different structure size, it is suggested at least *N*=18 is required in the whole cross section, to ensure at least three elements in the fracture process zone for not too large structure. For *N*=18 with *D*=768mm, the element size is 32mm, approximately one-tenth of the characteristic length 293mm. Thus results of this study agreed with the conclusions obtained by Moes and Belytschko[53],Carpinteri et al.[74], Camanho et al. [75] and Turon et al. [60]; while the suggestion by Tomar et al. [61] appeared to be conservative.

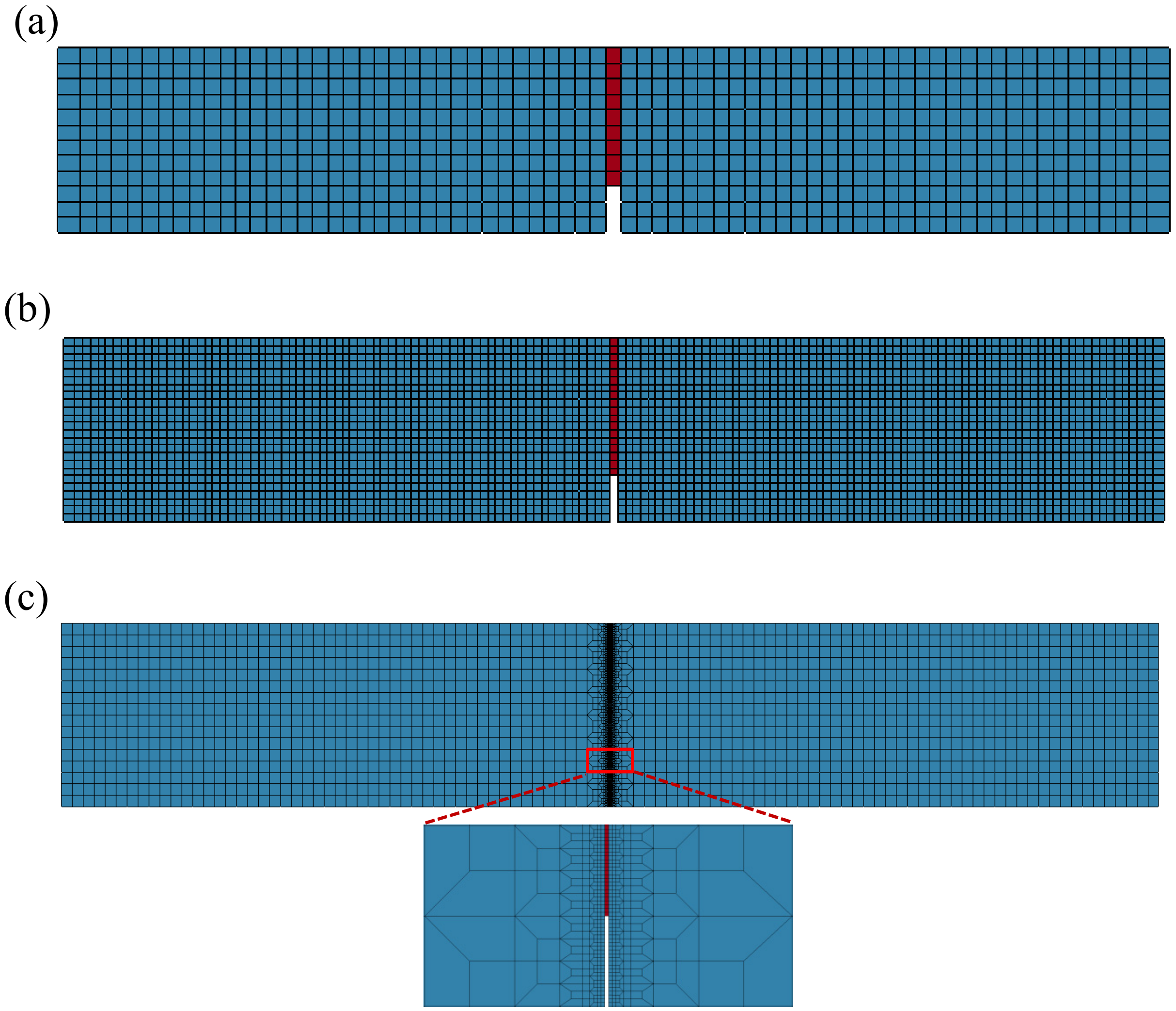

Figure 3.15 Typical finite element mesh for concrete with different No. of element layers N in the middle cross section (D=192mm): (a) N=9, (b) N=18, (c)N=288

(a)

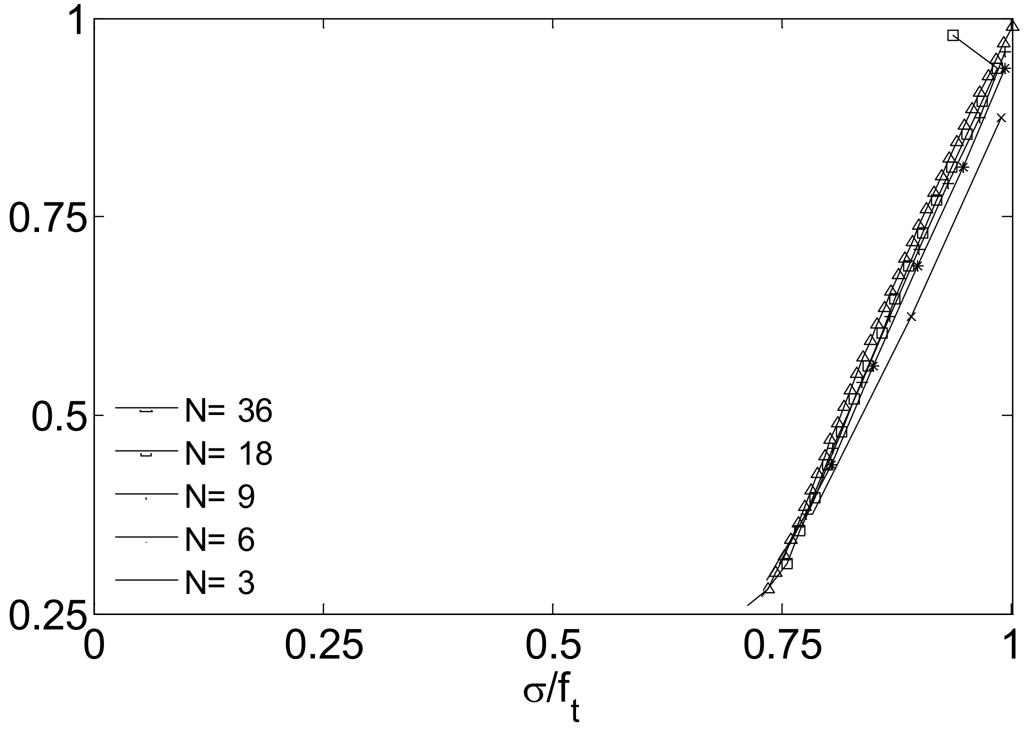
x/D
1
0.75
0.5
0.25
0
0.25
0.5
0.75
1
σ/f_t
N= 36
N= 18
N= 9
N= 6
N= 3

(b)

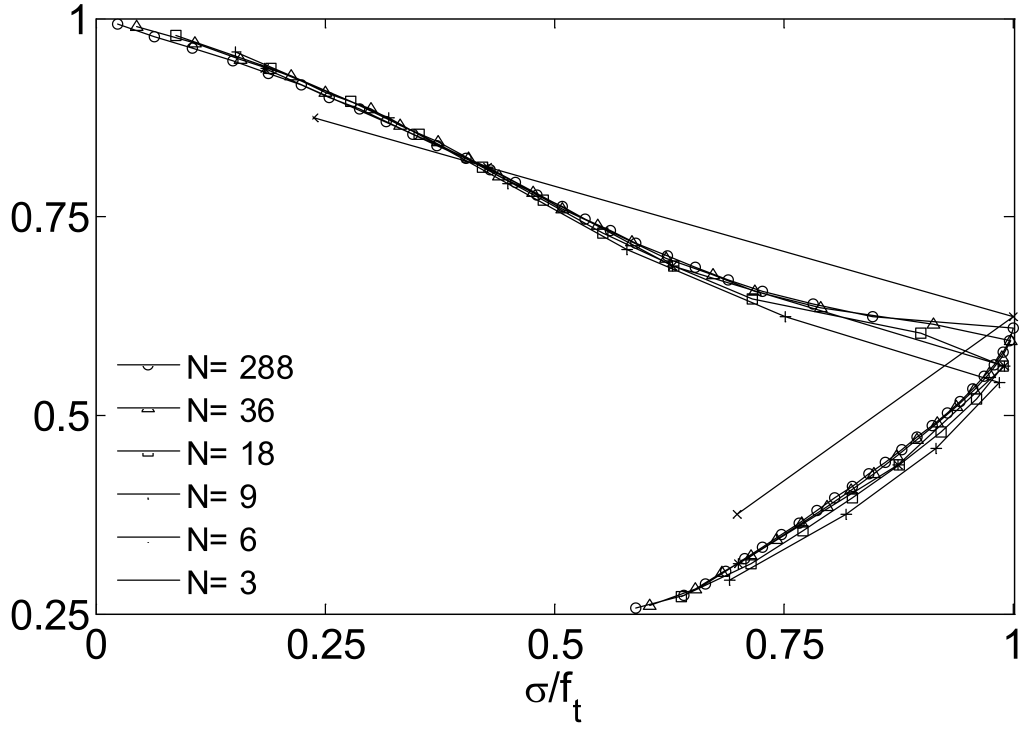
x/D
1
0.75
0.5
0.25
0
0.25
0.5
0.75
1
σ/f_t
N= 288
N= 36
N= 18
N= 9
N= 6
N= 3

(c)

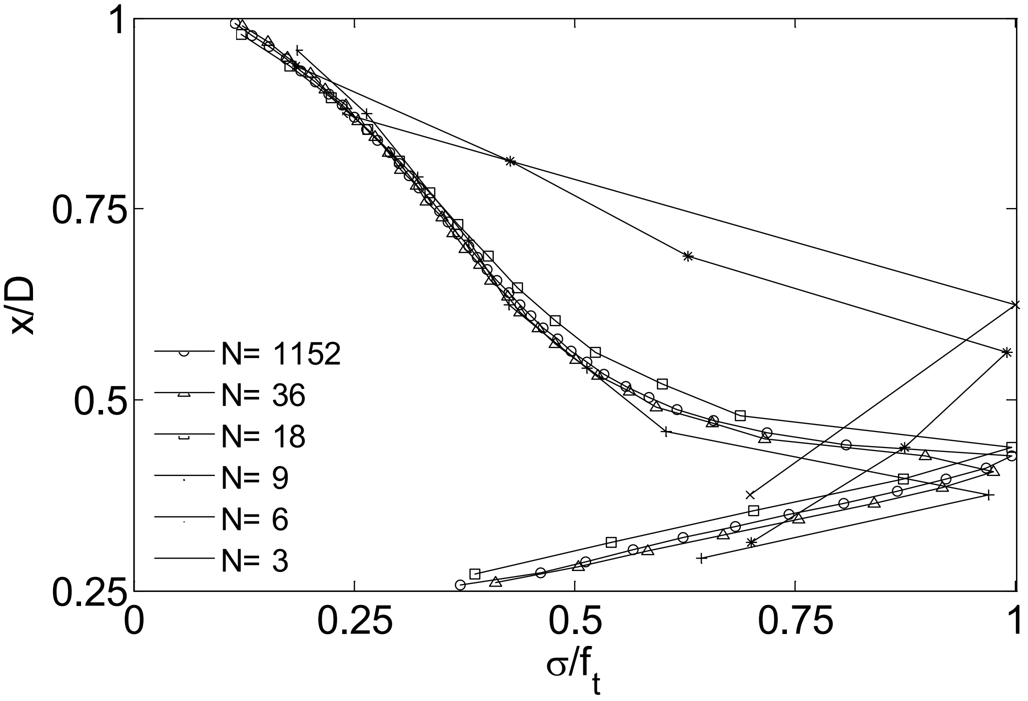

Figure 3.16 Typical stress distribution for concrete under tension with different No. of element layers N in the middle cross section:(a) D=24mm, (b) D=192mm, (c) D=768mm

Figure 3.17 summarizes the size effect results of concrete under tension and bending, using both fine mesh and coarse meshes. The fine mesh refers to fixed mesh size *l*=0.5mm in the middle for all structure size, while the coarse mesh refers to fixed 18 layers of element regardless of the structure size. A good comparison was obtained, showing that the relative error was smaller than 3% in all cases, even though mesh size differed by up to 128 times.

(a)

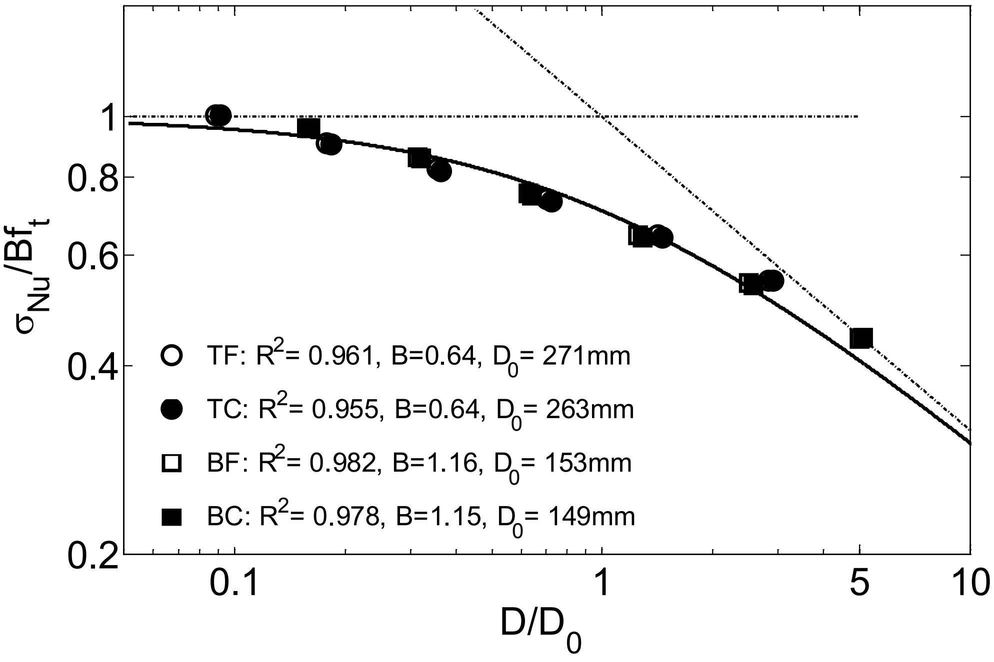

(b)

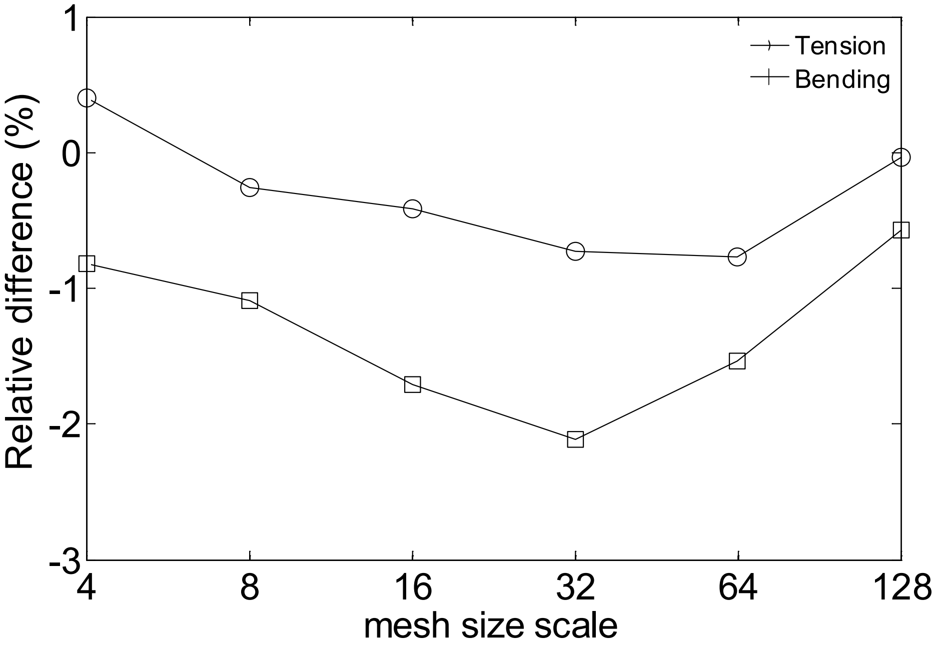

Figure 3.17 A comparison of size effect results for concrete with different mesh size:(a)Size effect results under tension and bending with fine mesh and coarse mesh, (TF: Tension with fine mesh, TC: Tension with coarse mesh, BF: Bending with fine mesh, BC: bending with coarse mesh) (b) Relative difference of nominal stress with different mesh size

3.4.2 Influence of shape of softening curve

The shape of softening curve is very important, as it governs the stress in the fracture process zone. Dugdale[76] originally proposed a model with a constant stress ahead of the crack tip, in other words, he proposed a rectangular softening curve. Hillerborg[50] extended it to both a trapezoid and a linear softening curves. Petersson[77] showed a bilinear softening could reasonably approximate the behavior of concrete. More complicated softening functions, such as quasi-exponentially decaying functions have also been proposed[78].

It has been recently shown that the initial portion, instead of the whole of the softening curve, played a paramount role in determining the peak strength for not too large structure[51, 79]. The reason is that a crack that is not fully opened at peak load, the fracture process zone would sweep only the initial part of the softening curve, as shown in Figure 3.18.

The continuum damage model implemented in the material model MAT159, accommodates different initial slopes, from relatively flat to steep. Eq. (3.9) can be approximately expressed as :

$$d \to \begin{cases} 1-\exp^{-C\left(\tau_b-\tau_{0b}\right)} & A \to 0 \\ 0 & A \to \inf \end{cases} \tag{3.22}$$

Thus this softening curve is able to model exponential softening with small A and approximately rectangular softening with large A, as well as moderately descending initial slope between the two limits.

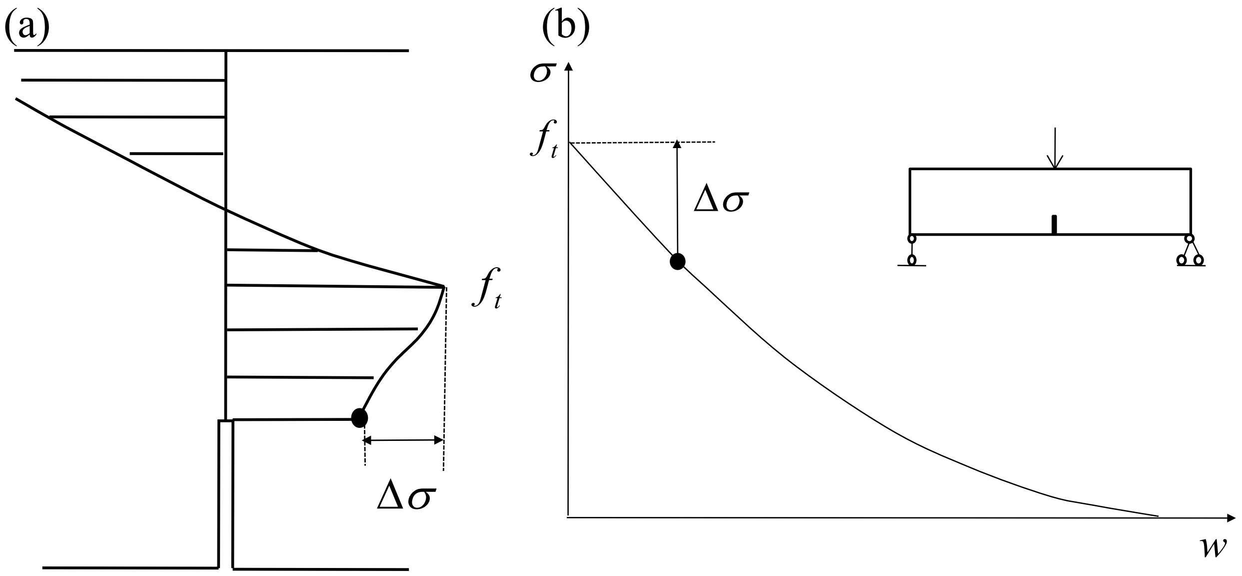

Figure 3.18 Maximum stress drop in the fracture process zone at peak load under bending: (a) Stress profile at peak load, (b) A typical stress separation curve and the location of stress at the initial notch tip on the softening curve [51]

Figure 3.19(a) shows the softening shape with A, of 0.001, 0.1, 1 and 10 for concrete material, while the fracture energy is fixed at G_f=85N/m. For the same softening curve, different range of the curve will be swept for different structure size. Figure 3.19(b) shows that the crack opening displacement of the initial notch tip for different structure size, with A=0.1. Generally, a larger structure will lead to a larger crack opening displacement, and that in turn leads to larger stress drop. Figure 3.19(c) summarizes stresses at the initial notch tip for both concrete and rock, under tension and bending test. All the data follow the trend of stress displacement under plane strain condition, but some discrepancy is also observed for rock. It is postulated that the relative larger Poisson's ratio for rock might be the cause, as the stress displacement curve obtained depends on plane stress, plane strain, triaxiality and other variables [51, 80].

(a)

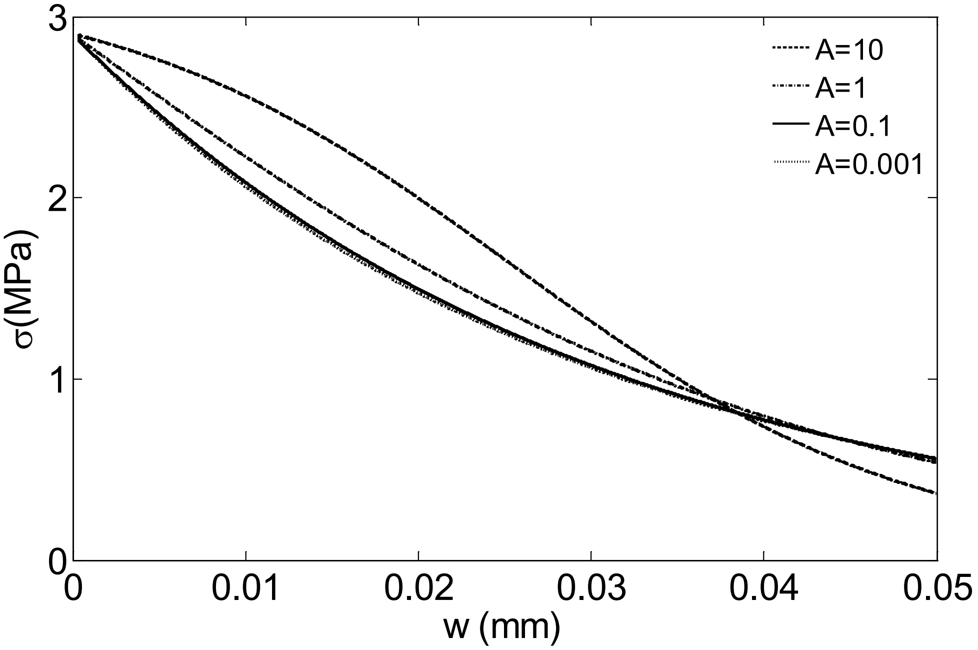
A=10
A=1
A=0.1
A=0.001
σ(MPa)
w (mm)
0
1
2
3
0.01
0.02
0.03
0.04
0.05

(b)

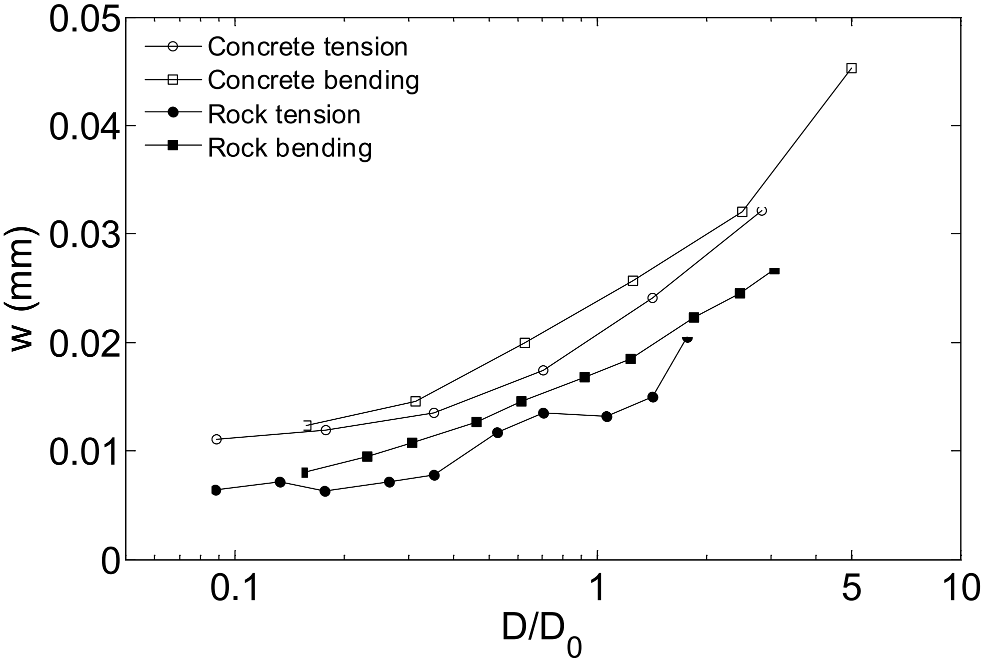
Concrete tension
Concrete bending
Rock tension
Rock bending
w (mm)
D/D_0
0
0.01
0.02
0.03
0.04
0.05
0.1
1
5
10

(c)

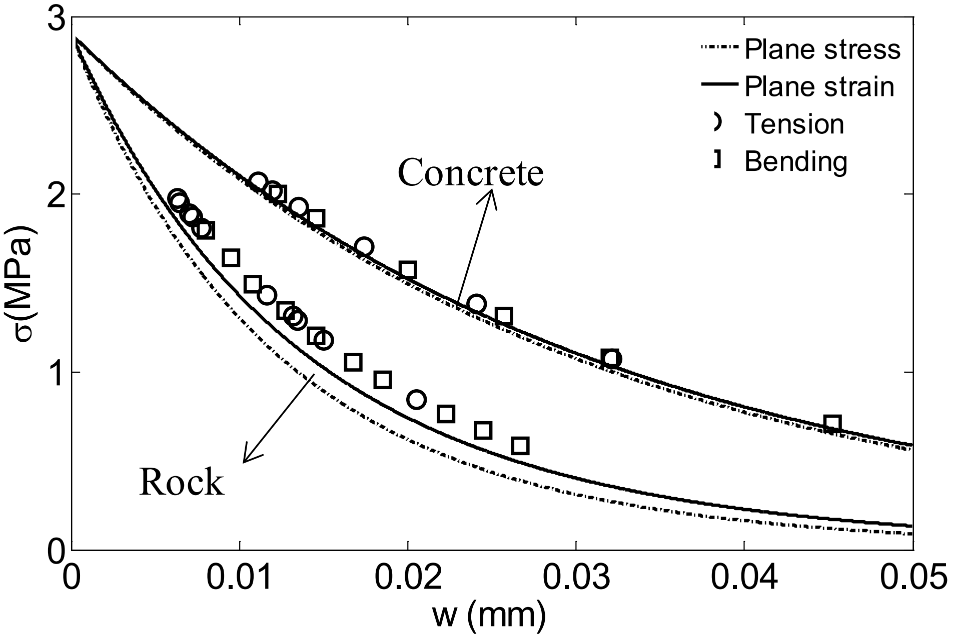

Figure 3.19 Influence of softening shape on the stress at the initial notch tip: (a) Influence of *A* on softening curves for concrete under plane stress conditions, (b) Influence of structure size on the crack mouth opening displacement, (c) Locations of stress at the initial notch tip at peak load

3.5 SIZE EFFECT IN ROCK CUTTING

Experiments have shown that the in rock cutting, rock fails mainly by crushing when the cutting depth is shallow, and by crack growth when depth of cut is deep. The energy dissipated mechanism is therefore different, energy is dissipated by volume in shallow cuts and by surface in deep cuts. Clearly there exists also a transition from a failure is governed by strength criterion to that governed by LEFM criterion in rock cutting. This line of thoughts led to the present proposal of treating the cutting depth as a measure of size corresponding to Bažant’s simple size effect law.

A set of geometrical similar rock samples with different sizes was generated. The dimensions and some typical mesh are shown in Figure 3.20. Tetrahedron elements were used, and the mesh size was fixed to be approximately *l*=0.15mm. The rake angle of the currer was $\theta = 15^0$, and the width of rock sample was *b*=0.1mm. Plane strain boundary was applied, and the normal translation in the bottom, left and right boundary were fixed. The cutter advances forward with a velocity of *v*=0.2mm/ms. The dynamic compressive strength and dynamic tensile strength consider the rate effect was approximately $\sigma_c = 47MPa, f_t = 3MPa$, respectively. The depths of cut chosen were *D* = 0.5, 0.6, 0.7, 0.8, 1.0, 1.2, 1.4, 1.6, 1.8, 2.0, 2.5, 3.0, and 4.0 mm. No depth below 0.5mm was chosen because that would be less than three layers of element in contact with the cutter as mesh size was set as *l*=0.15mm.

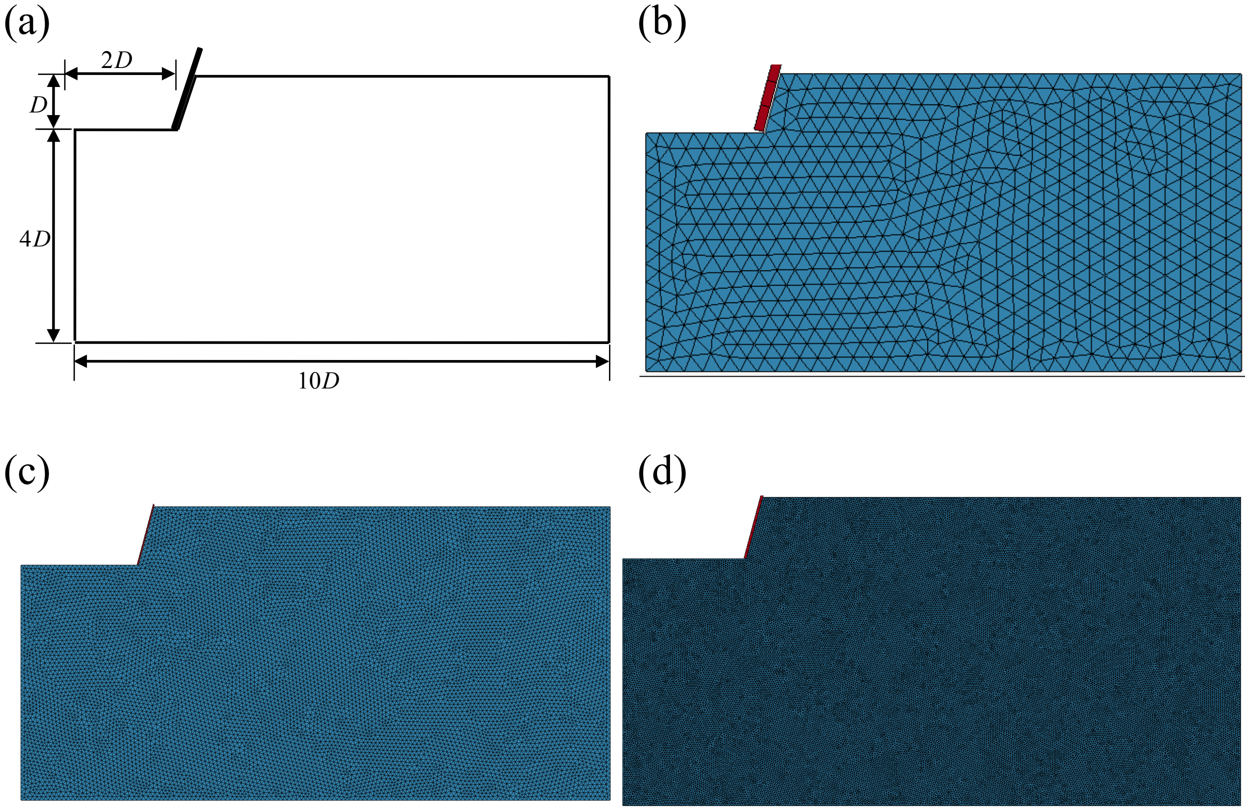

Figure 3.20 Geometry and mesh in rock cutting: (a) geometry, (b) D=0.5mm, (c) D=2mm, (d) D=4mm

Figure 3.21 shows the damage configuration from different cutting depths, with *D* = 0.5, 2.0, and 4.0 mm, respectively. Two snap shots were taken for each depth, one corresponding to peak cutting force, and the other after the peak cutting force.

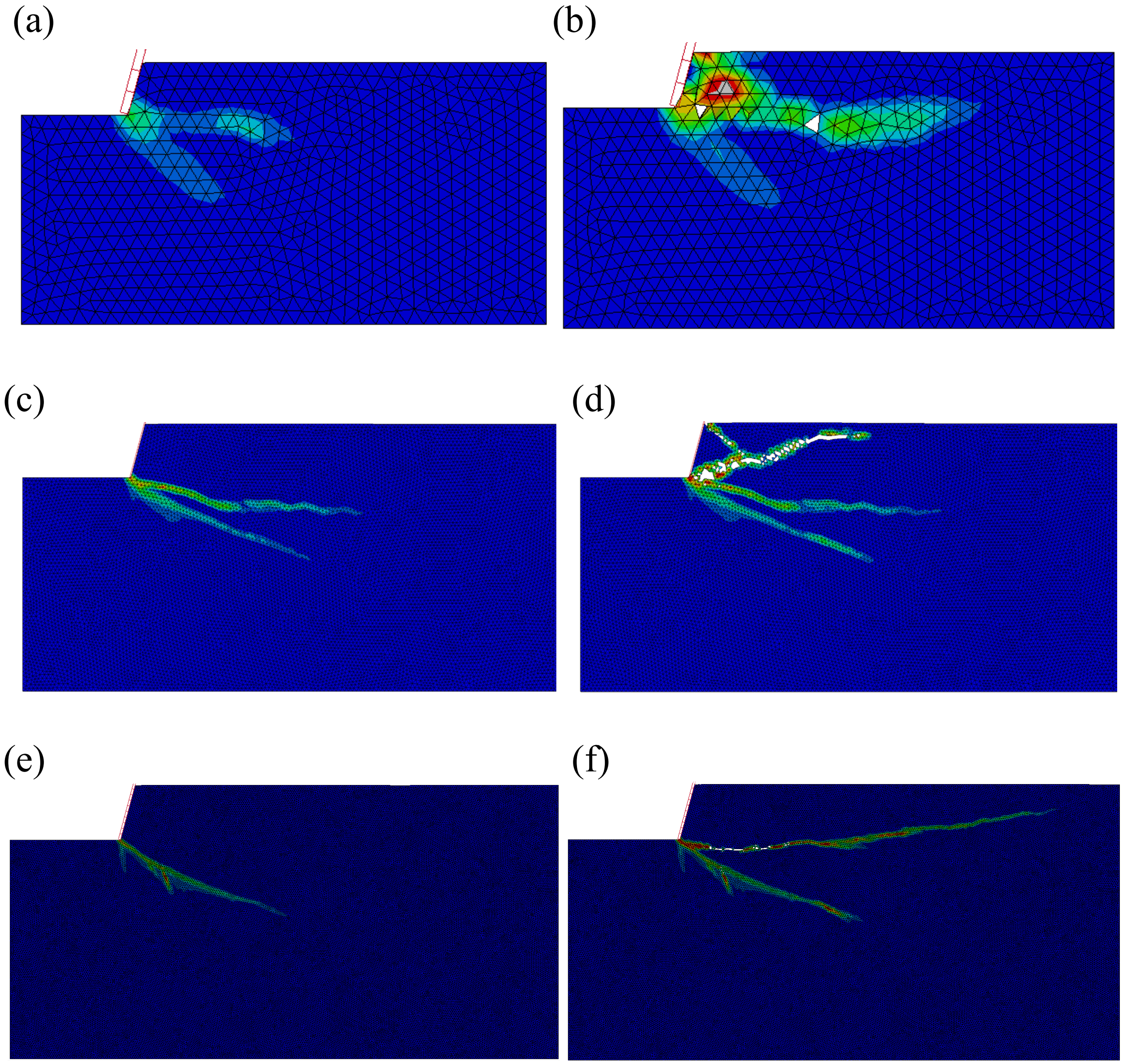

Figure 3.21 Damage configuration of rock cutting (a) D=0.5mm, corresponding to peak force (b) D=0.5mm, after peak force (c) D=2mm, corresponding to peak force (d) D=2mm, corresponding to peak force(e) D=4mm, corresponding to peak force (f) D=4mm, after peak force

It was found the failure pattern as observed in the distribution of damaged areas was much more complicated than those posed by a tension test, or by a three point bending test confined to mode I failure.

Stress state of some typical elements along the crack was analyzed. It was found that for a typical element with some damages, i.e., the damage index lies between 0 for no damage and 1 for complete damage, the damage would accumulate under both compression and tension stress states. The results suggested that rock cutting failure is governed by a mixed mode of failure. Despite of the complexity of the failure mode, the damage configurations were similar for different cutting depths when the peak cutting force was reached. But the pattern started to diverge afterwards.

To interpret the cutting test results with Bažant's simple size effect law, the nominal stress σ_N and ultimate nominal stress σ_{Nu} in the cutting tests are defined as:

$$\sigma_N = \frac{F_c}{bD}, \sigma_{Nu} = \frac{F_p}{bD} \tag{3.23}$$

where F_c is the cutting force, and F_p is the peak cutting force.

Compared with tests under tension and three point bending, the stress field in rock cutting is dominated by compression in front of the cuter. Thus the compressive strength, instead of tensile strength, was used to normalize the nominal stress in Bažant's simple size effect law, and it is introduced in rock cutting as followed:

$$\sigma_{Nu} = \frac{B\sigma_c}{\sqrt{1 + D / D_0}} \tag{3.24}$$

The result of the fit is shown in Figure 3.22. A higher fluctuation of the data point around the simple size law is not unexpected since the stress field is more complicated. Nontheless, with the R^2 of the fit was still rather high at 0.844, and the parameters obtained were B=1.77, D_0=2.04mm.

The stress and relative displacement curves for three typical cutting depths are also shown in Figure 3.23. The relative displacement is defined as the ratio of horizontal displacement over cutting depth. A similar trend as the size effect from the tension and the three point bending tests was found: (1) the initial slope before peak strength was approximately the same; (2) the peak nominal stress for smaller cutting depth was larger; (3) the shape after peak strength was flatter for shallow cuts, suggesting its behavior to be more ductile.

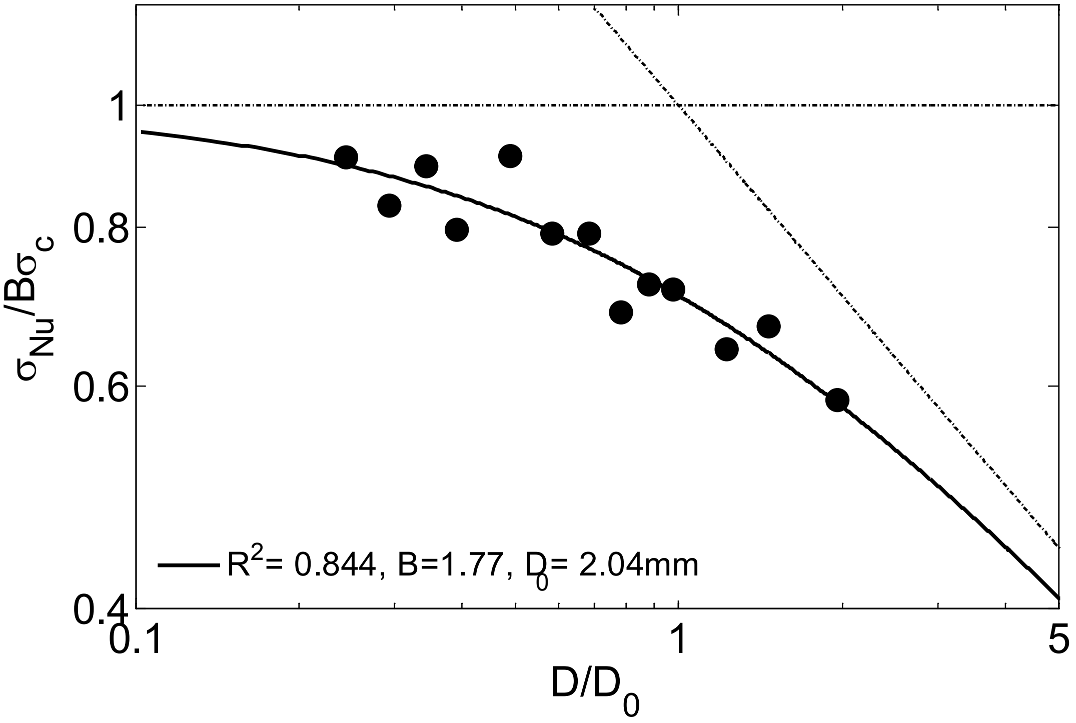

Figure 3.22 An interpretation of rock cutting with Bažant's simple size effect law

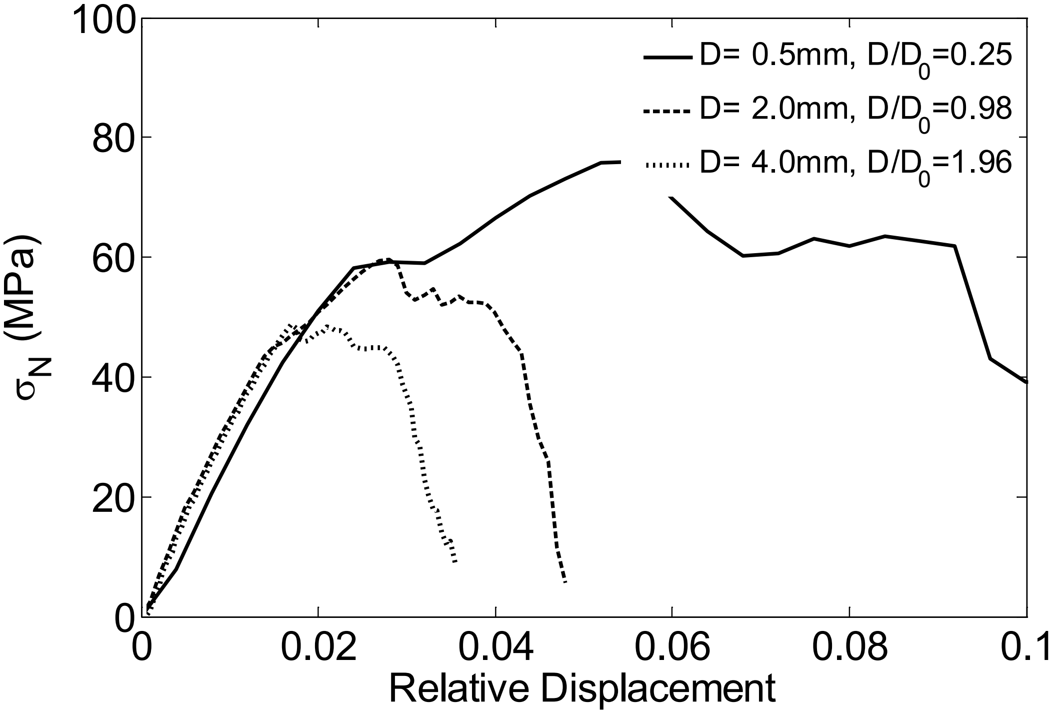

Figure 3.23 Stress and relative displacement with different size in rock cutting

3.6 CONCLUSIONS

This study modeled rock cutting based on damage mechanics, and introduced Bažant's simple size effect law in interpreting the result. Previously, Bažant's simple size effect law was found to hold under either mode I or mode II conditions, this study showed the law is also applicable in rock cutting with mixed mode failure, as posed in a rock cutting problem.

For modeling the failure of quasibrittle materials, a successful model should capture the crack propagation and fracture process zone during the fracture. Cohesive model have been widely used in modeling crack propagation in mode I and mode II condition, but has limitation in modeling rock cutting with mixed mode failure, and with unknown crack growth path. The continuum damage model was thus adopted. The damage model compared well with the cohesive model under model I failure after appropriate scaling, and that provided a credence of the continuum damage model in a general setting.

The study found relatively coarse mesh would also render good resolution results for the three point bending test of concrete. Similar to the role of traction separation curve of a cohesive model, the softening curve in the damage model governs the stress distribution in the fracture process zone.

4.0 ON THE CRITICAL FAILURE MODE TRANSITION DEPTH FOR ROCK CUTTING

4.1 INTRODUCTION

Cutting, much like indentation, induces in rocks two different modes of failure: the ductile mode of failure and the brittle mode of failure. The ductile mode of failure prevails when the depth of cut is shallow, and rocks fail either via the development of damage zones or through some plastic flow. In contrast, when the depth of cut is deep, the mode of failure becomes brittle and the rock fails through fracture. For processes such as drilling or tunneling, it is often desirable to control the extent of a rock being removed and that fail a rock in a particular mode becomes essential. As the cutting depth progresses from shallow to deep, there is a critical depth that the rock failure changes from the ductile to the brittle mode. This is one of the important questions that Detournay and his team at the University of Minnesota studied, and in fact they have been instrumental to the current understanding on this subject [4-6, 19].

Through extensive tests, Richard et al. [5, 6] have shown that within the ductile failure mode, the average specific mechanical energy input in a scratch test is directly proportional to the uniaxial compressive strength of rocks, σ_c, and proposed that the scratch test could serve as a rapid method for determining the uniaxial compressive strength of sedimentary rocks. The specific energy [31], ε, in a scratch test maintained at a fixed depth of cut of a wide cutter can be expressed as

$$\varepsilon = \frac{F}{wd} \tag{4.1}$$

Where F is the average cutting force, w is the width of a cutter, and d is the depth of cut.

When a rock is failed in a ductile mode, the average cutting force is proportional to the depth of cut since the specific energy is proportional to σ_c, namely [6]

$$F \propto \sigma_c wd \tag{4.2}$$

On the other hand, during a brittle failure the cutting force would be proportional to the square root of the depth of cut according to the Linear Elastic Fracture Mechanics (LEFM). In other words, the cutting force for deep brittle mode can be written as [6]

$$F \propto K_{IC} w\sqrt{d} \tag{4.3}$$

By equating the two equations, a critical failure mode transition depth, d_c, thus can be determined as [6]

$$d_c \propto \left(\frac{K_{IC}}{\sigma_c}\right)^2 \tag{4.4}$$

Test data from Nicodeme [4] were employed by Richard to obtain the transition depth. Nicodeme's data for Vosges sandstone, Berea sandstone and Rhune sandstone were reproduced in Figure 4.1. In these plots, both the average forces and the average peak forces were presented. Because peak forces are more closely related to the fracture initiation process, they are more relevant in the transition depth discussion. There is an uncertainty associated with this approach because it is not clear data from which depth should be fitted by Eq. (4.3). This uncertainty could be removed as elaborated in the discussion that follows.

Huang and Detournay [19], took up a different approach using dimensional analysis and obtained a similar relationship. They defined an *intrinsic length scale* as follows,

$$l_i = \frac{1}{\pi}\left(\frac{K_{IC}}{\sigma_c}\right)^2 \tag{4.5}$$

With the aid of discrete element simulation they further proposed that the critical transition depth is related to this intrinsic length scale. In essence, they affirmed the earlier results of Richard et al.

(a)

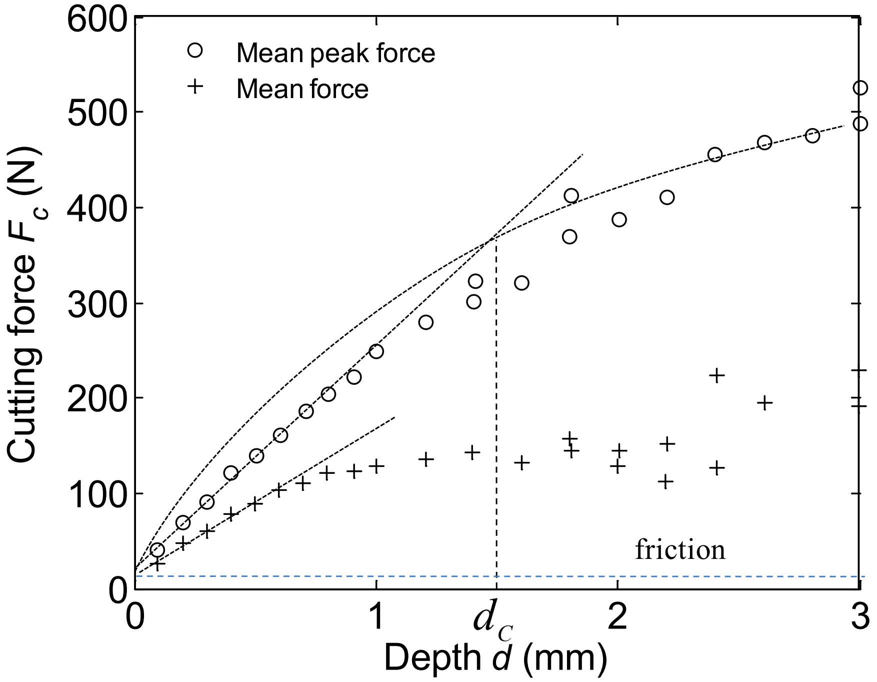

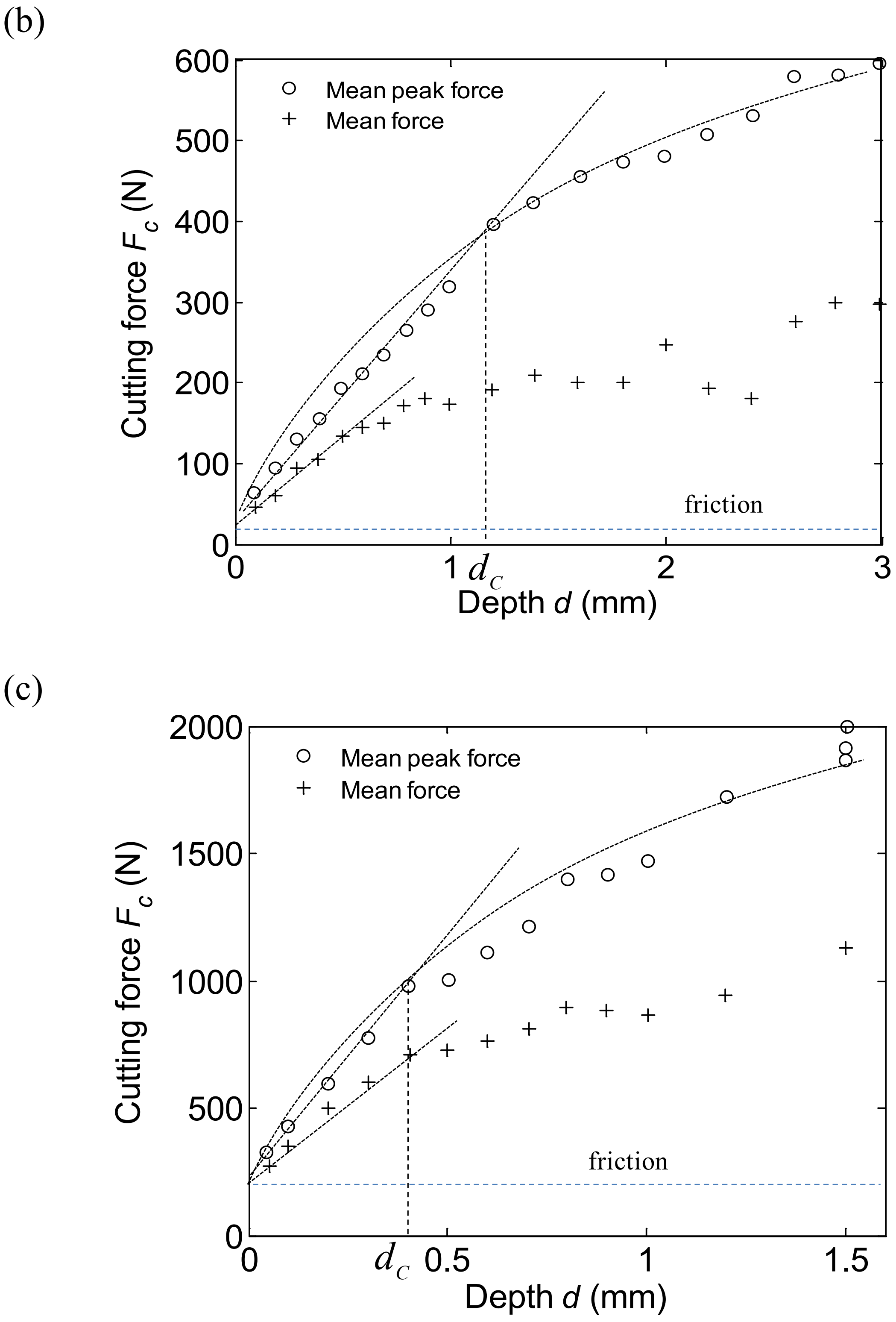

Figure 4.1 Evolution of cutting force with cutting depth: (a) Vosges sandstone, (b) Berea sandstone, (c) Rhune sandstone, [4, 5]

4.2 A DIFFERENT VIEW FROM THE SIZE EFFECT ANGLE

The problem of ductile-brittle transition in a fracture process is an important one and viewed from a larger context may provide some insights on rock mechanics applications. In this respect, Puttick [33] has developed a theory of transition based on the scaling law of crack propagation deduced from fracture mechanics. In his theory the size effect appears because as the size of a test specimen is increased under geometrical similarity, the energy supply in the form of volume strain energy grows as a cubic function of some linear dimension, while the demand of the growing crack increases as the square of the same dimension. He further argued that for a failure involved an inhomogeneous tensile stress field, the rate of strain energy release depends also on a characteristic length defined by the strain energy field. His theory concluded that the apparent fracture stress is a function of both this characteristic length and the geometry of the test sample. This characteristic length, l_{ch}, is related to the crack fracture process zone, which in the concrete fracture literature is often expressed as [80]

$$l_{ch} = \frac{G_{ft} E}{\sigma_t^2} \tag{4.6}$$

Where G_{ft} is fracture energy, E is Young's Modulus, and σ_t is the tensile strength.

To follow up on Puttick theory about the connection between the size effect and the ductile-brittle transition, we reexamined Nicodeme's data [4]. For the rock cutting problem, based on the findings of the Minnesota group a recast of the problem can be proposed as follows: the rock cutting be viewed as a geometrically similar problem and that the depth of cut the size measure. With this in mind, bilogarithmic plots of Nicodeme's data using average peak forces are presented in Figure 4.2. Here we define the nominal stress as the average peak cutting force, F_C, divided by the cross section of cutter-rock contact as follows,

$$\sigma_N = \frac{F_C}{wd} \tag{4.7}$$

The plots clearly demonstrate that rock cutting, when the depths of cuts lie within the range of practical interests, follows the size effect law of ductile-brittle transition of quasibrittle material as Bažant [36] has proposed for concrete. Bažant simple size effect equation fit to these data were carried out using the following form,

$$\sigma_N(d/d_0) = \frac{B\sigma_c}{\sqrt{1+d/d_0}} \tag{4.8}$$

Where B is a scaling factor, d_0 represents the intersection of asymptotes and is a measure of how large the transition zone is.

(a)

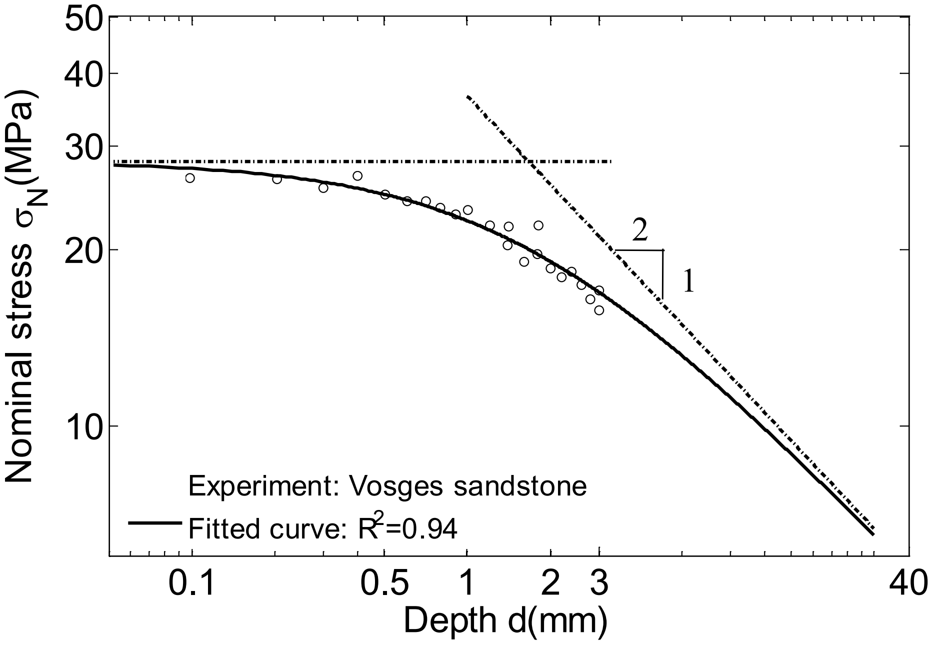

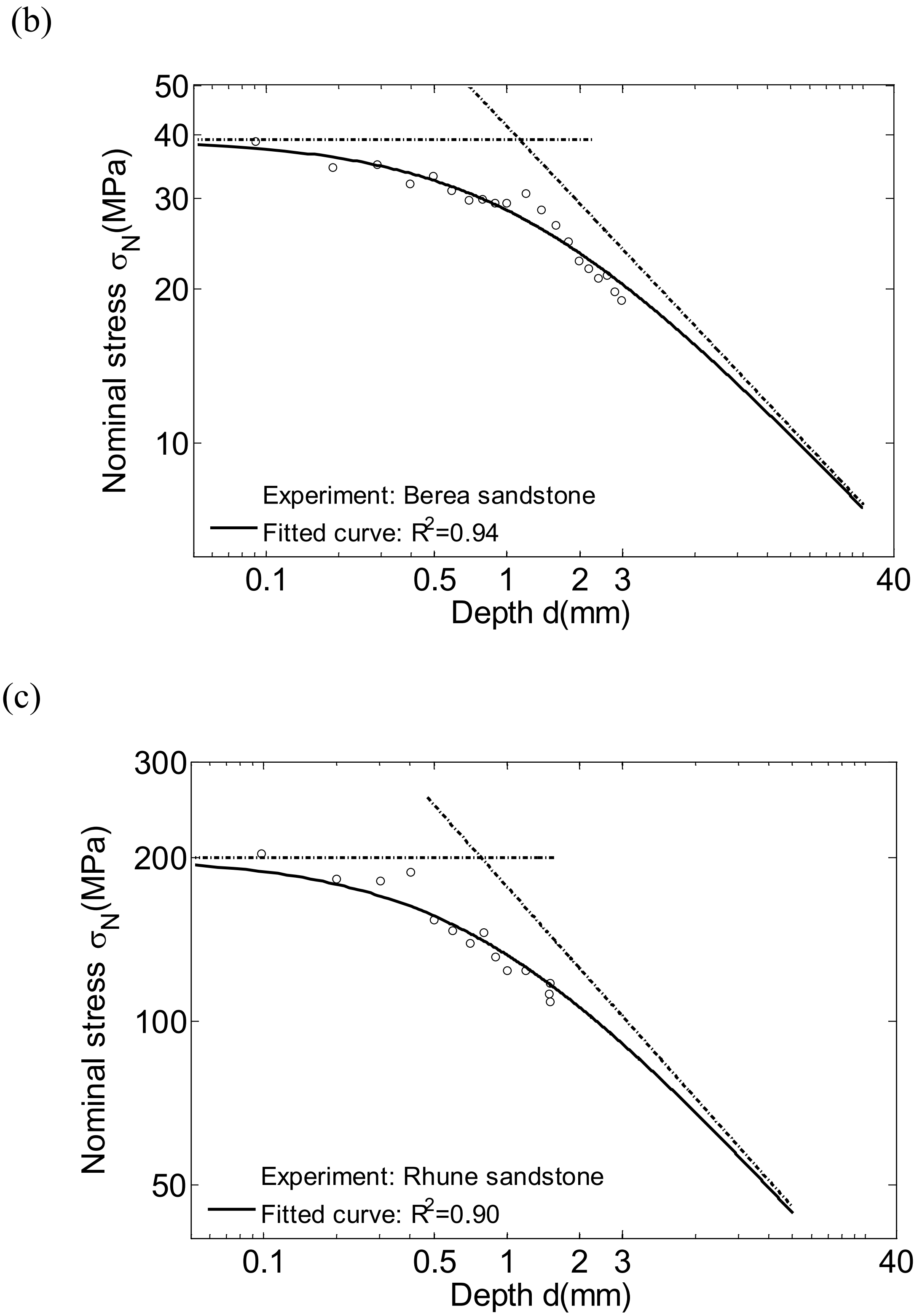

Figure 4.2 Evolution of nominal stress with cutting depth : (a) Vosges sandstone, (b) Berea sandstone, (c) Rhune sandstone, [4, 5,32]

Nicodeme's data gave non-zero intercepts on the forces versus depth plots, which implied presence of friction caused by cutter wear. For the Vosges sandstone and Berea sandstone data, the frictions were small, with magnitudes around 15 and 28.5 N, respectively. Whereas for the Rhune sandstone, the friction was as high as 230 N, but in this case the rock strength was also high. These frictions were subtracted with the assumption that the cutter wear remained unchanged during the cutting, and this step might introduce significant error in the interpretation of Rhune sandstone results.

Bažant size effect equation fit Nicodeme's data well: for the Vosges sandstone test, $B\sigma_c$ =28.3 MPa, d_0= 1.67 mm, R^2 of fit was 0.94; for Berea sandstone, $B\sigma_c$ =39.1 MPa, d_0=1.13 mm, R^2 of fit was also 0.94; for Rhune sandstone, $B\sigma_c$ =200 MPa, d_0=0.78 mm, R^2 of fit was 0.90. The larger scatter in the Rhune sandstone data fit might reflect that the friction was not properly addressed. Using Bažant size effect law removes the uncertainty about the data selection because cutting data from all depths were use. In the discussion that follows, the critical transition depth, d_c, was estimated using d_0.

The application of Bažant size effect equation may be interpreted as follows: at shallow cut the plasticity dominates, then as the depth of cut increases it gradually shifts toward fracture mode with a -1:2 slope on the bilogarithmic plot dictates by the LEFM. The transition clearly is a gradual process, and that LEFM is reached only asymptotically.

With the size effect law fitting the data well, it follows that the work on qusaibrittle material from concrete fracture research could also have important bearing. In this respect, we looked into Hillerborg's characteristic length which has been widely used in concrete fracture research.

4.3 CHARACTERISTIC LENGTH AND INTRINSIC LENGTH SCALE

According to Irwin [81], the energy release rate and stress intensity factor are equivalent in the critical condition of mode I crack, namely

$$G_{ft} = \kappa \frac{K_{IC}^2}{E} \tag{4.9}$$

where $\kappa = 1$ for plane stress condition, and $\kappa = 1 - \nu^2$ for plane strain condition, and ν is the Poisson's ratio.

Applying the above equation, the characteristic length can alternatively be defined below as a function of the mode I fracture toughness and tensile strength:

$$l_{ch} = \kappa \frac{K_{IC}^2}{\sigma_t^2} \tag{4.10}$$

Puttick [33] has mentioned that the yielding strength other than the tensile strength might be used in defining the characteristic length, Huang and Detournay [19] were the first to use the uniaxial compressive strength for this purpose. We can view Huang and Detournay's intrinsic length scale in terms of Hillerborg's characteristic length as follows,

$$l_i = \frac{1}{\pi\kappa} \frac{l_{ch}}{\left(\sigma_c / \sigma_t\right)^2} \tag{4.11}$$

The greater the Hillerborg's characteristic length, the greater the intrinsic length scale is, and the deeper it goes before failure shifts from ductile to brittle. In other words, the greater the Hillerborg's characteristic length, the more ductile a material becomes; and it is a measure of ductileness. On the other hand, the ratio of uniaxial compressive strength over tensile strength is clearly related to the brittleness of rock [82]:

$$B_1 = \sigma_c / \sigma_t \tag{4.12}$$

Thus Huang and Detournay's measure can be viewed as a contrast of ductileness to brittleness, and its physical significance then becomes clear: When the ductilness to brittleness ratio is large, the critical depth of failure mode transition increases.

From the present discussion it follows that Eq. (4.4) can be rewritten as

$$d_c \propto \frac{l_{ch}}{B_1^2} \tag{4.13}$$

For engineering applications, it would be beneficial to know d_c of a given rock, and an establishment of the above equation would be useful. Can this relationship be determined other than using experiments? A reflection on the Bažant's size effect law, particularly on the substantial plastic deformation during transition and complex mechanics of cutting, leads to the conclusion that the critical depth of failure mode transition is unlikely to be theoretically derived. In view of this, a computational procedure is presented below.

4.4 A COMPUTATIONAL CALIBRATION PROCEDURE

A numerical method that would facilitate the specification of right hand side of Eq. (4.13) may serve as a basis for determining the proportionality constant posed by Eq. (4.13). The explicit finite element program LS-DYNA [57] fit this objective and was employed in the numerical analysis. Specifically, a constitutive model-- a continuous surface cap model, i.e., model 159 in LS-DYNA, enabled such an undertaking. The main features of the model [40] include a plastic yield surface with a smooth cap, the damage-based softening with erosion and modulus reduction and rate effects for strength increase in high strain rate application. A detailed description of the procedure in rock cutting application, including the determination of rock parameters, can be found in [83].

For the present application, the most important feature of this continuous surface cap model is that it facilitates the input of fracture energy G_f, σ_c and σ_t that, in turn, makes the specification of characteristic length feasible. σ_c and σ_t are defined through the specification of the yield surface, while G_f is directly input.

In the continuum surface cap model, strain softening starts when the stress reaches the yield surface. As the strain softening continues, fracture eventually takes place when the cumulative energy release, or the stress times the displacement, equals the material fracture energy. That is [40],

$$G_f = \int_{x_p}^{x_f} \sigma(x)\,dx \tag{4.14}$$

Where $\sigma(x)$ is the stress during the strain softening, x_p and x_f are the displacements at the yielding and fracture, respectively.

Three fracture energies are defined in the continuum surface cap model: The fracture energy due to tension, or mode I fracture , G_{ft}, the fracture energy due to shear, or mode II, G_{fs}, and the fracture energy due to compression, G_{fc}. Which fracture energy is used depending on the stress state when the yield surface is reached: the uniaxial tension failure triggers G_{ft}, pure shear failure triggers G_{fs} , and the uniaxial compression failure triggers G_{fc}, that is, $I_1/\sqrt{3J_2}$ equals to -1, 0, and 1 ,respectively, as depicted in Figure 4.3, where I_1 denotes the first invariant of the stress tensor, and J_2 the second invariant deviatoric stress tensor. For other stress states, interpolation is used: $I_1/\sqrt{3J_2} \leq -1$ uses G_{ft} , $-1 < I_1/\sqrt{3J_2} < 0$ interpolates between G_{ft} and G_{fs},

$0 < I_1/\sqrt{3J_2} < 1$ interpolates between G_{fs} and G_{fc}, and $I_1/\sqrt{3J_2} \geq 1$ uses G_{fc} . Tensile stress is defined negative, and when $I_1 \leq 0$, pure mode I and pure mode II fracture are governed by the same fracture energy [84] , thus G_{fs} was set equal to G_{ft} in this study. As for fracture under compression, there existed very few data to guide the selection of G_{fc}. From Li's data [85], Shen and Stephansson [86] concluded that fracture energy in compression could be greater than 100 times of G_{ft}. We carried out limited sensitivity with G_{fc} varied between 100 and 250 times of G_{ft}, and found that fragmentation pattern next to the cutter might change slightly, but the cutting forces were not much affected. Accordingly G_{fc} was set equal to 100 G_{ft} in this study.

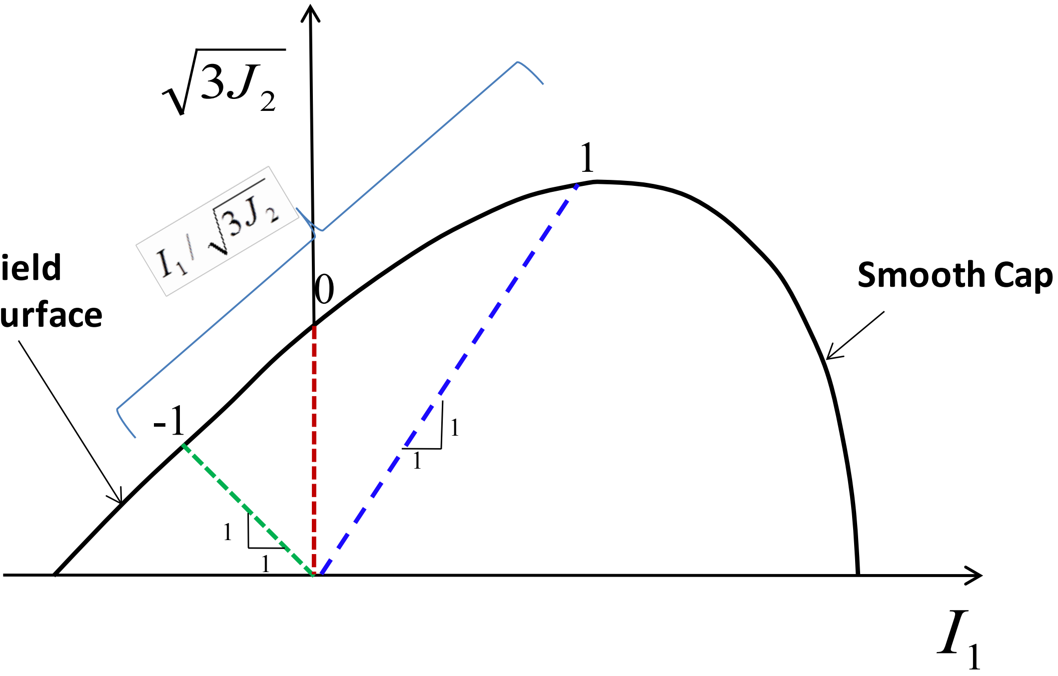

Figure 4.3 Stress states upon which the fracture energies are defined

In the analysis carried out, each rock sample was assigned a different characteristic length. This was achieved by varying the fracture energy, while all other essential properties such as σ_c, σ_t, the Young's modulus, and the Poisson's ratio remained fixed. Table 4.1 summarizes some typical values of fracture energy for rocks [63]. First, a baseline case was developed based on the properties of Vosges sandstone, in that the uniaxial compressive strength was set to 36MPa, the tensile strength to 3MPa, the Young's modulus to 8.3GPa, the Poisson's ratio to 0.3, and the fracture energy, G_{ft}, to 35 Jm^{-2}. Following that, the fracture energies were the only change made to provide a host of characteristic lengths Using Table 4.1 as a guide, the fracture energies of the following values were further employed in computation: $G_{ft} = 8.8Jm^{-2}$, $17.5Jm^{-2}$, $26.3Jm^{-2}$, 43.8 Jm^{-2}, $52.5Jm^{-2}$. Thus, except for the baseline case, the rock samples used were not realistic in the sense that the parameters were artificially set. Thus it was essential that real test data were also used in evaluating the analysis.

Table 4.1 Some typical values of fracture surface energy of rocks [63]

Rocks	Fracture surface energy γ_c (Jm^{-2})
Fontainebleau sandstone	7-27
Berea sandstone	10
Carrara marble	35
Solnhofen limestone	12
Red Oland limestone	19
Holston limestone	12

To obtain the critical transition depth corresponding to each sample, a series of scratch tests were conducted. The dimension of rock sample used was 24mm in length, 5mm in depth and 1mm in thickness. The average mesh size was about 0.17mm. The rack angle of the cutter was fixed at 15 degree. Figure 4.4 shows the setup for the case with depth of cut of 1 mm. The cutting depth started at 0.2mm for small intrinsic length scale sample, and was increased at an interval of 0.2mm until the failure mode transition was identified. But for the larger intrinsic length scale sample, the starting depth of cut was set greater. For example, for the case in which the fracture energy was 17.5 Jm^{-2}, or that the characteristic length was 16 mm , when the cutting depth reached 0.6mm the rock failed mainly by crushing along with small chipping; but significant chipping was observed when the depth of cut was 0.8mm, and d_c was determined to be 0.8mm. Figure 4.5 shows the snapshots of the analysis around the transition depth.

Figure 4.6 summarizes the results from numerical modeling together with three data points processed with the size effect law from Figure 4.2.

A linear relationship between the critical transition depth d_c versus l_{ch}/B_1^2 was obtained with R^2=0.90 as follows,

$$d_c(mm) = 5.4\frac{l_{ch}}{B_1^2} \tag{4.15}$$

This result affirms that the critical transitional depth is indeed directly related to the intrinsic length scale.

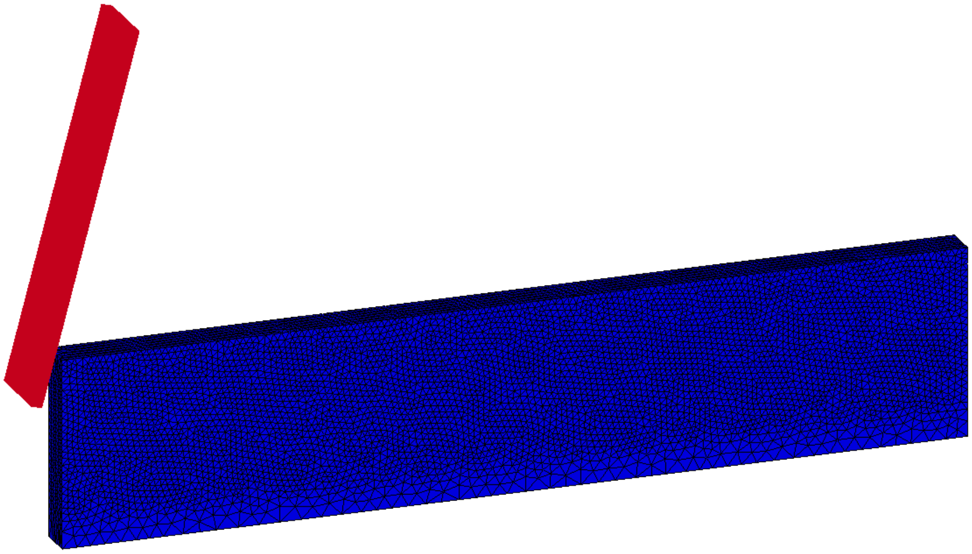

Figure 4.4 A typical FEM model setup for a slab scratch test

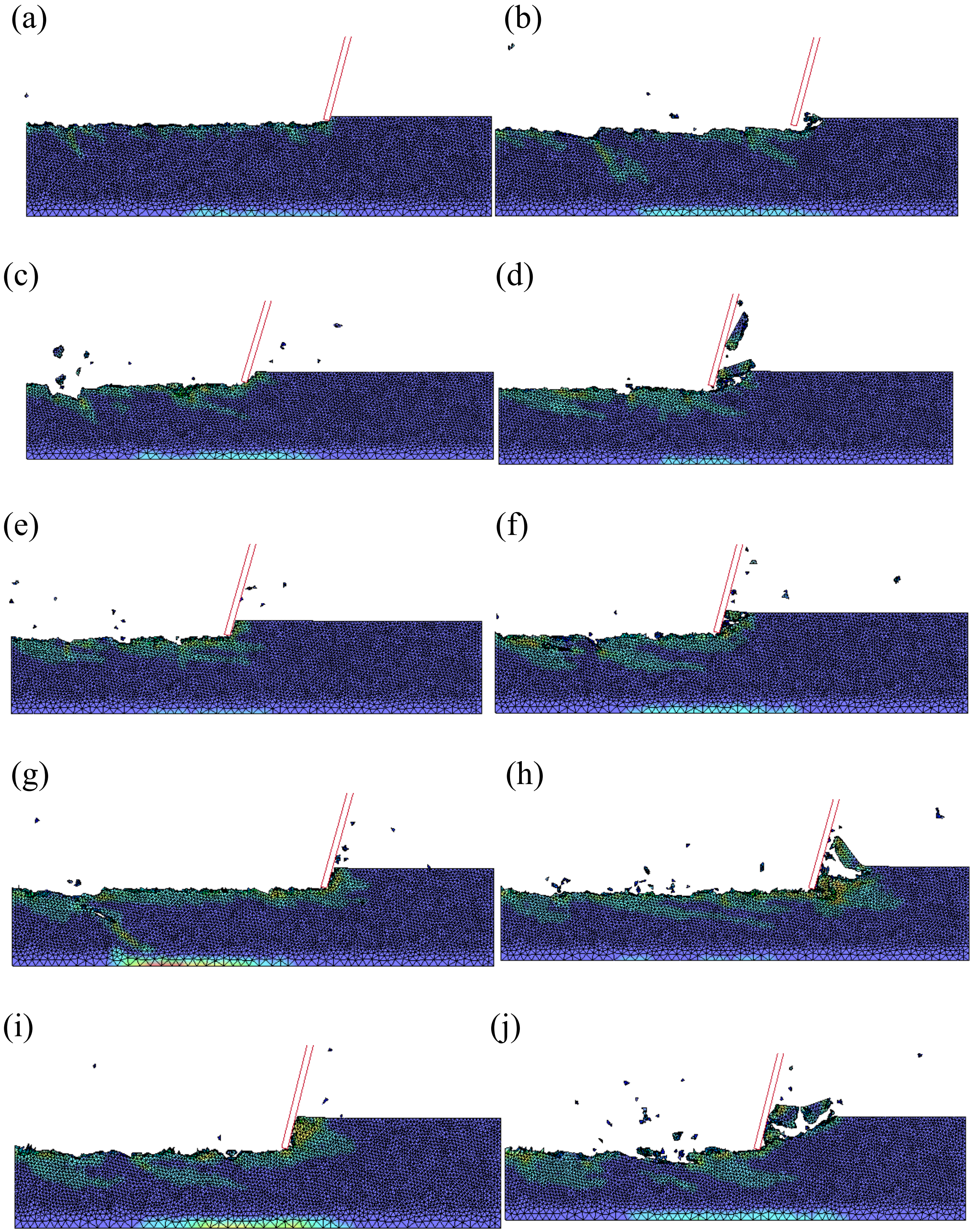
(a)
(b)
(c)
(d)
(e)
(f)
(g)
(h)
(i)
(j)

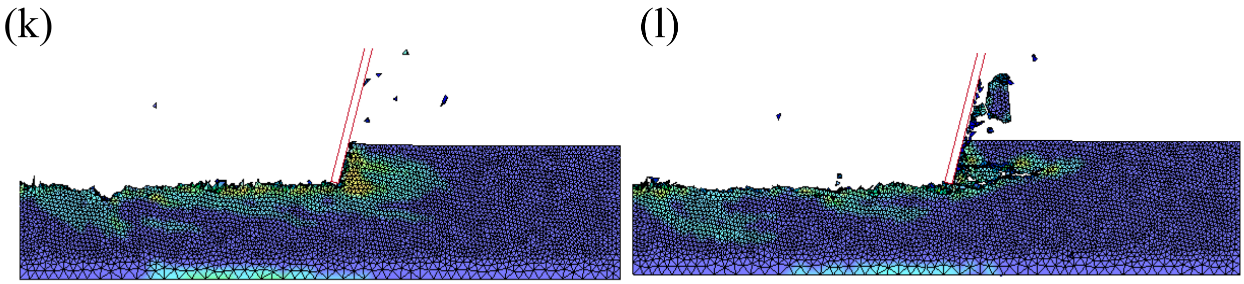

Figure 4.5 Damage for rocks with different fracture energies at various cutting depths (a) G_{ft}=8.8Jm^{-2}, d=0.2mm, (b) G_{ft}=8.8Jm^{-2}, d=0.4mm, (c) G_{ft}=17.5Jm^{-2}, d=0.6mm, (d) G_{ft}=17.5Jm^{-2}, d=0.8mm, (e) G_{ft}=26.3Jm^{-2}, d=0.8mm, (f) G_{ft}=26.3Jm^{-2}, d=1.0mm, (g) G_{ft}=35.0Jm^{-2},d=1.0mm, (h) G_{ft}=35.0 Jm^{-2}, d=1.2mm, (i) G_{ft}=43.8 Jm^{-2},d=1.4mm, (j) G_{ft}=43.8 Jm^{-2}, d=1.6mm, (k) G_{ft}=52.5Jm^{-2},d=1.4mm, (l) G_{ft}=52.5Jm^{-2}, d=1.6mm

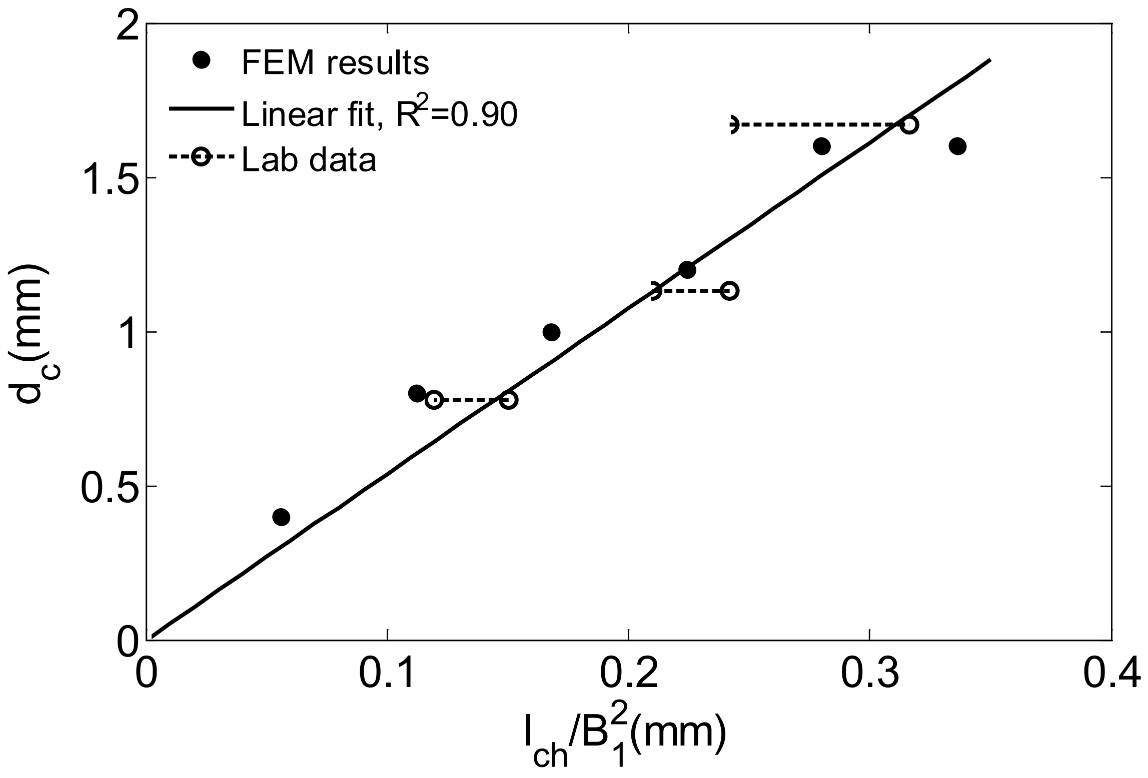

Figure 4.6 The critical transition depth as a function of l_{ch}/B_1^2

In comparing with the trend from three laboratory test data points, we have employed an empirical equation to be discussed later to obtain B_1^2 from σ_c. Also there were uncertainty regarding σ_c for the test data. The reported σ_c values for Vosges sandstone, Berea sandstone and Rhune sandstone were 28, 39 and 89MPa, respectively [6]. It was not clear if these strengths were determined on the same batch of samples used in the cutting tests. Therefore, the cutting specific energies from Figure 4.1 were also used as estimates of σ_c [5, 7], and they were found to be 15.2, 28.4 and 144 MPa, respectively. We used these two sets of σ_c as a potential range of the actual values. Each of the test data point was therefore marked on Figure 4.6 as a range on l_{ch} for a given d_c value.

4.5 TRANSITION DEPTH AS A FUNCTION OF ROCK UNIAXIAL COMPRESSIVE STRENGTH

It is much easier to determine the strength properties of rock than to obtain its fracture properties. Chaput [3] has shown that the transition depth reduces when the uniaxial compressive strength increases, as reproduced in Figure 4.7, where the rocks are sorted along the vertical axis by increasing strength. In the plot, the boundary between the secondary and the primary chipping represents transition from ductile to brittle mode of failure. This plot motivated us to investigate a conversion of Eq. (4.13) into a relationship between the critical transition depth and the uniaxial compressive strength. This is feasible if relationship could be established between K_{IC} and σ_t, and between B_1^2 and σ_c. Indeed, there exists a rich literature in relating K_{IC} to σ_t, and all were posed in a linear form: Gunsallus and Kulhawy [87] found a linear relationship between K_{IC} and σ_t for several types of rock; Bhagat [88] obtained one for coal; Harison et al. [89] proposed one for some soft rocks based on experiments by Haberfield and Johnston [90].

Using available experimental results from various kinds of rocks and coals, Whittaker et al. [84] obtained the following empirical equation,

$$\sigma_t = 9.35 K_{IC} - 2.53 \tag{4.16}$$

Where the unit of K_{IC} is MPa.m$^{0.5}$, the unit of σ_t is MPa.

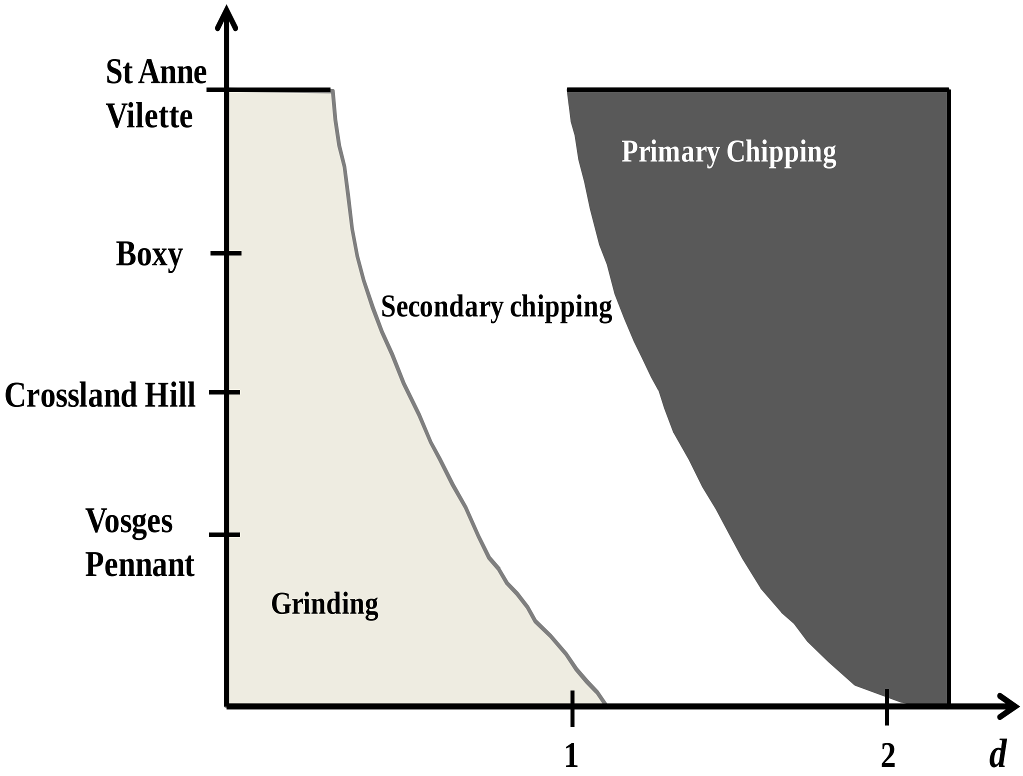

Figure 4.7 Failure mode transition as a function of depth of cut and rock strength [3]

Zhang [91] argued that the intercept of should be set to zero in regression, as rocks that had no tensile strength rock could not have fracture toughness. As such, he obtained the following equation, reproduced in Figure 4.8, with data from [84, 92-95]

$$\sigma_t = 6.88 K_{IC} \tag{4.17}$$

This empirical equation was employed in this study. One would expect a large data scatter around such empirical relationship as attested by Figure 4.8. Using the original data, we found the R^2 to be 0.78.

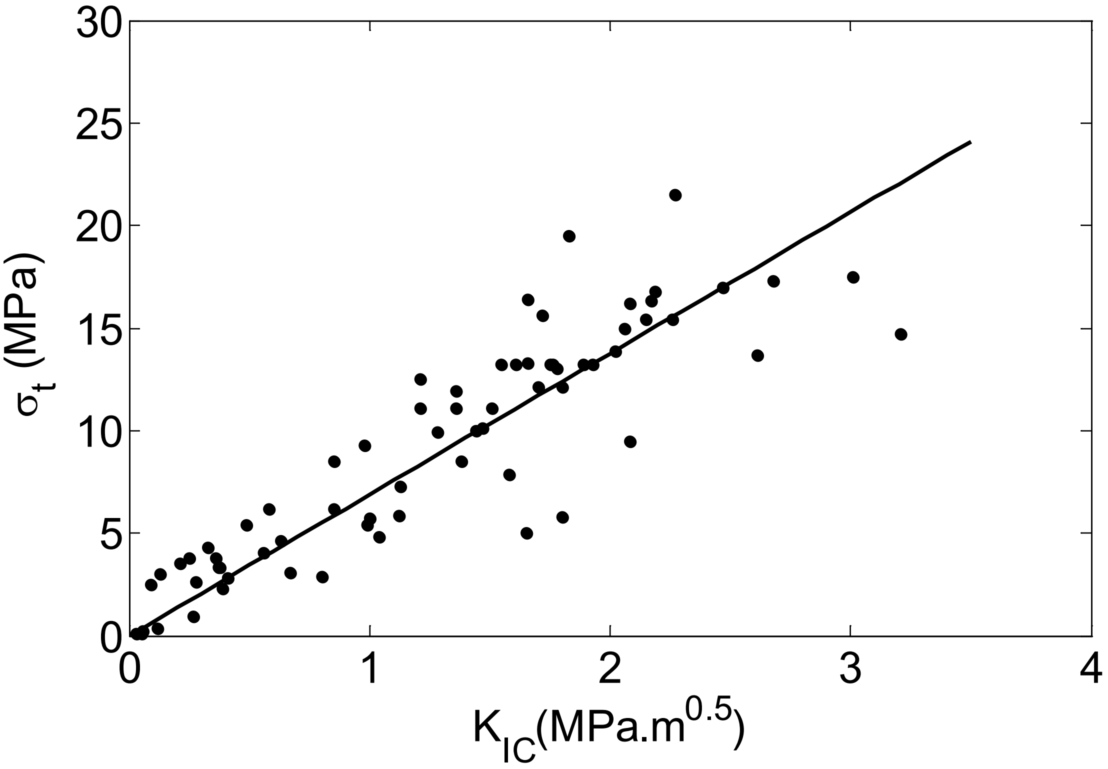

Figure 4.8 Relationship between fracture toughness and tensile strength [94]

As for the relationship between B_1^2 and σ_c, this study used about 200 samples from a wide variety of sources [96-107], and obtained a relation between B_1^2 versus σ_c. Through a linear regression in bilogarithmic scale, see Figure 4.9, we obtained, with a large scatter as reflected in a R^2 of only 0.25, the following

$$(\sigma_t/\sigma_c)^2 = 0.05\sigma_c^{-0.43} \tag{4.18}$$

Where σ_c is expressed in MPa.

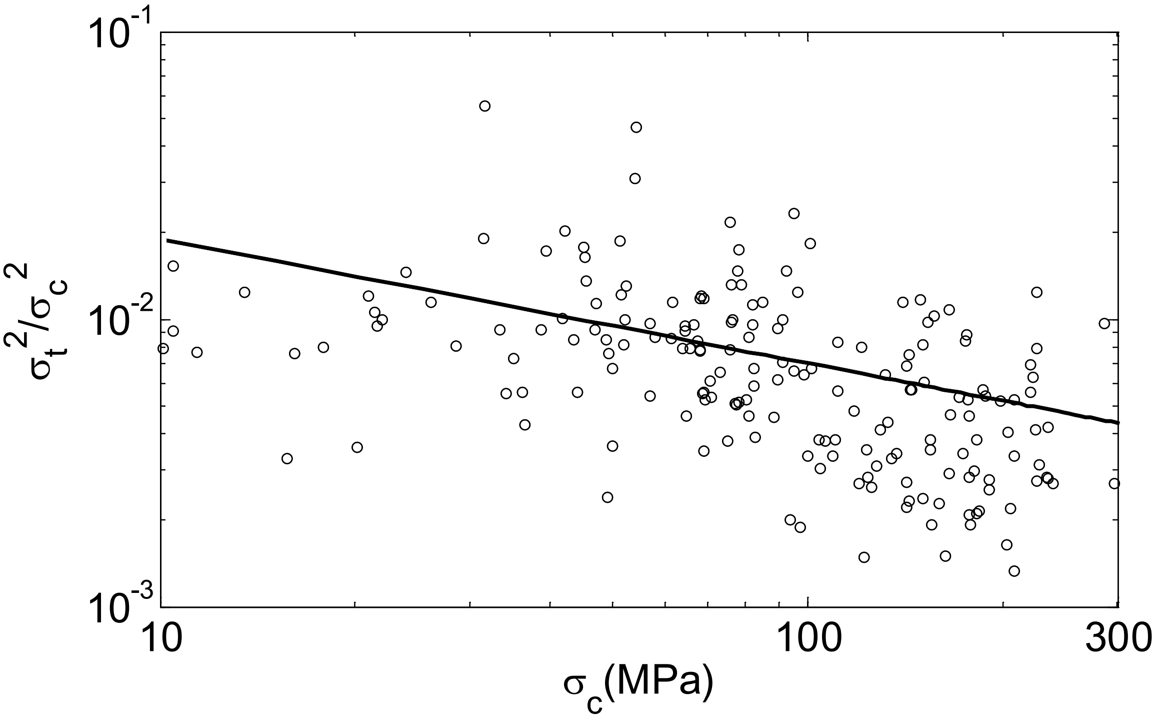

Figure 4.9 The Brittleness as a function of the uniaxial compressive strength.

Substituting Eqs. (4.10), (4.17), (4.18) into Eq. (4.11), the intrinsic length scale, l_i, in mm, was converted to a function of σ_c, in MPa, as follows,

$$l_i = \frac{1.06}{\pi}\sigma_c^{-0.43} \tag{4.19}$$

The critical transitional depth, d_c, being proportional to intrinsic length scale, became proportional to a fractional power of the uniaxial compressive strength as follows,

$$d_c \propto \sigma_c^{-0.43} \tag{4.20}$$

To obtain the proportionality constant of the above equation, we used results from the FEM computation. Among the FEM cases analyzed, only that from the baseline case was employed as it represented a realistic rock, i.e., the case with σ_c=36 MPa, G_f=35 Jm^{-2} in which l_{ch}= 32 mm and B_I=12 from Eqs. (4.6) and (4.12). Using this data point alone, we obtained,

$$d_c = 5.6\sigma_c^{-0.43} \qquad (4.21)$$

Where the units of d_c and σ_c are mm and MPa, respectively.

How does this relationship compare with real test data? The three samples from Figure 4.1 were again employed. Again due to the uncertainty in σ_c, each of the laboratory test data point was marked on Figure 4.10 with a range on σ_c for a given d_c value. The data appeared to support the trend posed by Eq. (4.21), albeit that they also pointed to the potential of a large variability as would be expected.

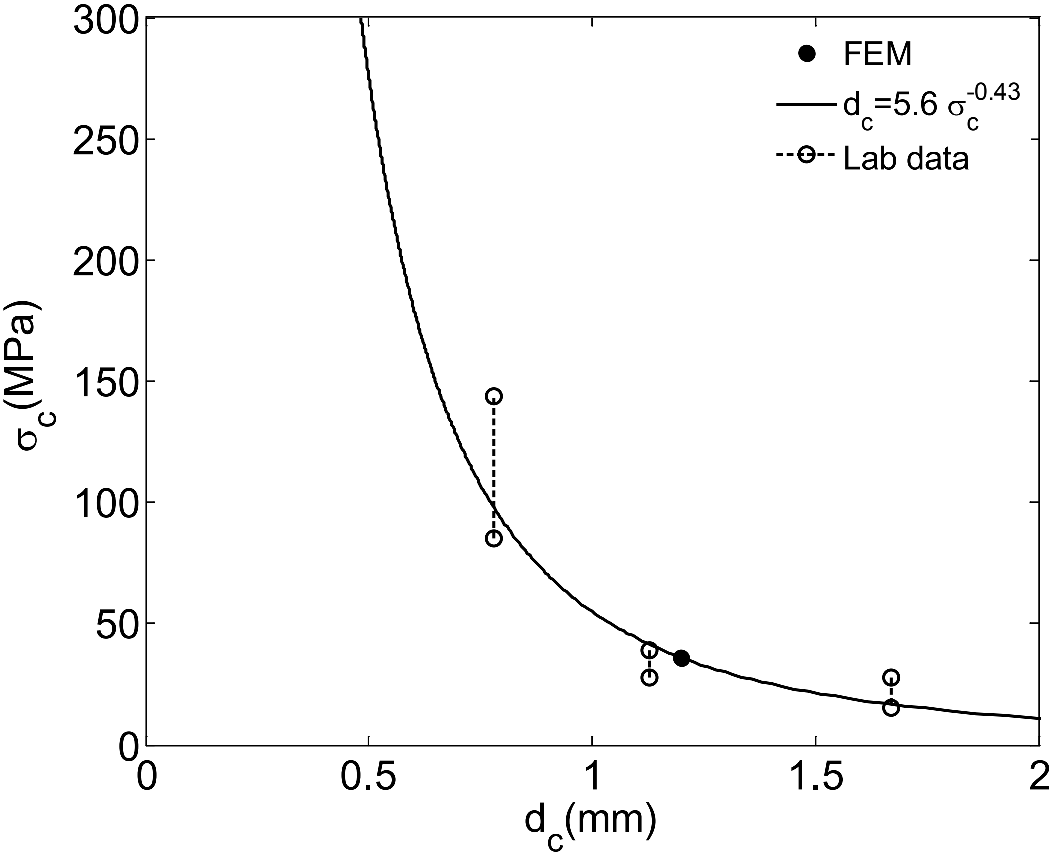

Figure 4.10 The critical transition depth as a function of rock strength

4.6 CONCLUSIONS

By treating the depth of cut as the scale of similarity, this study showed that the rock cutting follows Bažant size effect law for quasibrittle material. The critical transition depth from ductile to brittle failure can be obtained by fitting cutting data with the size effect law.

The intrinsic length scale, proposed by Huang and Detournay, was shown to be a contrast between ductileness and brittleness, where the ductileness could be represented by Hillerborg's characteristic length, and the brittleness by the ratio of the square between the compressive strength and the tensile strength. This contrast became the basis of using FEM modeling to obtain a linear relationship between the critical transition depth and the characteristic length. By further obtaining an empirical relationship between the brittleness and the uniaxial compressive strength, a relationship between the critical transition depth and the uniaxial compressive strength was also presented. The trend from three laboratory test data points appeared to support such a relationship, but they also pointed to potentially significant inherent variability.

The two relationships so derived manifest the general trend regarding the critical transition depth with respect to the intrinsic length scale and the uniaxial compressive strength, respectively. With limited data, they are perhaps best be viewed as an illustration of a potential framework to obtain critical transition depth as presented in this study.

5.0 MODELING GROOVE CUTTING IN ROCKS USING FINITE ELEMENTS

5.1 INTRODUCTION

In an effort to establish the modeling framework of rock cutting within the finite element method, laboratory rock scratch tests has been successfully modeled [29]. It has been demonstrated that the Lagrangian FEM approach was capable of modeling the rock fragmentation progression from crack initiation, to chip formation, to the interactions of chips, cutter, and the rock sample. In particular, two failure modes as observed in the laboratory tests were reproduced by FEM: the ductile failure for shallow cuts and the brittle failure for deep cuts. The cutting modeled was slab cutting, in which the width of a cutter was the same as that of the rock sample. The problem was essentially a two dimensional one. In an effort to model the cutting action of a drilling bit, this study expanded research into the modeling of groove cutting by a single polycrystalline diamond compact cutter. The cutter had a narrower width and cut beyond the immediate contact area, both laterally and along the depth. A clear difference between slab cutting and groove cutting was the lateral cutting of the latter, resulting in a larger specific energy in groove cutting [6, 8].

To provide an accurate estimate of the cutting force, it was essential to capture the volume of cut. It turned out that the volume of cut was sensitive to the mesh size used in a finite element modeling. This study thus first investigated the mesh-size conditions. Also affecting the results of an analysis was the number of elements in contact with a cutter. After establishing preliminary guidelines, numerical experiments were conducted on groove cutting using both rectangular and disc cutters. Finally, a circular cutting model, albeit preliminary, was also developed.

5.2 MODELING CONSIDERATIONS

The core considerations of the finite element modeling effort were:

- The bottom, right, and left surfaces of the rock piece are treated as “non-reflecting” boundaries, which allow stress waves to be dissipated instead of being reflected, thus there is no such boundary effect affecting the stress distribution near the edges of the model.
- Nodes on the front and rear faces were constrained to ensure lateral confinement.
- The Continuous Surface Cap Model (Mat159) in LS-DYNA [57] was adopted to model the rock behavior. The material parameters were calibrated based on the experimental results of Vosges Sandstone [64].
- Rock fragmentation was modeled via removal of elements that had been subjected to a high level of damage. The procedure is known as element erosion.
- The study modeled sharp cutters and a coefficient of friction of 0.0 or 0.30 was used at the cutter-rock interface [108]. Cutting velocity was 4 m/s, with a force-sampling rate of 25 data/mm.
- The mesh of rock sample was originally generated by LS-PrePost using pyramidal elements, and then refined in the top by ANSYS. Randomness was desirable in element size

distribution and element orientation. The quality of mesh size was vital to the accuracy of result.

5.3 LATERAL REFINED ZONE REQUIREMENT FOR THE GROOVE CUTTING

During a groove cut, a cutter plows through rock over some lateral distance from its edge. Before a judgment can be rendered on the adequacy of a finite element mesh, an understanding of the lateral reach of a cutting action had to be established. A numerical experiment focusing on the influence of the lateral distance on the cutting specific energy was designed. In our design, the right side of the sample was the widest at 10 mm, which gradually tapered down toward the left to 2 mm. The geometry of the sample and the mesh employed is shown in Figure 5.1. The average mesh size in the fine zone was 0.2mm. The depth of cut was 1mm, the width of the cutter was 2 mm, and the lateral extent of the sample from the edges of the cutter ranged between 0 to 4 mm.

Figure 5.2 shows the damage, as well as the post cutting configuration of the sample. It was clear that lateral damages was confined within a strip zone with a width of w_a=1 mm, which was about five times the average element size from the edge of the cutter. Figure 5.3 depicts the history of the original specific energy and its moving average. The horizontal axis was the lateral extent of the rock sample from the edge of the cutter at the time the energy was computed. The moving average shows that the specific energy increased when lateral distance increased and that it was approximately constant if the lateral distance exceeds five times of the element size.

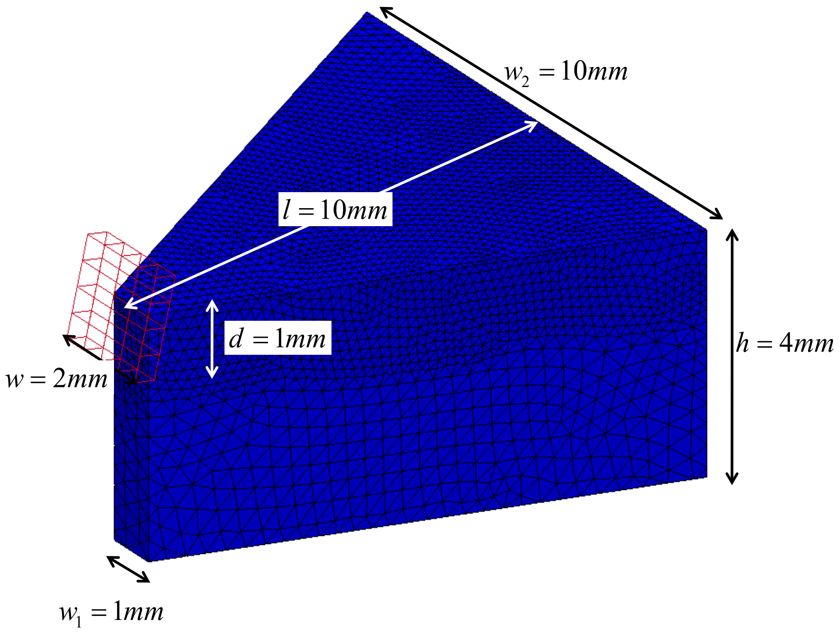

Figure 5.1 Groove cutting with different lateral distance

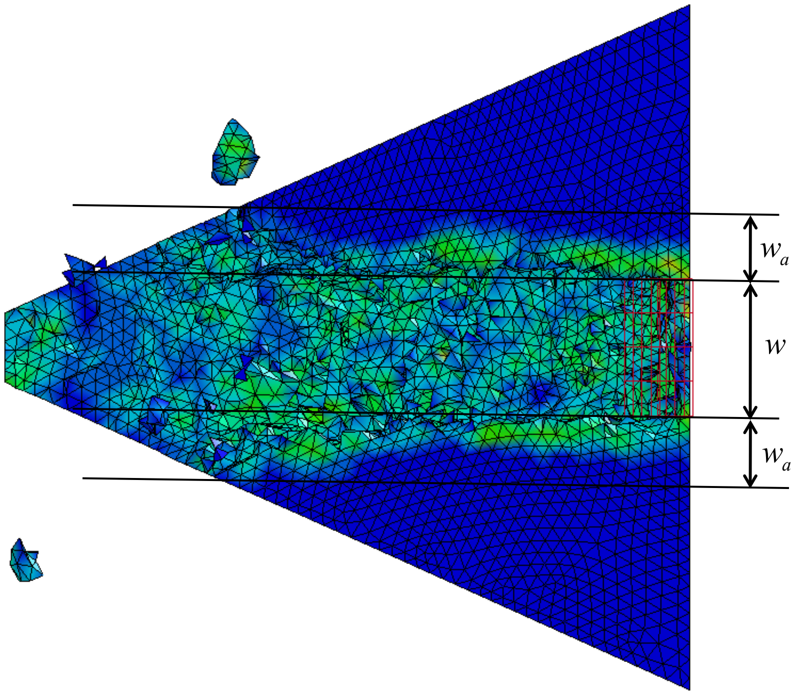

Figure 5.2 Affected lateral distance in groove cutting

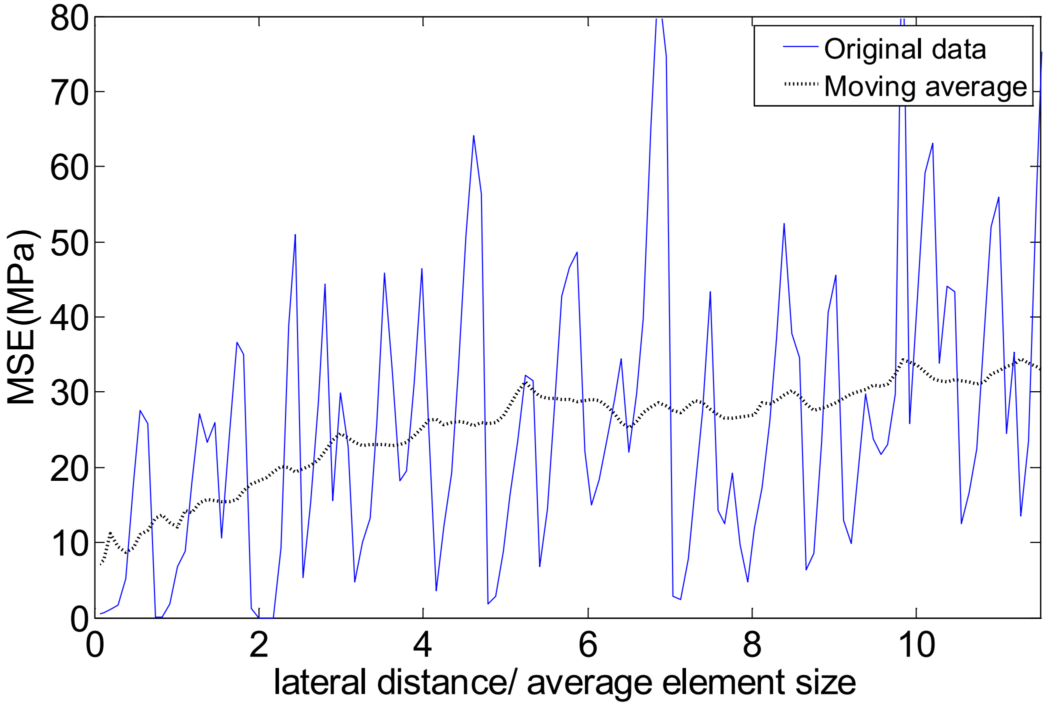

Figure 5.3 Log of specific energy with different lateral distance (the width of moving average is three times average element size)

5.4 SYMMETRY CONSIDERATIONS

Whenever possible, in an orthogonal cutting, one would employ the symmetry conditions and only analyze half of the problem, in order to reduce computational cost. Aside from the necessity of using enough small elements to guarantee an accurate solution, one might ask if there were any unexpected consequences stemming from the application of symmetry conditions. To answer this question, a numerical experiment was carried out. Figure 5.4 shows both a half model and a full model: the full model was generated by reflecting the half model across an XY plane. The average mesh size in the fine zone was 0.2mm. The cutting width was 6mm and the cutting depth was 1mm.

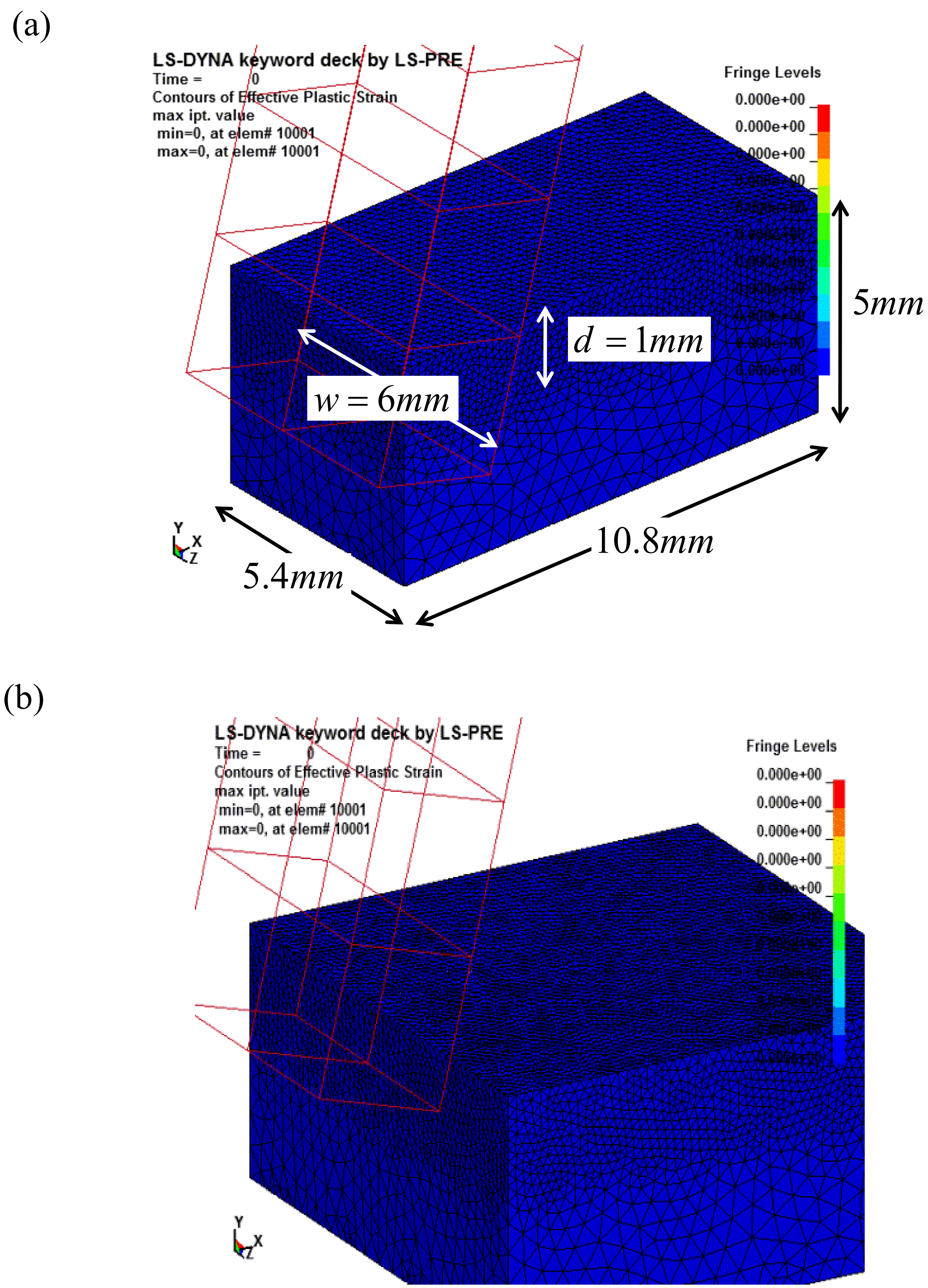

Figure 5.4 A half model and a full model (a) a half model (b) a full model

Figure 5.5 gives the force histories of these two models; the average forces were 0.103kN and 0.099kN, and the standard deviations of the force were 0.076kN and 0.052kN, respectively. By imposing symmetry conditions, the resulting cutting forces were close. But a greater difference was measured in the fluctuation of the forces. The full model gave a lower coefficient of variation at 0.53, while the half model gave a higher coefficient of variation at 0.74. The full model encountered more elements, and the total force was the average of a larger number of elements, and thus resulted in a smaller fluctuation. In the present study, these differences were deemed insignificant.

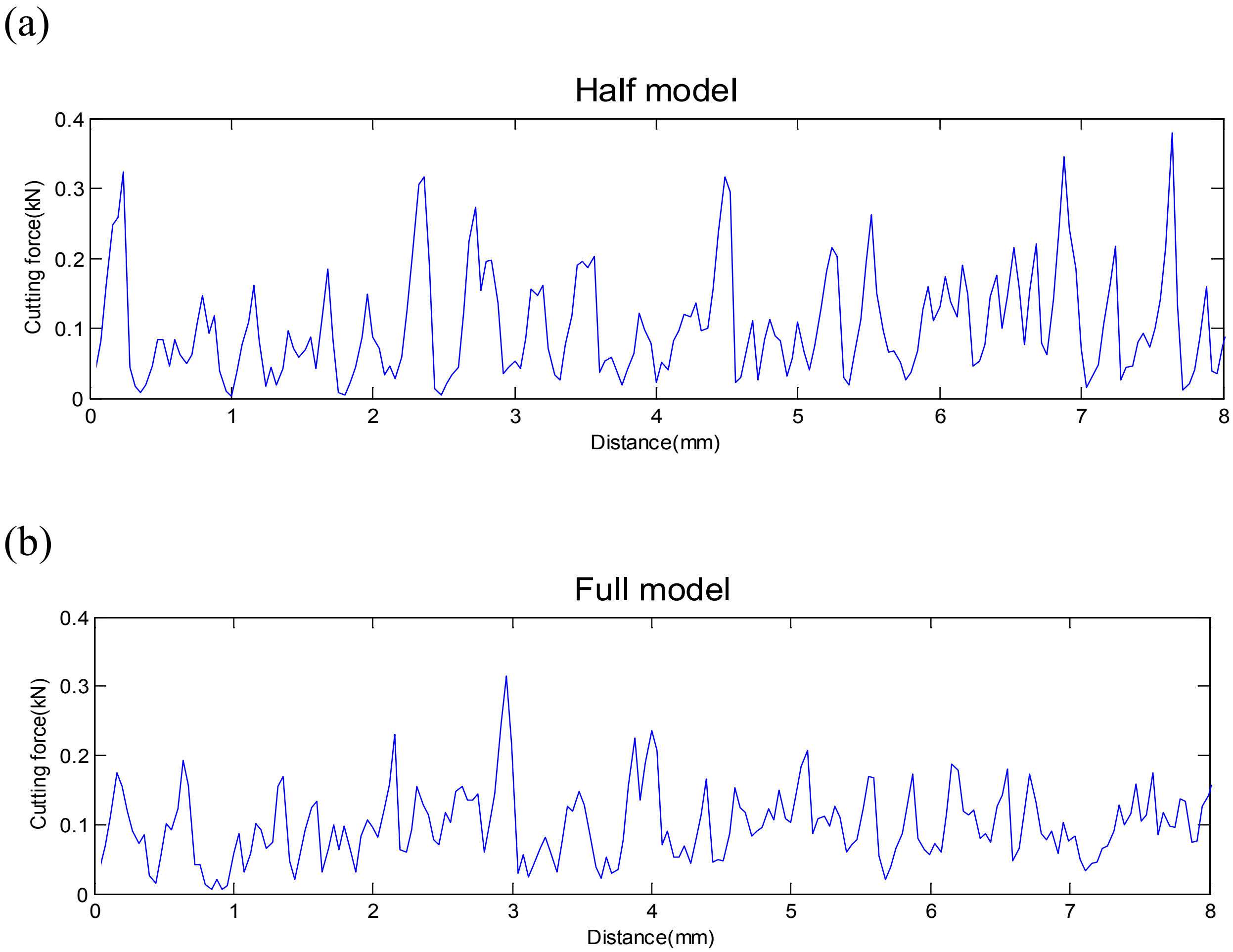

Figure 5.5 Cutting force for a half model and a full model(a) a half model (b) a full model

5.5 SPECIFIC ENERGY EVOLUTION IN GROOVE CUTTING FOR THE RECTANGULAR CUTTER

Having confirmed the validity of imposing the symmetry conditions, we moved on to model groove cutting. In order to investigate the influence of cutter width with respect to cutting depth, namely, the influence of *w/d* ratio, on the specific energy in groove cutting, a total of five groove cuts were conducted using the same cutting depth while varying the cutting width. The cutting depth chosen was 0.6mm, which corresponded roughly to 6 layers of the elements, to ensure sufficient resolution in a ductile failure mode cutting [19]. The cutting widths increased from 1.2 mm to 3.6 mm at an interval of 0.6mm. A full model of the rock sample was only adopted for the case where the width equaled 1.2 mm to ensure an adequate number of elements made contact with the cutter, while for all the other cases only half models were used.

Figure 5.6 presents the mesh of groove cutting for the case where *w/d* equaled 2. A fine mesh with average element size of 0.11 mm formed the top 1.5 mm of the sample, while a coarse mesh with an average element size of 0.5 mm was used for the rest. Figure 5.7 depicts the mesh for all the other groove cutting cases, where fine mesh was limited to a zone of 0.8 mm in depth and 2.2 mm in width. The lateral distance in all cases exceeded six times that of the average element size. The cutting force history and a snapshot for the case where *w/d*=2 are shown in Figure 5.8; the average cutting force was 0.023KN, and the specific energy was 32.5MPa. The cutting forces for the cases that *w/d*=3, 4, 5 and 6 were all obtained based on the mesh in Figure 5.7. The cutting force history and a snapshot for the case where w/d=4 are shown in Figure 5.9; the average force was 0.038kN, and the specific energy was 26.5MPa. The slab cutting was carried out based on the mesh of Figure 5.6. Its cutting force history and a snapshot are shown in Figure 5.10; the average force was 0.039kN and the intrinsic specific energy was 21.4MPa.

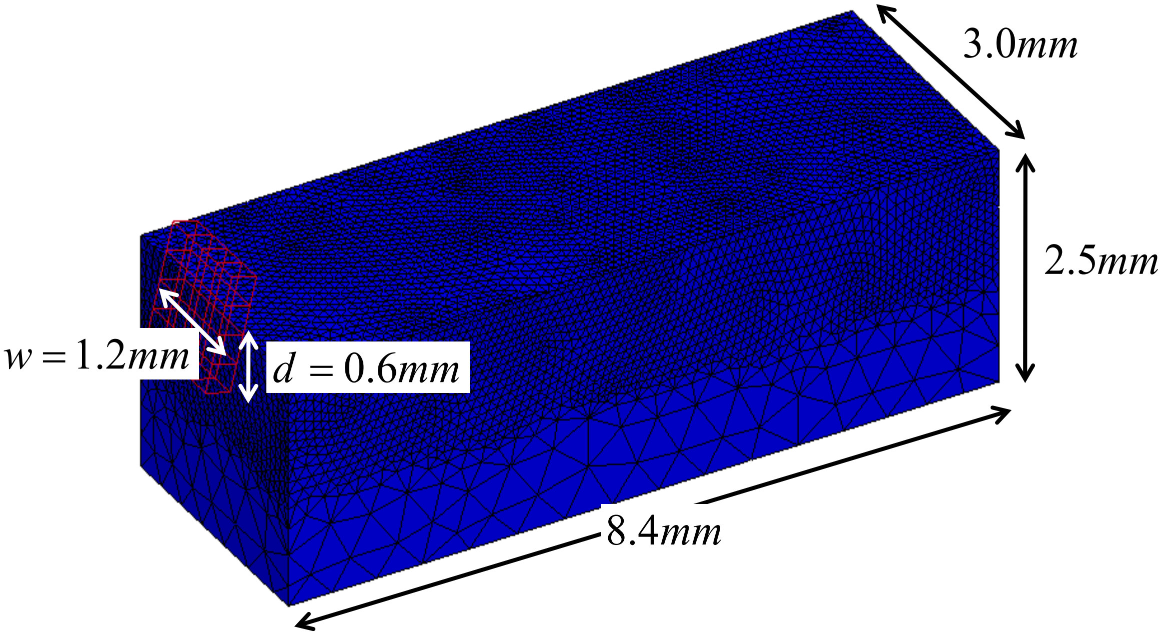

Figure 5.6 Geometry and mesh used in grooving cutting with *w/d*=2

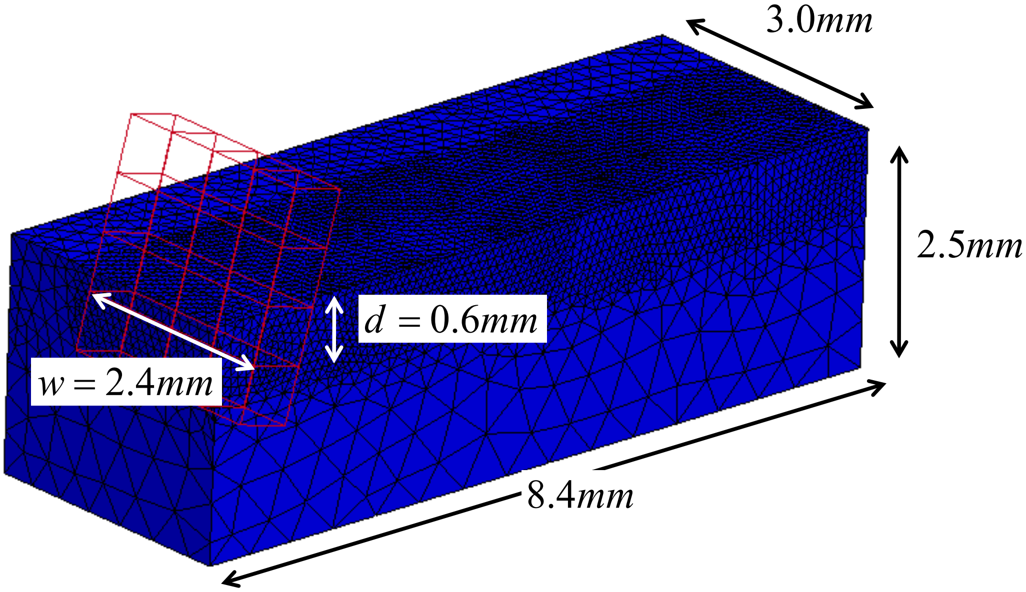

Figure 5.7 Geometry and mesh used in grooving cutting with *w/d*=3,4,5,6

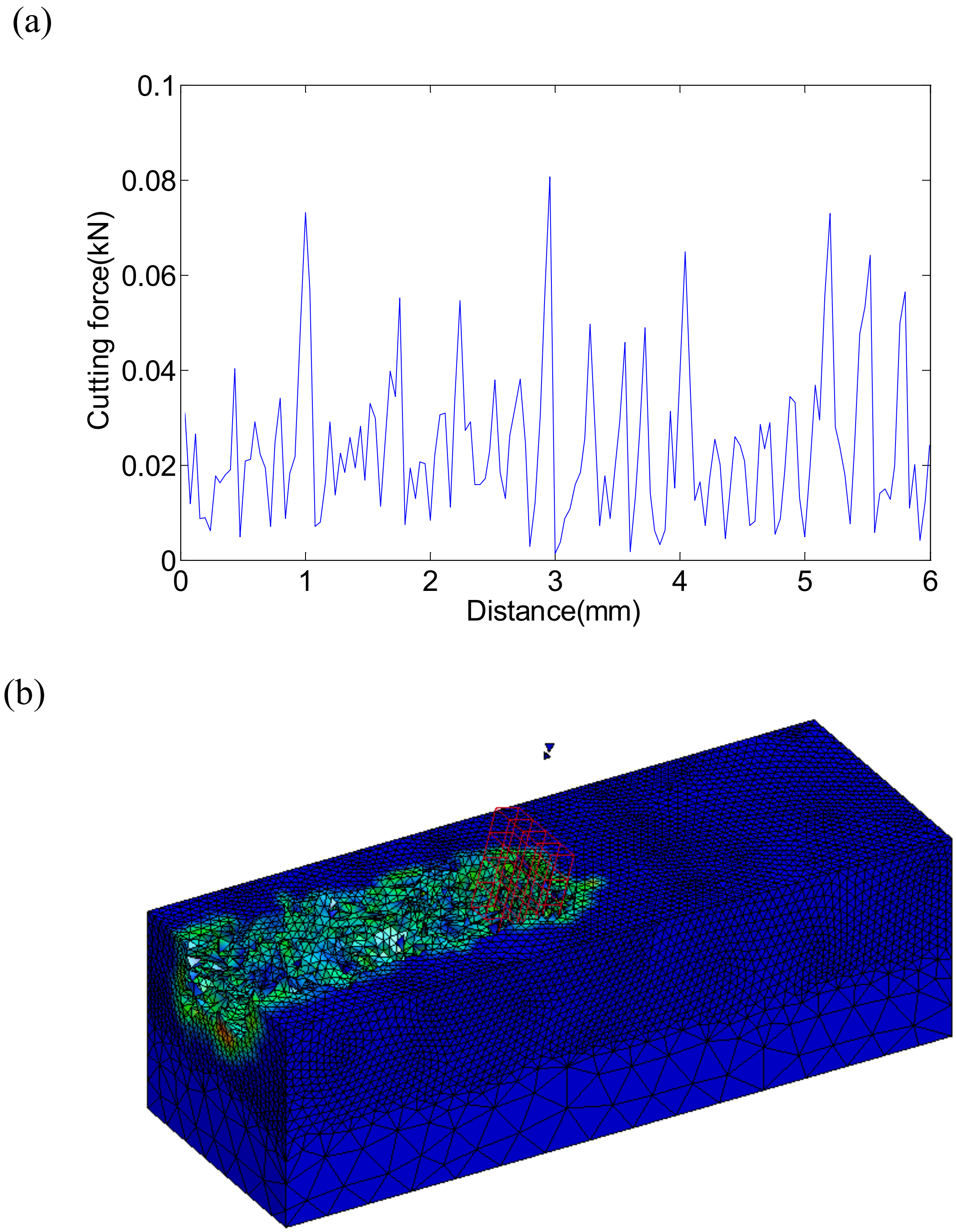

Figure 5.8 Cutting force and a snapshot of damage in grooving cutting with *w*/*d*=2 (a) cutting force history (b) a snapshot

(a)

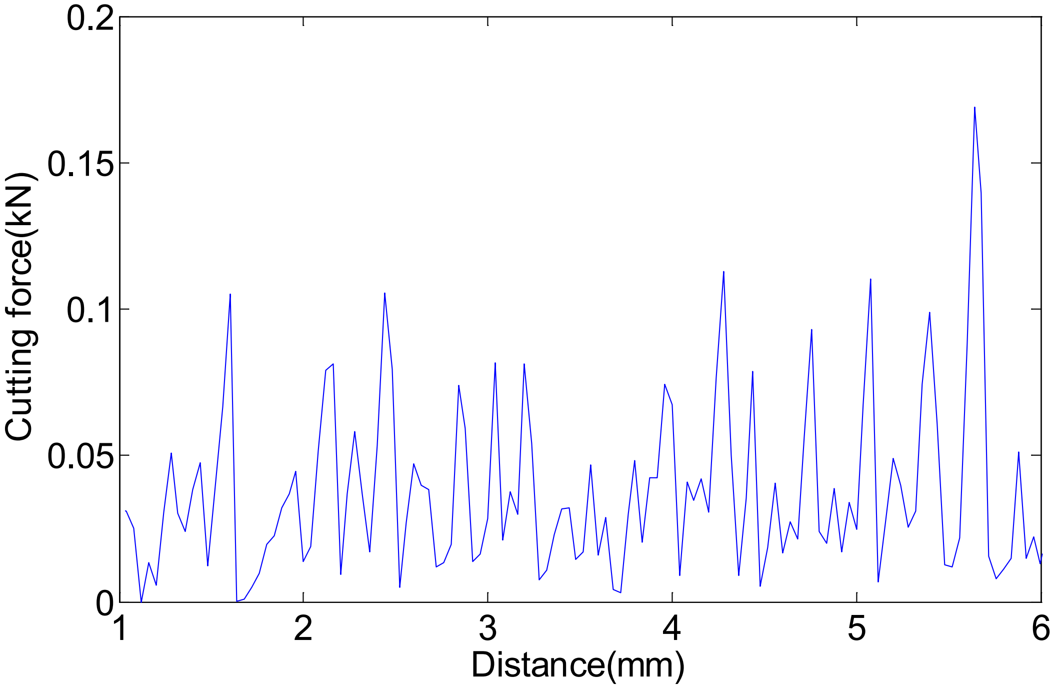

(b)

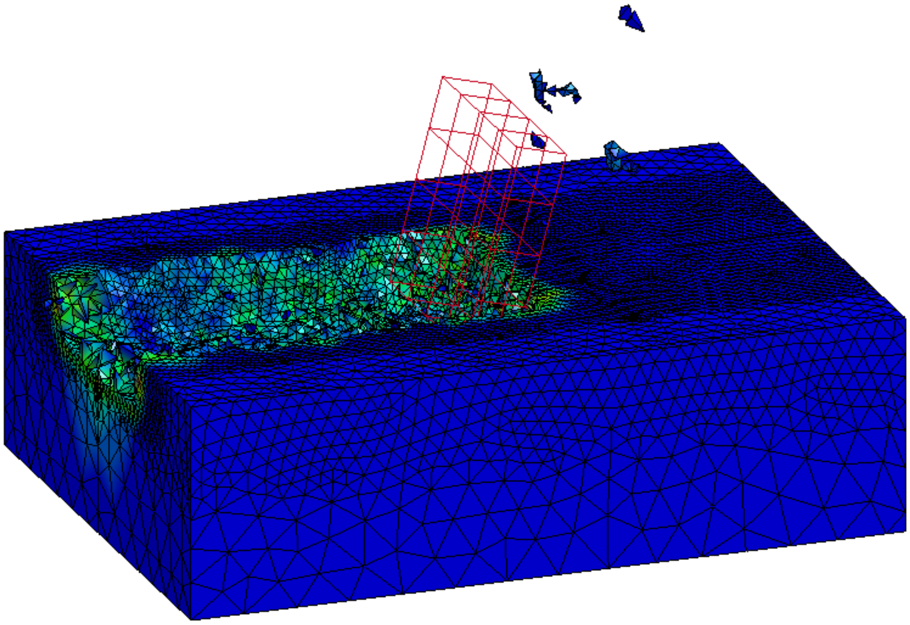

Figure 5.9 Cutting force and a snapshot of damage in grooving cutting with *w/d*=4 (a) cutting force history (b)snapshot

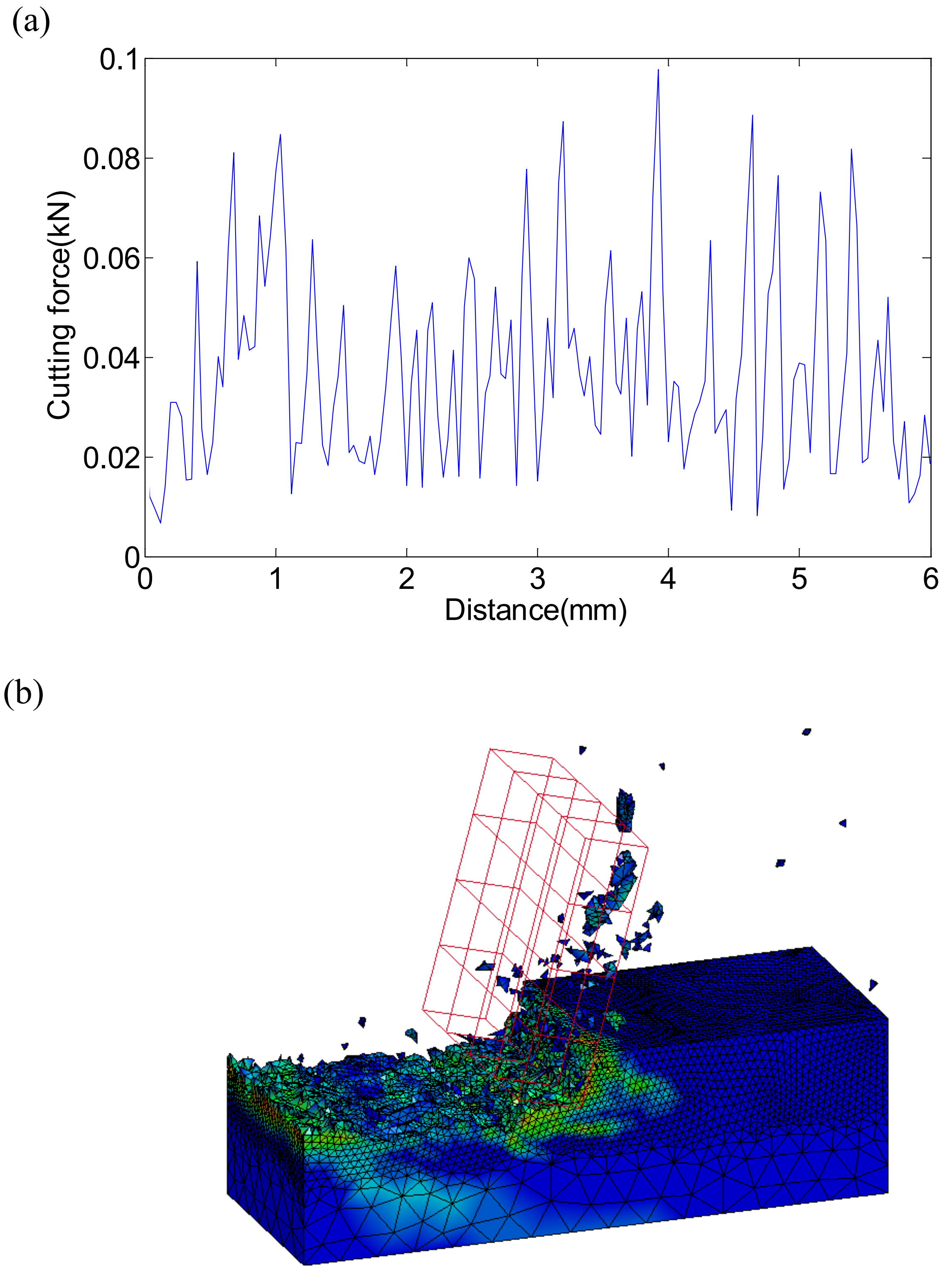

Figure 5.10 Cutting force and a snapshot of damage in slab cutting (a) cutting force history (b)snapshot

A summary of the cutting force and specific energy for all the groove cutting cases as well as a slab cutting is shown in Table 5.1.

Table 5.1 A summary of cutting force and specific energy

	w/d	Average force(kN)	Force standard deviation (kN)	Specific energy(MPa)
Groove cutting	2	0.0234	0.0155	32.5
	3	0.0310	0.0262	28.7
	4	0.0382	0.0276	26.5
	5	0.0478	0.0272	26.6
	6	0.0480	0.0346	22.2
Slab cutting		0.0386	0.0196	21.4

The evolution of the specific energy versus *w/d* is shown in Figure 5.11. It agreed with the experimental results in Vosges sandstone, by observing that the specific energy decreased with *w/d* and showed a tendency to converge to the intrinsic specific energy in slab cutting. However, as the details of the mechanical properties of laboratory data were not available, the comparison can be viewed as qualitative. In the simulation, the specific energy in the slab cutting is smaller than the uniaxial compressive strength, and this might result from the element erosion algorithm. As the rock elements were deleted after failure, thus the debris or plastic flow of crushed rock in front of cutter [41] would not be well modeled.

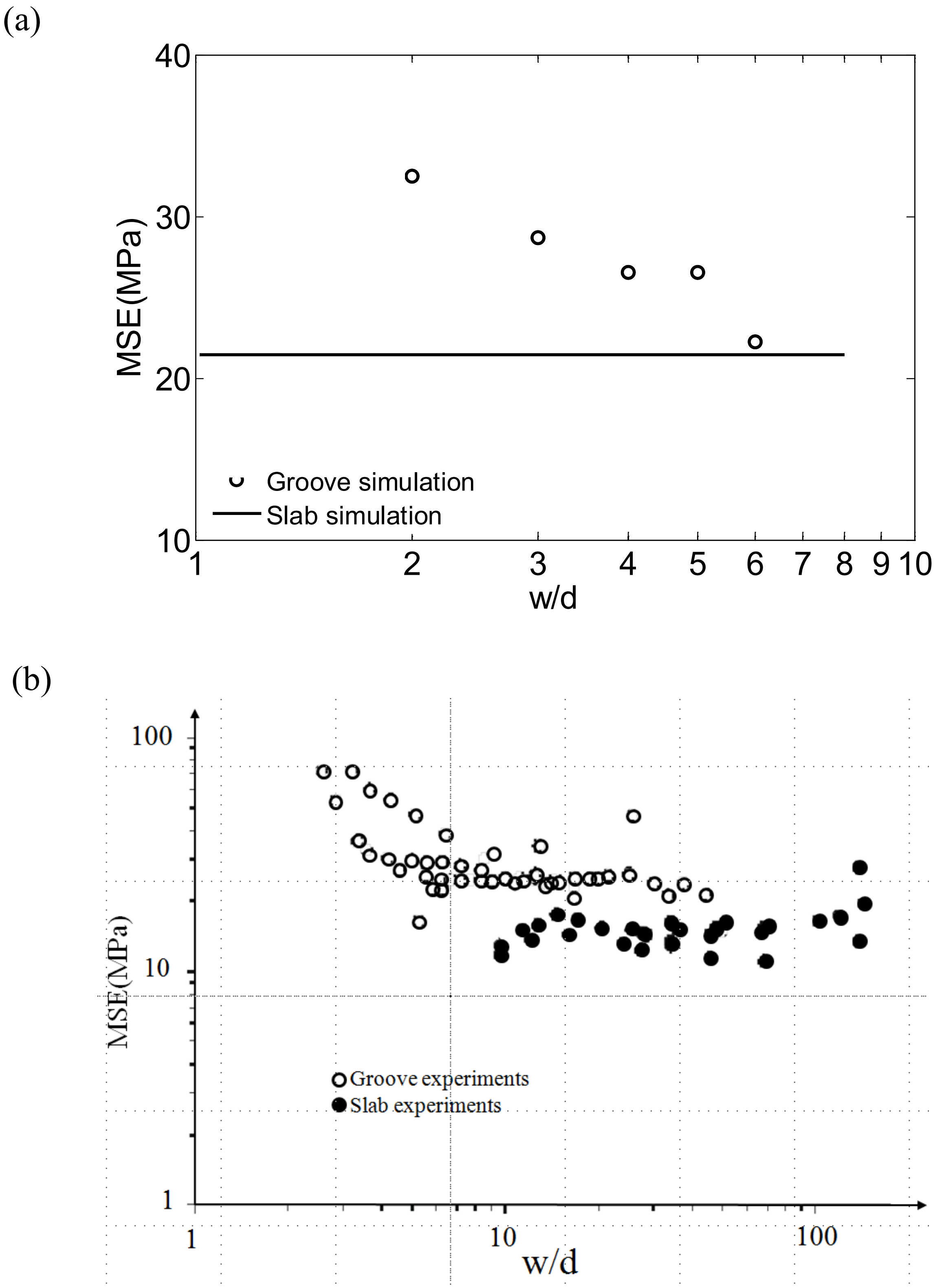

Figure 5.11 Evolution of the specific energy versus *w/d* (a) present modeling results. (b) experiments conducted in Vosges sandstone[6]

5.6 COMPARISON OF LINEAR CUTTING AND CIRCULAR CUTTING

As extensive calibration of material parameters and sensitivities analysis were based on linear cutting [29], it was desirable to establish the relationship between linear cutting and circular cutting. A numerical experiment was designed to compare the circular cutting and linear cutting, regarding the force and cutting volume, which were essential for MSE. The comparative experiment adopted the same cutter but different shape of rock sample. To save computation expense, only 1/8 of rock sample was modeled in the circular cutting, as shown in the shaded area in Figure 5.12

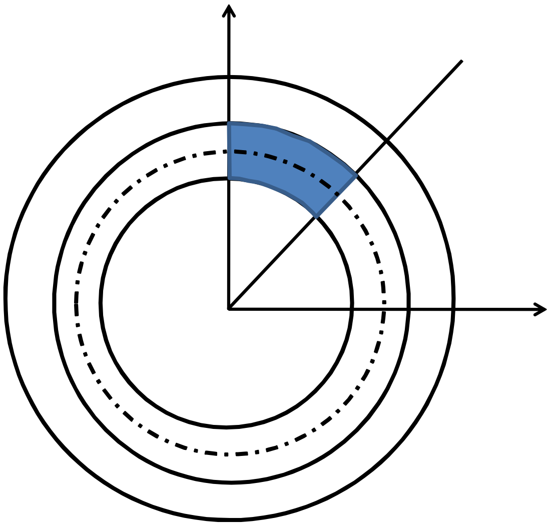

Figure 5.12 Sketch of rock sample for circular cutting

The diameter and thickness of PDC disc cutter was 13mm and 2mm, respectively. The rake angle of the disc cutter was 15^o. The mesh of rock sample was illustrated in Figure 5.13. For circular cutting, the width and average length of rock sample is 11mm and 23.4mm, respectively; the height is 3mm, with the top 2.5mm fine zone formed with the average mesh size of 0.25mm. The total number of tetrahedron element is 645,140. For the counterpart linear cutting, the dimension of rock sample was X*Y*Z=23.4mm*3mm*11mm, with a total number of 595,660 elements.

The horizontal velocity was fixed to be $v_x=v_\theta=4$m/s, while the vertical velocity of cutter was fixed to be $v_y=0.255$m/s, resulting in a linear increase of the cutting from zero in the left to 1.5mm in the right. As the maximum cutting width was 8.4 mm corresponding to the cutting depth of 1.5mm, the width of rock sample allowed a margin of at least five times mesh size beyond immediate contact area in the lateral direction.

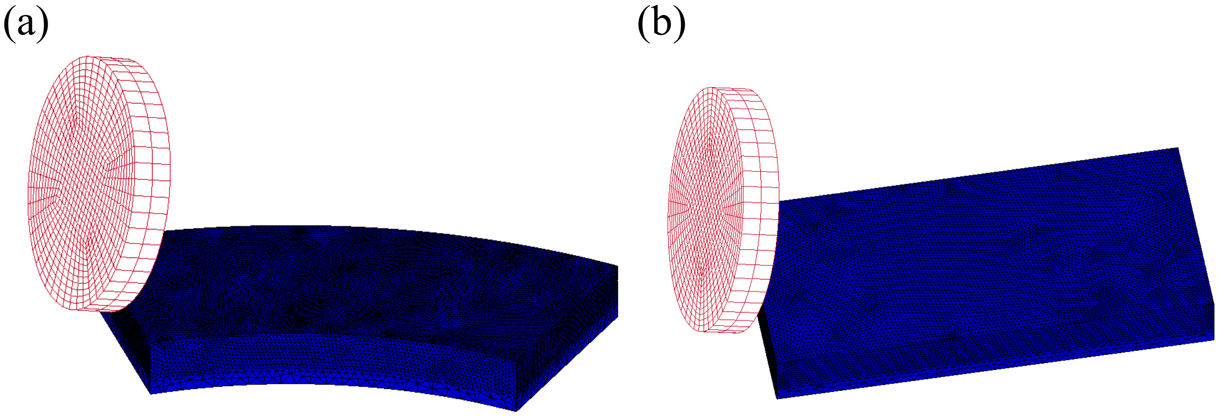

Figure 5.13 Geometry and mesh by a disc cutter (a) circular cutting (b)linear cutting

Figure 5.14 showed the damage as well as post cutting configuration. Figure 5.15 shows the histories of three force components. To eliminate the possible effect of boundary condition, only the middle part when depth is between 0.3mm to 1.3mm was plotted to compare. The cutting force was larger than the thrust force, and the side force was around zero. These trends agreed qualitatively with the laboratory test of circular cutting in ambient pressure environment [8]. To compare the forces components statistically, the average and standard derivation of three force components were summarized in Table 5.2. By comparing the force components of circular cutting and linear cutting, it turned out that they were almost identical.

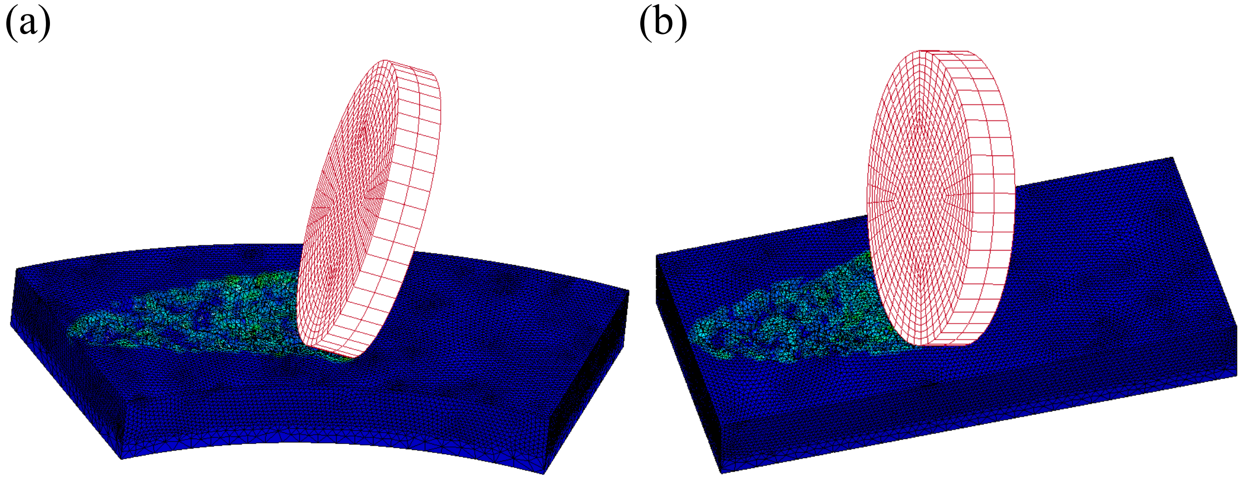

Figure 5.14 A snapshot of damage by a disc cutter (a) circular cutting. (b)linear cutting

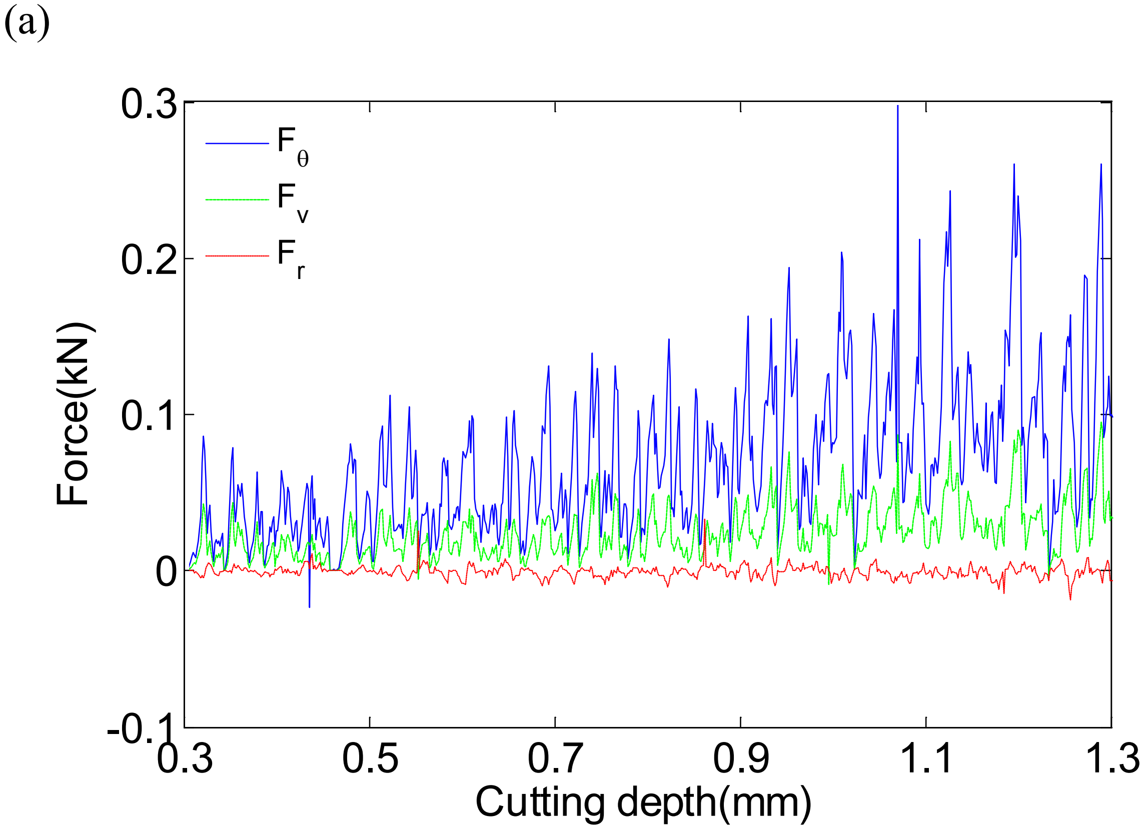

(b)

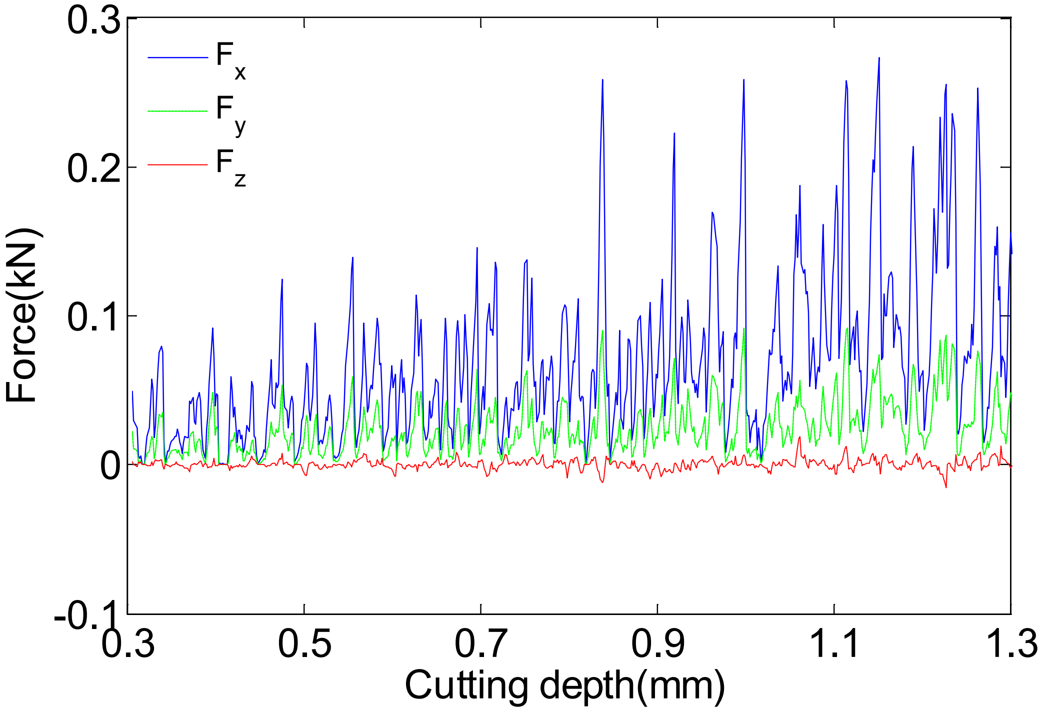

Figure 5.15 History of force componentsby a disc cutter (a) circular cutting (b)linear cutting

Table 5.2 Comparison of force components between circular cutting and linear cutting

Circular cutting			Linear cutting		
	average(kN)	standard derivation(kN)		average(kN)	standard derivation(kN)
F_θ	0.066	0.069	F_x	0.066	0.053
F_y	0.023	0.019	F_y	0.024	0.018
F_r	-0.001	0.005	F_z	0.000	0.003

Besides the force hisory, another key component to evaluate MSE was the volume of rock. The volume traced by the cutter through its path in the rock was apparent the same for circular cutting and linear cutting, because the same disc cutter advanced with the same horizontal velocity and vertical velocity. For the actual volume of rock been cut, the accumulative value along versus the horizontal distance was plotted in Figure 5.16, and it was shown that the actual volume of rock been cut was also almost identical.

Given the fact that the force components, volume of rock traced by the cutter, and volume of rock been cut were almost identical between circular cutting and linear cutting, it was concluded that the experience in linear cutting could be readily translated to circular cutting.

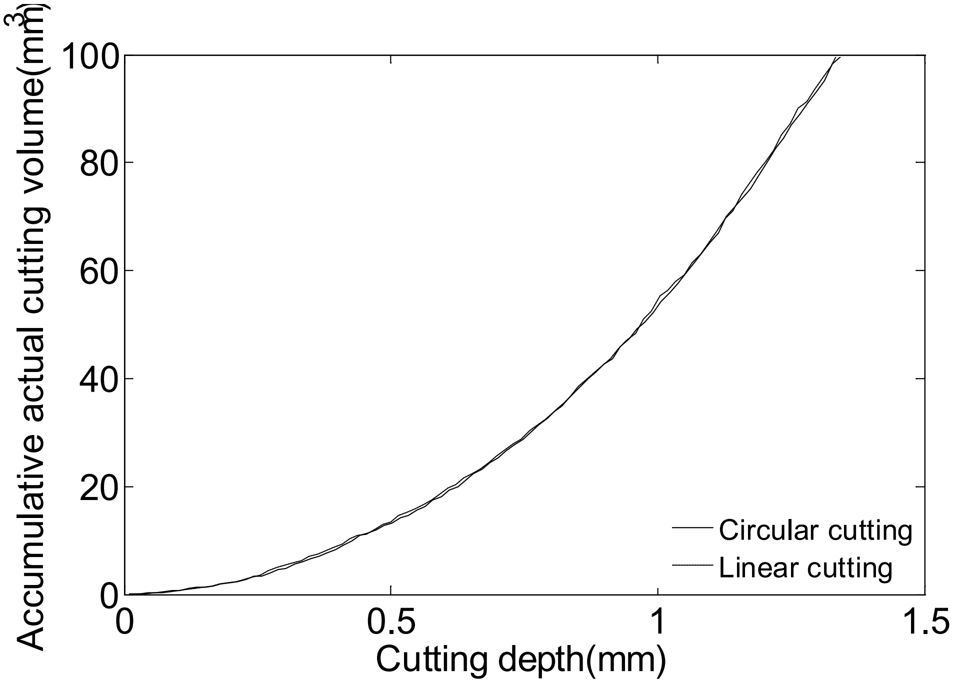

Figure 5.16 Comparion of eroded volume between linear cutting and circular cutting by a disc cutter

5.7 CONCLUSIONS

This study successfully simulated groove cutting using the FEM method. In spite of lacking data for a detailed calibration, our modeling results were consistent qualitatively with available laboratory tests results. For a rectangular cutter, we have shown that the specific energy decreased as the cutting width versus depth ratio w/d, decreased, because the effect of side cutting became insignificant. The computed trend of the specific energy of the groove cutting agreed well with the experiment.

After successfully modeling the linear cutting by a rectangular cutter, we moved on to the modeling of the circular cutting by a disc cutter, and the result showed that the cutting forces and specific energies for linear cutting and circular cutting were almost identical.

This study has obtained satisfactory results, by using a finite element mesh with element size in the order of 0.1 to 0.4 mm within the interested zone of the rock. Using such a small element size, however, could be problematic at times, causing anomalies such as distorted element deformation, or a decrease in the automatic time stepping to an unmanageable time step during a run. For future application, the issue of how to scale up the problem needs to be further investigated.

The element erosion algorithm in FEM often led to loose of contacts between the cutter and the rock elements. It then led to an underestimation of the cutting force, or the specific energy of the slab cutting. A proper tuning of FEM modeling would have to take this into account.

6.0 RELATIONSHIP BETWEEN MSE AND ROP BY CONSIDERING CUTTER WEAR

6.1 INTRODUCTION

Mechanical Specific Energy (MSE) and Rate of Penetration (ROP) are two key factors for evaluating the efficiency of a drilling process [9] and together they form a good base for strategizing a desirable drilling operation. MSE is defined as the energy required to removing a unit volume of rock [31]. This study looked into the relationship between MSE and ROP as obtained from cutting by a single Polycrystalline Diamond Compact (PDC) disc cutter as well as by a full drilling bit. In terms of a single PDC cutter, a MSE versus ROP relationship may be obtained in two ways. One approach is to use a suite of tests that adopts a different fixed depth of cutting for each of the tests, while advancing the cutter forward at a fixed speed. The other approach uses just a single test and advances the cutter both horizontally and vertically with their respective fixed rates. In this second approach, the rate of depth of cutting increases as the cutting progresses. This corresponds to an ever increasing ROP within a test. Thus a study on the relationship between MSE versus the depth of cut in such a setting constitutes a convenient way of understanding the relationship between MSE and ROP.

Even for the same ROP, or cutting depth, the MSE may be different for a blunt cutter due to the force below the cutter. Based on Detournay and Defourny's cutting model [15], the forces act on the cutting face and wear face independently for a blunt rectangular cutter, and the MSE can be expressed as:

$$\frac{MSE}{\varepsilon} = 1 + \mu \frac{F_n^f}{F_s^c} \tag{6.1}$$

where ε is the intrinsic specific energy for a sharp cutter, μ is the friction coefficient. F_n^f is the vertical force component on the wear face, F_s^c is the horizontal force component on the cutting face.

Both force components are assumed to be proportional to the area[15, 16]:

$$F_s^c = \varepsilon A_c, F_n^f = \sigma A_f \tag{6.2}$$

where A_c is the cutting area on the cutting face, A_f is the friction area on the wear face, σ is the contact stress on the wear face. The ratio of σ over ε is defined as $\kappa = \sigma / \varepsilon$, which is in the order of one to ten[109].

Extensive cutting experiments have shown that the intrinsic specific energy ε is approximately equal to the uniaxial compressive strength of rock σ_c [6, 7]. Thus, Eq (6.1) and Eq (6.2) leads to:

$$\frac{MSE}{\sigma_c} \approx 1 + \mu\kappa \frac{A_f}{A_c} \tag{6.3}$$

Specifically for a blunt rectangular cutter,

$$\frac{MSE}{\sigma_c} \approx 1 + \mu\kappa \frac{l_0}{d} \tag{6.4}$$

where l_0 is the initial wear length on the edge of cutter, d is the cutting depth.

Thus Detournay and Defourny's cutting model [15] presented an relationship between MSE and cutting depth, for slab cutting with both sharp and blunt rectangular cutters. The MSE associated with a blunt cutter is larger than that of a sharp cutter, as extra energy is consumed by friction in the bottom of blunt cutter. MSE also decreases with cutting depth provided that the wear length is constant, as friction is more significant at small depth. A blunt cutter may be a product of wear. The main wear mechanism includes: microchipping on cutter edge due to impact loading, abrasion caused by hard abrasive rock, thermal degradation by high temperature, among other factors[110, 111]

The concept of tip force due to defects or chamfer on the edge of cutter has been used by other researchers [6, 112, 113]. Challamel and Sellami[112] argued that an extra tip force might be introduced by microstructure effect and defects or chamfer on the tip of a cutter. Richard [6] found that the tip force could well explain the force intercept at zero depth for a nominal sharp rectangular cutter. Richard [113] has also observed the MSE decreases with cutting depth for a nominal sharp circular cutter.

The derived relationship between MSE and cutting depth based on Detournay and Defourny's cutting model [15] assumes a constant wear length along a rectangular cutter, without considering the evolution of wear during the cutting process. In a drilling operation wear would not remain unchanged. Thus, this study extended the relationship between MSE and depth to a circular cutter, and took into account the evolution of wear during cutting.

This study started by deriving a simple model for the relationship between MSE and cutting depth of a circular cutter, based on several assumptions. The model considered four different conditions: (1) perfect sharp cutter; (2) initially perfectly sharp cutter with a constant wear rate; (3) blunt cutter with a fixed wear; and (4) blunt cutter with a constant wear rate.

To test the model, Lagrangian Finite Element Method was first employed to model the circular cutting of a perfectly sharp circular cutter. In laboratory tests and in the field drilling, it is not always possible to obtain an accurate estimate of the volume of rock being removed. In contrast, in a finite element analysis the actual volume of rock being removed can be accurately estimated. An accurate estimate of removed rock volume turned out to be a significant issue as the results of this study would attest.

Secondly, the model was applied to some experiment data in literature[113]. The cutting tests were carried out with soft rock under ambient pressure condition. The actual volume of rock removed was estimated based on the measurement of micrometers after cutting.

Thirdly, the model was applied to cutting test conducted in the Ultra-deep Drilling Simulator (UDS) [10] of the Extreme Drilling Laboratory located at National Energy and Technology Laboratory (NETL), Department of Energy. The test was conducted under high pressure with high strength rock. The volume of rock removed was estimated using high resolution 3D surface profile obtained with confocal microscope.

Lastly, the model was employed to study MSE from the drilling operation by a full drilling bit.

6.2 A SIMPLE MODEL BETWEEN MSE AND DEPTH

Considered here is the case of a groove cutting with a circular cutter, in which the cutter advanced at a fixed horizontal velocity and a fixed but different vertical velocity. The rake angle considered is $\theta = 15^0$. A simple model between MSE and cutting depth is derived based on several assumptions as follows:

(1) The failure mode is ductile, as the cutting depth investigated is shallow.

(2)The 3D effect in groove cutting of a circular cutter is neglected for simplicity, as the *w/d* is typically large with small depth for a circular cutter. For a grooving cutting, its MSE is larger than that of a corresponding slab cutting, however, the difference is not significant when the ratio of *w/d* is large [6].

(3)The wear surface on the edge of the cutter is idealized to be horizontal, and it is in perfect contact with rock.

(4) The rate of wear is constant, in which the wear rate is defined as the increase of wear length within a unit contact time between the cutter and rock.

Assuming that the cutting surface of a circular cutter is in the coordinate system *x'y'z'*, which is rotated clockwisely with the rake angle of θ from the global coordinate system *xyz*. In other words, $y = y'\cos\theta$ on the cutting face. For a circular cutter with a radius *r*, the cutter edge on the cutting face can be expressed in polar coordinate as: $y' = r(1-\cos\phi)$. Figure 6.1 shows the definitions of the Cartesian coordinate systems *x'y'z'*, *xyz,* and the polar coordinate system as well as the geometrical terms used.

For a shallow cut, $\cos\phi \approx 1 - \frac{1}{2}\phi^2$, and the polar coordinates are related to the Cartesian coordinates by $\phi \approx \sqrt{2y/(r\cos\theta)}$. This gives the curve length along the cutter edge as:

$$L = 2r\phi \approx 2\sqrt{\frac{2ry}{\cos\theta}} \tag{6.5}$$

To consider the evolution of wear, a constant wear rate is defined here as: $K = dl/d\tau$, where l is the wear length on the edge of cutter, τ is the contact time between the cutter and the rock. For a cutter travels both horizontally and vertically, the contact time is a function of the depth of cut d, the vertical distance between the bottom of the cutter and any position below the rock surface y, and the vertical velocity of the cutter v_y. The contact time can be written as

$$\tau = \frac{d-y}{v_y}, 0 \le y \le d \tag{6.6}$$

As the wear length increases with contact time, thus at any location below the rock surface, the wear length can be expressed as:

$$l = l_0 + K\tau = l_0 + \frac{K}{v_y}(d-y), 0 \le y \le d \tag{6.7}$$

where l_0 is the initial wear length before cutting. The wear length is the largest at the bottom of the cutter after cutting, because of the longest contact time there.

When the depth of cut is *d*, the worn area along the cutter edge can be expressed as:

$$A_f = \int_c l dL = \int_0^d l \frac{dL}{dy} dy \approx 2\sqrt{\frac{2r}{\cos\theta}} l_0 f(d) \tag{6.8}$$

where $f(d) = d^{1/2} + d^{3/2}/\alpha, \alpha = 3v_y l_0/(2K), K \ne 0, l_0 \ne 0$. α is a parameter introduced for simplicity with a dimension of length. It is related to the wear rate K and thus can be determined from the boundary condition. Assume the final wear length in the bottom of cutter is l_f when the cut depth is d_f, then the wear rate can be expressed as: $K = (l_f - l_0)v_y/d_f$. For simplicity, the ratio of initial wear length over the final wear length in the bottom of cutter is defined as: $\beta = l_0 / l_f$, which lies between 0 and 1. α can be determined from the initial and final condition as: $\alpha = 3\beta d_f/[2(1-\beta)]$.

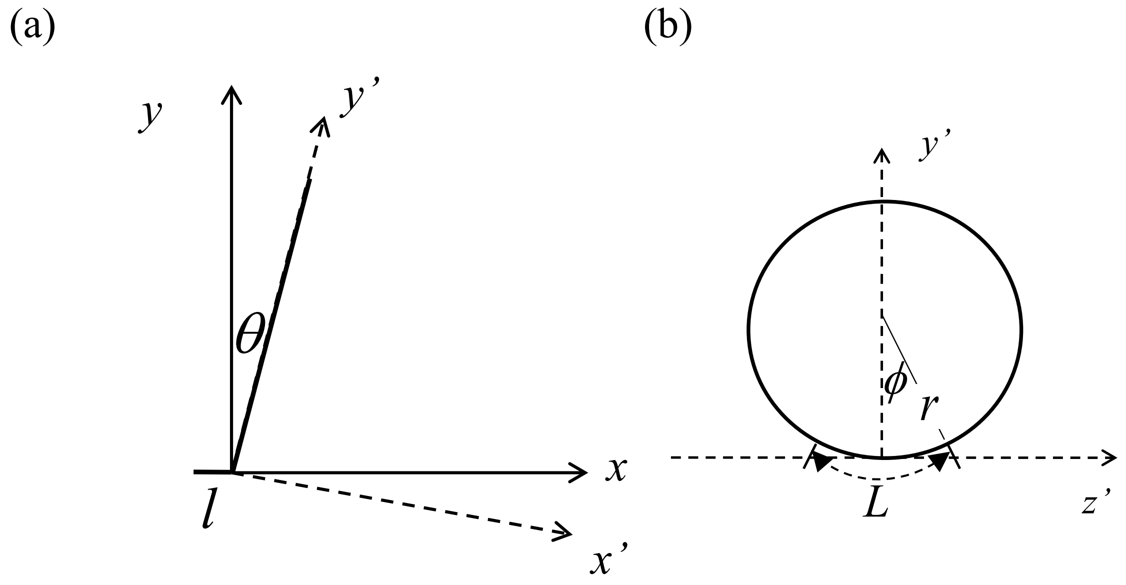

Figure 6.1 Coordinate transformation and geometrical terms.

The summation of two power functions can be further approximated with a simple power function: $f(d) = d^{1/2} + d^{3/2}/\alpha \approx g(d) = (\alpha+1)/\alpha\, d^{1/2+1/(\alpha+1)}$. Figure 6.2 shows the comparison of $f(d)$ and $g(d)$ for different α, with α=0.1, 1, 10mm, it shows that these two functions match well. Thus the friction area can be approximated by a simple power function of depth as:

$$A_f \approx 2\sqrt{\frac{2r}{\cos\theta}}\, l_0 \frac{\alpha+1}{\alpha} d^{\frac{1}{2}+\frac{1}{\alpha+1}} \tag{6.9}$$

The cutting area, on the other hand, can be expressed as:

$$A_c = r^2\left(\phi - \frac{1}{2}\sin 2\phi\right)\cos\theta \tag{6.10}$$

Based on the approximation of $\sin\phi \approx \phi - \phi^3/3!$, the cutting area corresponding to $y = d$ can also be approximated as a power function of depth as:

$$A_c \approx \frac{4}{3}\sqrt{\frac{2r}{\cos\theta}}\, d^{\frac{3}{2}} \tag{6.11}$$

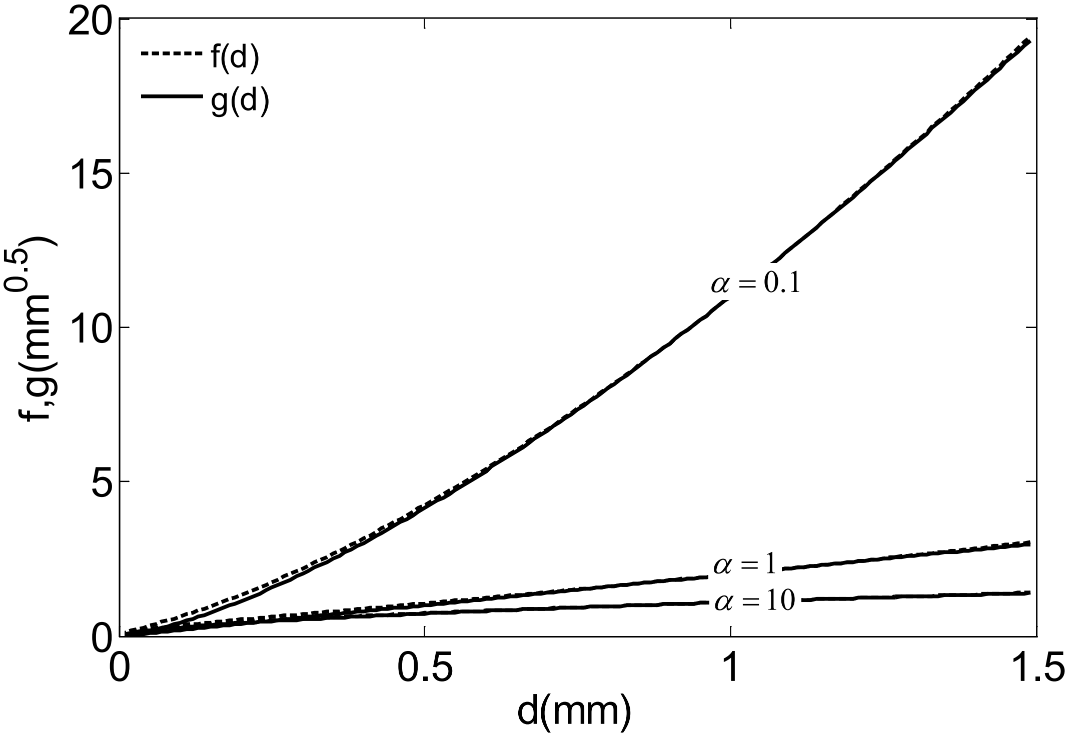

Figure 6.2 Approximation of the summation of two power functions with a simple power function

Thus, for an initially blunt circular cutter with a evolving of wear $(l_0 \neq 0, K \neq 0)$, a simple relationship between MSE and cutting depth can be expressed as:

$$\frac{MSE}{\sigma_c} \approx 1 + \frac{\beta_1}{d^{\beta_2}} \tag{6.12}$$

where $\beta_1 \approx 3\mu\kappa l_0/(2\beta_2), \beta_2 \approx \alpha/(\alpha+1), \alpha = 3\beta d_f/[2(1-\beta)], \beta = l_0/l_f$

It can readily be seen that the power β_2 lies in the range of (0,1), and a higher wear rate leads to smaller β_2 and larger β_1, resulting in larger MSE. The value of β_1 and β_2 in some special cases are as follows:

$\beta_1 = \beta_2 = 0$, for an perfectly sharp cutter $(l_0 = 0, K = 0)$;

$\beta_1 \approx \mu\kappa l_f/d_f, \beta_2 \approx 0$, for an initially sharp cutter with a constant rate of wear $(l_0 = 0, K \neq 0)$;

$\beta_1 \approx 3\mu\kappa l_0/2, \beta_2 \approx 1$, for an initially blunt cutter with a fixed wear $(l_0 \neq 0, K = 0)$.

6.3 FEM MODELING OF CIRCULAR CUTTING

For the modeling of a circular cutting by a disc PDC cutter, only 1/8 of rock sample was modeled as shown in the shaded area in Figure 6.3

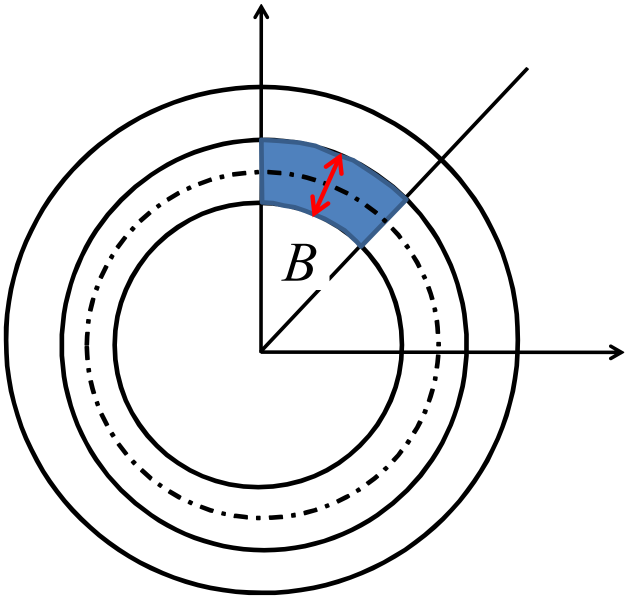

Figure 6.3 Sketch of rock sample used in the circular cutting model

As it has already been found that in this study that in order to ensure sufficient lateral confinement of a groove cutting, the width of the finite element rock sample should satisfy[114]:

$$B > w + 2w_a \tag{6.13}$$

where B is the sample width, w is the cutter-rock contact width, and w_a is affected distance from edge of a cutter, which is approximately six times of the average element size.

A sample of the FEM mesh used is depicted in Figure 6.4. The diameter and thickness of the PDC disc cutter considered was 13mm and 2mm, respectively. For the circular cutting studied, the width and average length of rock sample were 11mm and 23.4mm, respectively; while the sample height was 3mm, with the top 2.5mm a finely meshed zone formed with an average mesh size of 0.25mm. A total number of 645,140 tetrahedron elements was used in the sample depicted in Figure 6.4.

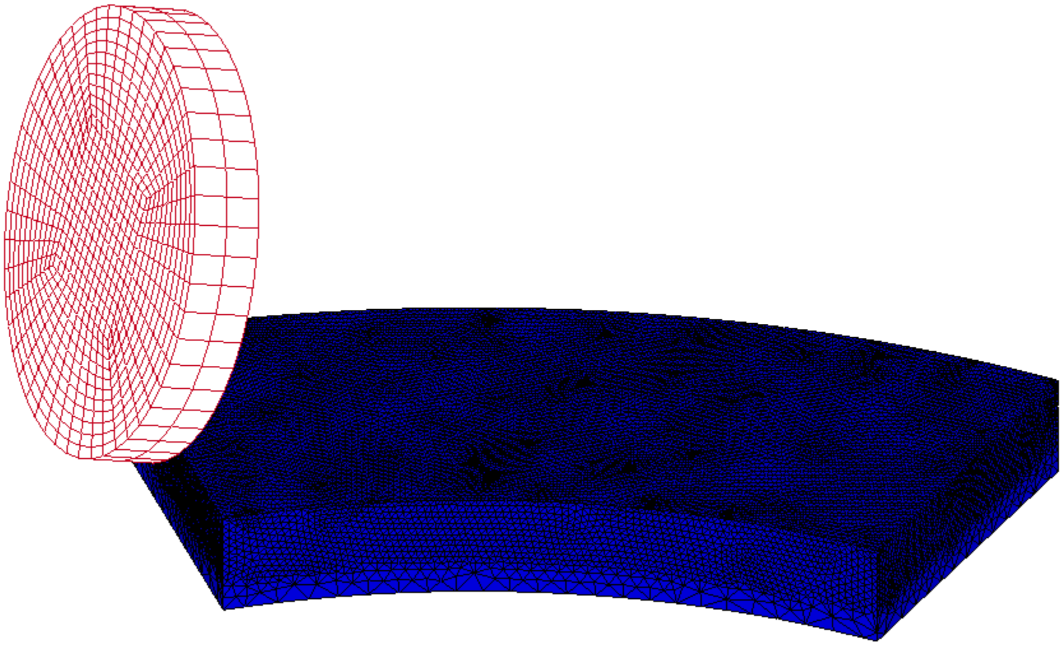

Figure 6.4 Mesh of cutter and rock for circular cutting

The rake angle of the circular cutter used was set at $\theta = 15^0$. The tangential velocity of the cutter was fixed at v_θ =4m/s, while the vertical velocity of cutter was fixed at v_v =0.255m/s, resulting in a linear increase of the cutting depth from zero on the left to 1.5mm on the right. The maximum cutting width was 8.4 mm, when the cutting depth reached 1.5mm, and the width of rock sample did maintain a sufficient margin as dictated by Eq. (6.13).

The present FEM cutting analysis was carried out on Vosges sandstone[64]. The uniaxial compressive strength was $\sigma_c = 39MPa$. As the adopted material model uses an erosion algorithm that deletes the rock elements after failure, thus the debris or plastic flow of crushed rock in front of cutter [41] would not be well modeled. To offset the influence of erosion algorithm on the cutting force, special efforts were conducted by tunning the dynamic strength of rock, to offer reliable cutting force observed in laboratory cutting test.

Figure 6.5 gives the configuration of a cutting in progress as well as the state of damages incurred on the sample behind the cutter as it passed. Figure 6.6 shows the histories of three force components, the force normal to the cutter, f_θ, the force tangential to the cutter, and the vertical force, f_v. The cutting forces obtained were larger than the thrust forces, and the side forces were around zero. These trends agreed qualitatively with the laboratory test of circular cutting in ambient pressure environment of sharp cutters[8].

MSE computation requires an estimate of the volume of rock being removed. Two different volume measures can be distinguished: the project removed volume and the actual removed volume. The projected removed volume is the volume that is swept by a cutter through its path over the sample; whereas the actual removed volume is literally the actual volume of rocks that is being removed.

Given the histories of force components and projected cutting area during the cutting process, the MSE using the projected volume may be calculated as:

$$MSE_p = \frac{dW}{dV_p} = \frac{f_\theta v_\theta + f_v v_v + f_r v_r}{A_p v_\theta} \approx \frac{f_\theta}{A_p} \tag{6.14}$$

Where W is the work, V_p is the projected removed volume, A_p is the projected area that the cutter traced through its path in the rock.

If the actual removed volume of rock was used, the MSE_a could be calculated as:

$$MSE_a \approx \frac{f_\theta}{A_a} \tag{6.15}$$

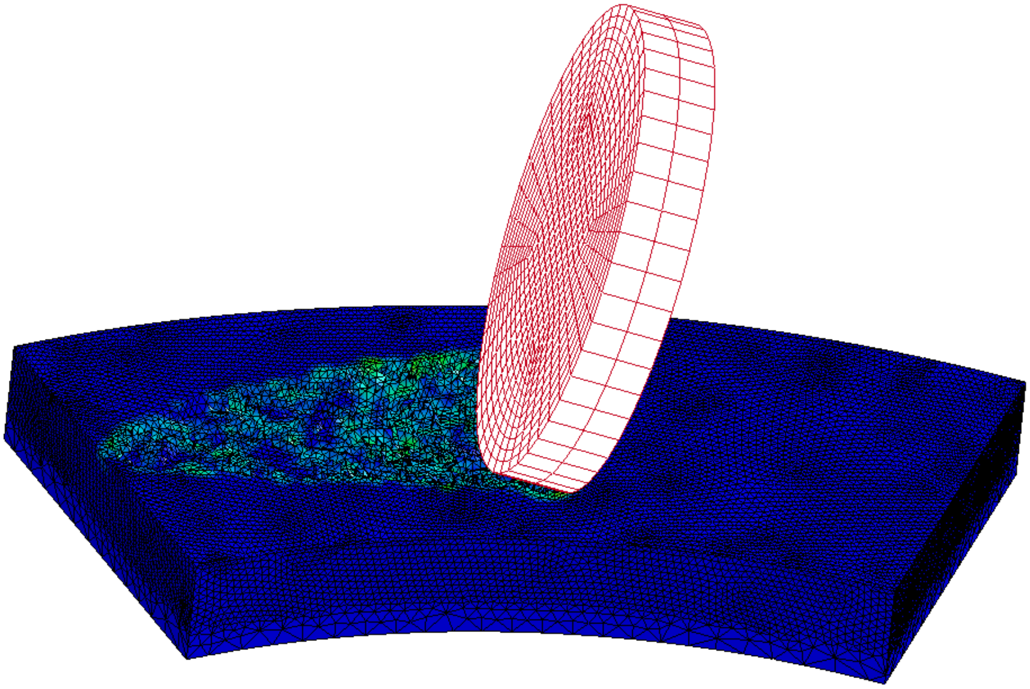

Figure 6.5 A snapshot of showing the cutting in progress.

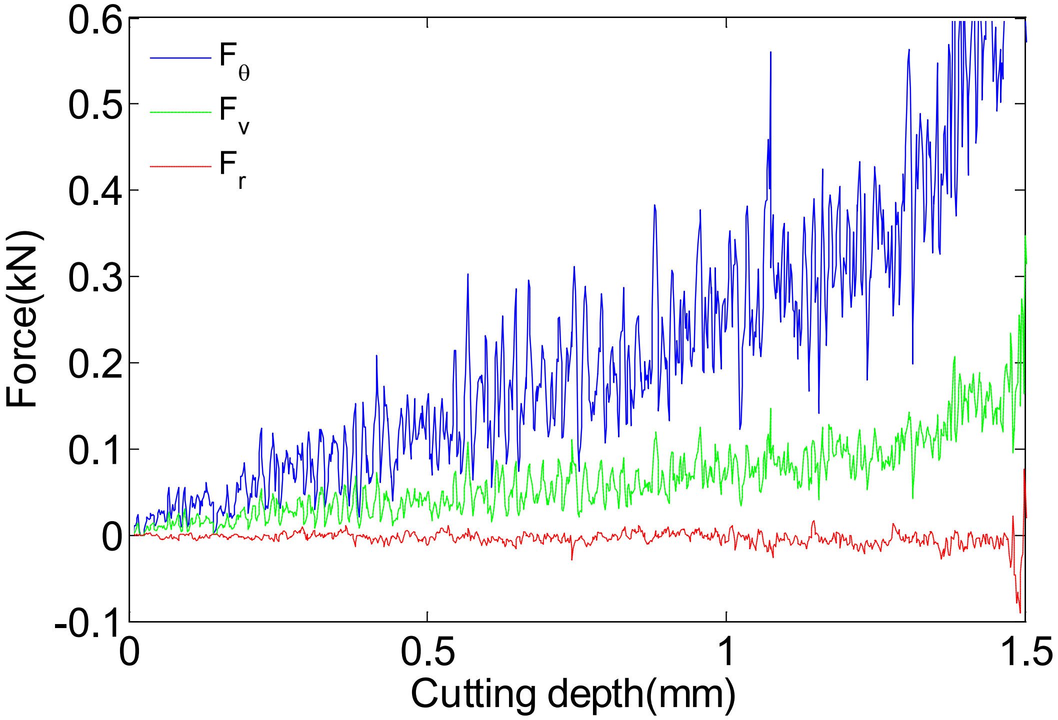

Figure 6.6 Histories of forces obtained in FEM

The actual cut area A_a was related to the actual volume cut, V_a, as

$$A_a = \frac{dV_a}{v_\theta dt} \tag{6.16}$$

In a FEM run both areas can be readily found. The projected area and actual cut area are plotted in Figure 6.7.

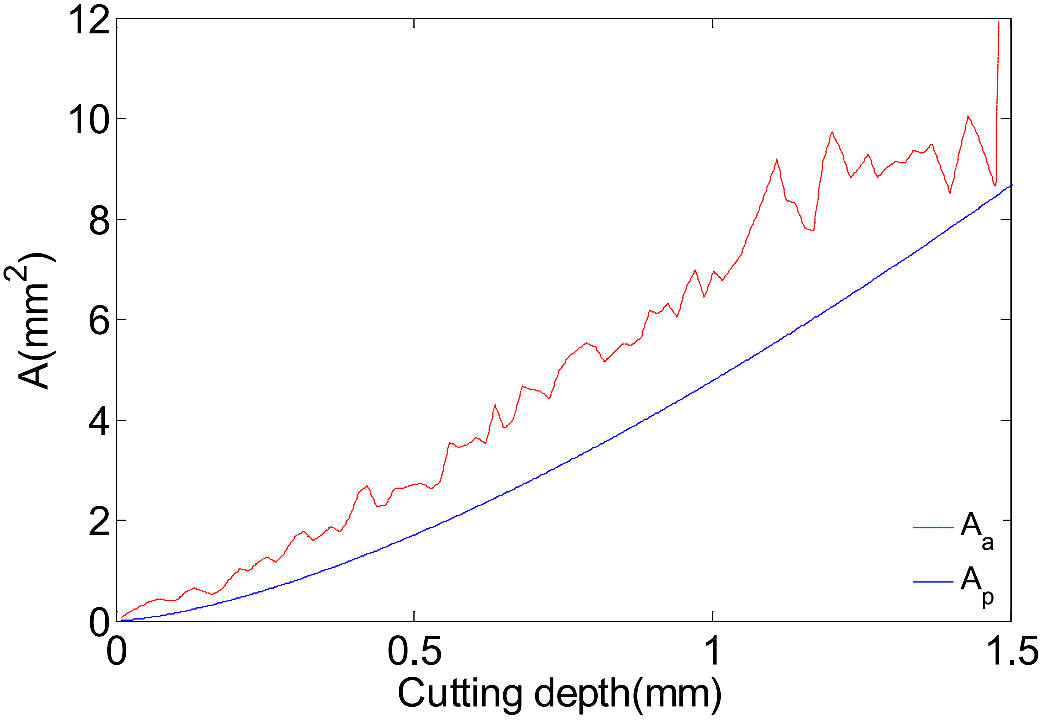

Figure 6.7 History of actual cut area and projected area in FEM

The actual removed or cut area, fluctuated as expected, whereas the smaller projected area was smooth. The MSE$_p$ or MSE$_a$ obtained are presented in Figure 6.8, in which a moving average has been applied as a filter. Figure 6.8 shows that the MSE$_p$ computed decreased with the cutting depth and then leveled, while the actual MSE$_a$ was more or less constant. To eliminate the possible effect of boundary, the depth smaller than 0.3mm and larger than 1.3mm were taken out, thus only the depth from 0.3mm to 1.3mm were plotted.

Because the FEM analysis modeled a sharp cutter, the MSE_a obtained should be a constant, independent of the depth of cut, as the analysis results affirmed. The estimate of the MSE from using the projected area would best be carried out at the maximum depth where the projected area and actual cut area has the smallest difference.

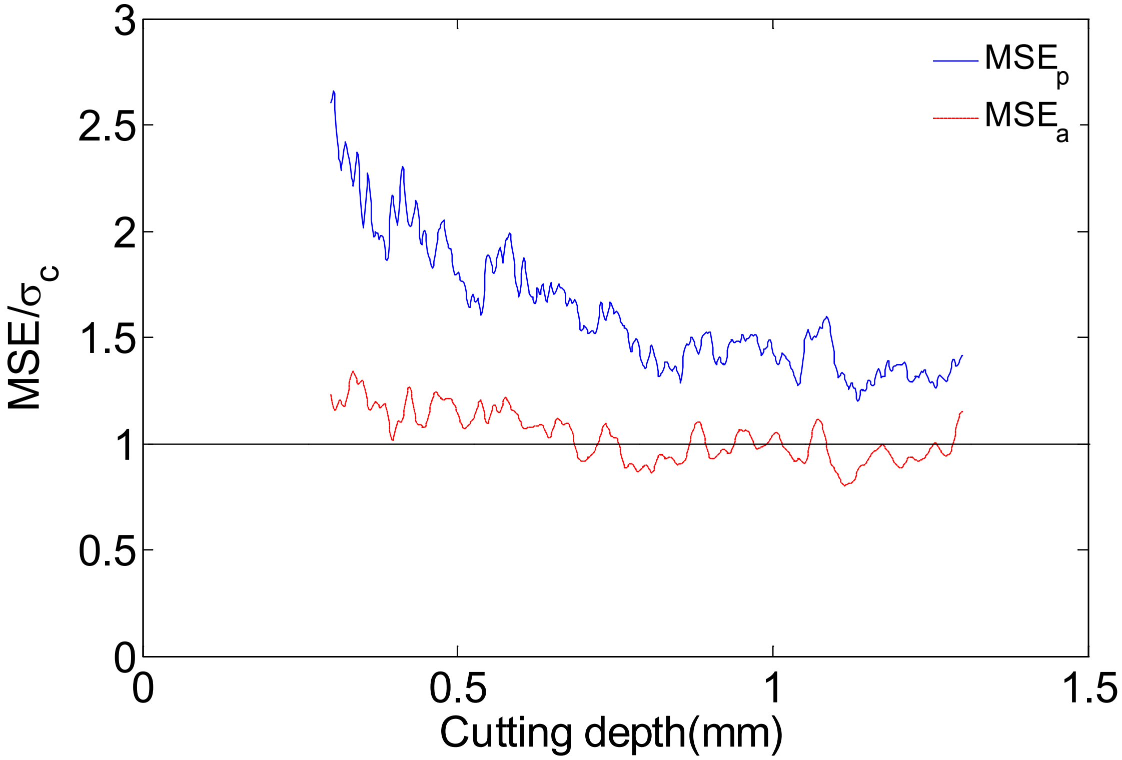

Figure 6.8 Evolution of MSE_p and MSE_a over cutting depth in FEM

6.4 EXPERIMENT OF CIRCULAR CUTTING UNDER AMBIENT PRESSURE CONDITION

Richard et al. [113] conducted extensive experiments on the groove cutting tests under ambient pressure condition. The tests involved various cutters with various geometries, including circular, triangular and rectangular cutter with various soft sedimentary rocks. The cutting depths were small, typically less than 1mm, and the rock was deemed to have failed in ductile mode. The cutting depth was kept constant during each test, but the depth varied from test to test. For each test, the cutting depth was measured with a micrometer at several points along the groove after cutting, and the average depth was used as the actual cutting depth[113].

Two sets of their circular cutting data obtained using two different cutter radii were compared to the present model. The radii of the cutter were 6.5mm and 9.5mm, respectively, with an average initial wear lengths.l_0 in the range of 0.05 to 0.08mm. The back rake angles were fixed at $\theta = 15^0$. The particular rock tested was soft Lens limestone, with $\sigma_c = 30MPa$. The data with cutting depth smaller than 1mm were used to fit Eq (6.12), and we found a reasonable good match for these two sets of data, as shown in Figure 6.9. Specifically, for the test with the cutter radius of $r = 6.5mm$, $\beta_1 = 0.18, \beta_2 = 0.96$ and $R^2 = 0.93$; while for the test with the cutter radius $r = 9.5mm$, $\beta_1 = 0.10, \beta_2 = 1.04$ and $R^2 = 0.81$.

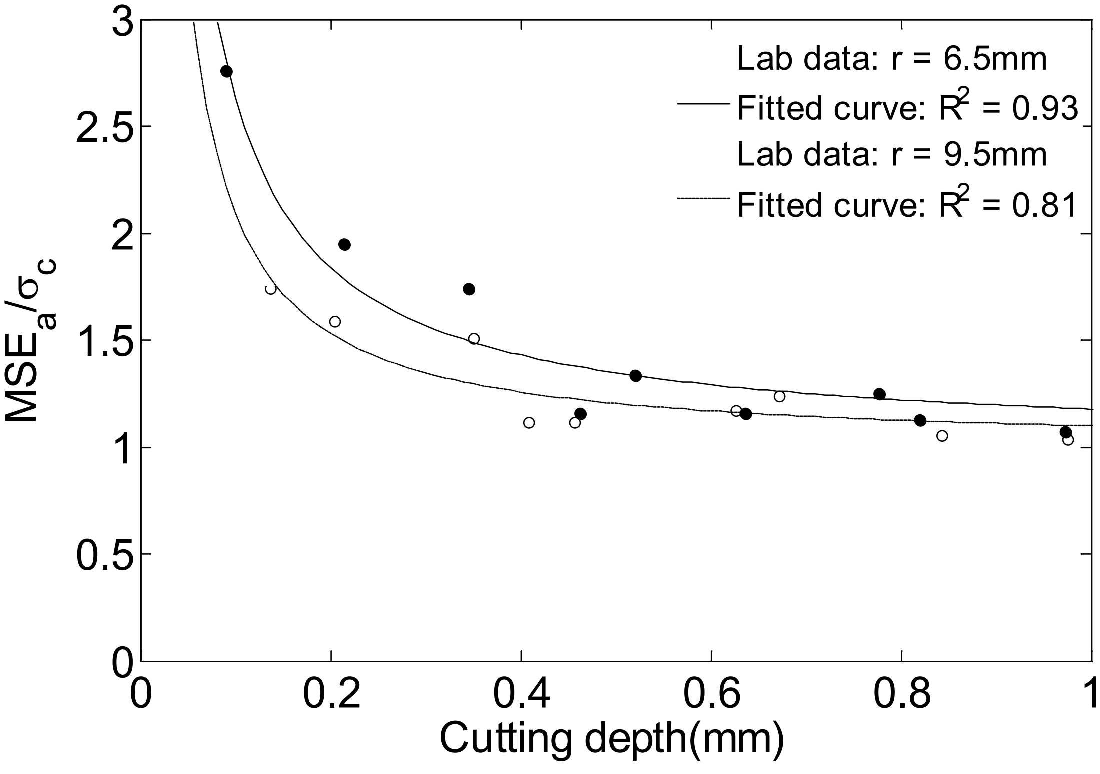

Figure 6.9 Evolution of MSE with cutting depth under ambient pressure condition

Due to the uncertainty about the contact stress on the wear face, the comparison between the fitted result and the model was focused on the parameter β_2. For these two sets of data, it shows $\beta_2 \approx 1$, suggesting that the wear length of the initially blunt cutter was approximately constant when cutting soft rock under ambient pressure condition.

6.5 EXPERIMENT OF CIRCULAR CUTTING UNDER HIGH PRESSURE

To understand the complex interaction among the drilling bit, rock, and drilling fluid, NETL invested in the construction of an Ultra-deep Drilling Simulator (UDS) [10] as shown in Figure 6.10(a). The UDS is capable of simulating the cutting action of a single PDC cutter under pressure as high as 205MPa. Figure 6.10(b) gives a layout on the force measurements taken in UDS.

Here we studied one set of test results obtained from UDS [10]. The PDC disc cutter had the diameter and thickness of 16mm and 1.8mm, respectively. It also had a small chamfer of 0.3mm at 45 degrees. The rake angle applied was set at 15 degrees, and the initial wear flat length l_0 was approximately 0.4 mm along the edge of cutter. The rock tested was Carthage marble, and the sample had a diameter of 0.2m and a thickness of 0.2m. The surface of the rock sample was tilted in a fashion so that the cutting depth would increase from 0 to 1.5mm as the cutter was rotated without vertical translation. A clear mineral oil was used to simulate the drilling fluid, and a pressure of 103 MPa was applied through the hydraulic system. Figure 6.11 presents a photo of the rock sample of Carthage marble taken after cutting was completed.

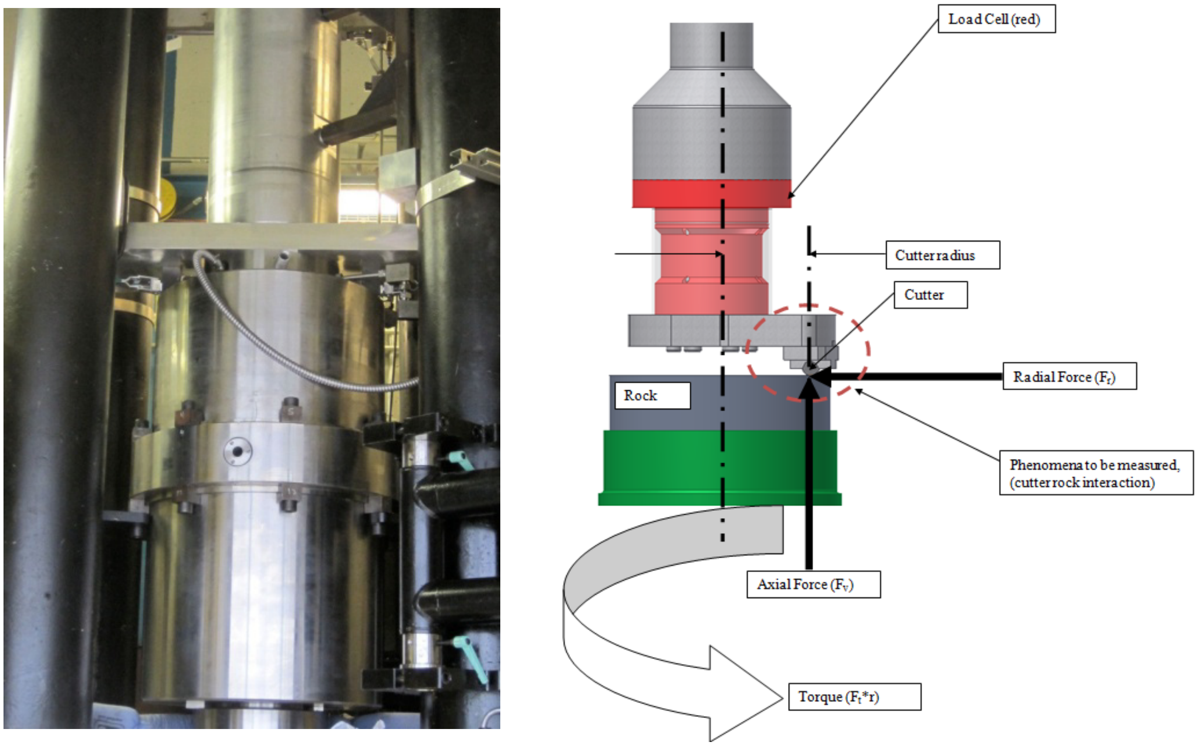

Figure 6.10 Laboratory of rock cutting under high pressure in (a)one view of the NETL UDS system (b)The UDS force measurement layout[10]

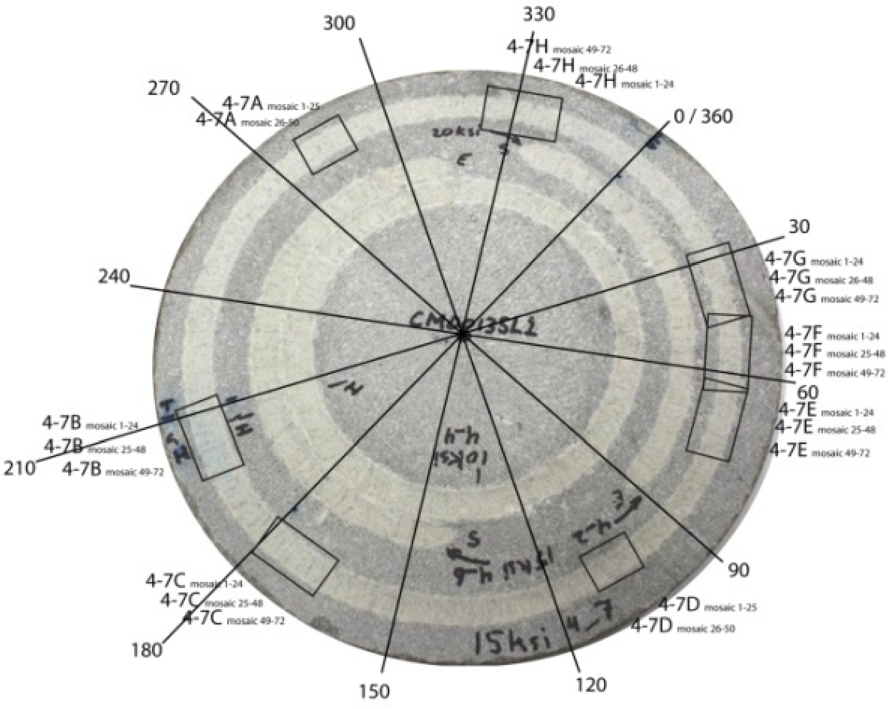

Figure 6.11 The rock sample of Carthage marble[115]

Three force components were recorded during the cutting process, and two primary force components obtained are depicted in Figure 6.12, as the side force was almost zero.

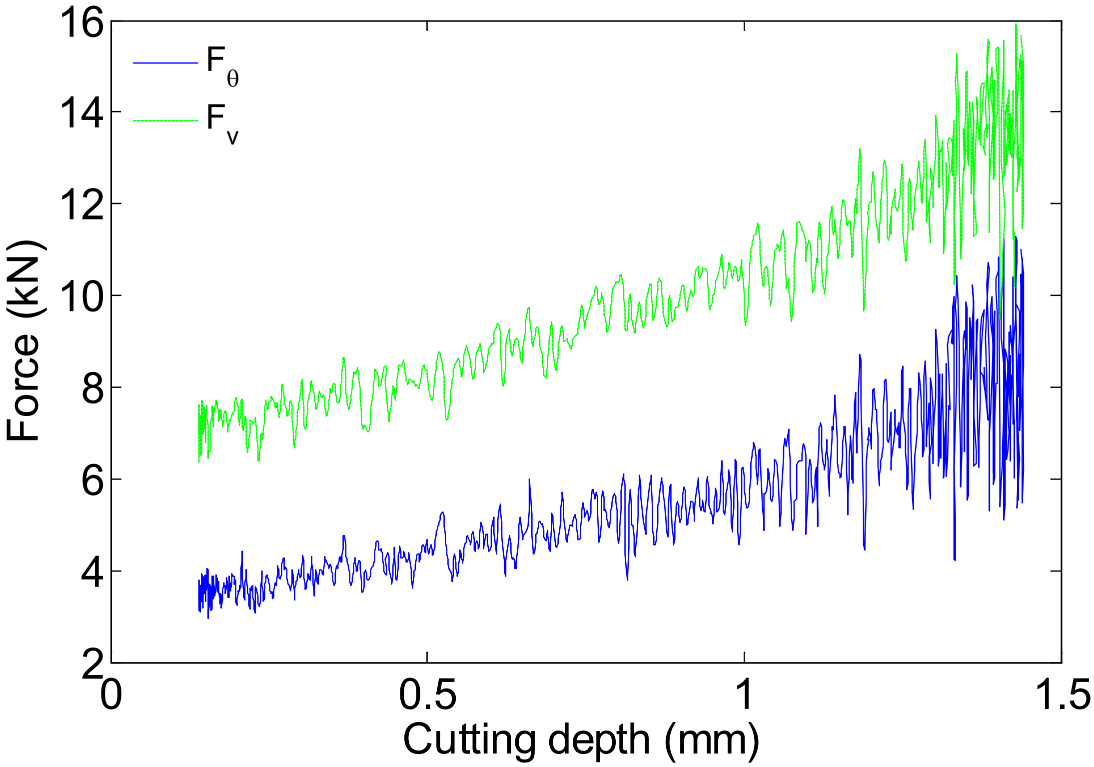

Figure 6.12 History of tangential force and vertical force in UDS

The projected area was calculated based on the geometry and the experiment setup, and the actual cut area was obtained by measurement through high resolution three-dimensional images taken by a confocal laser scanning microscope [115]. Confocal images were taken on several rectangular areas on the surface of the rock sample as shown in Figure 6.11, and one is presented in Figure 6.13.

Based on the projected area and actual cut area, the corresponding MSE_p and MSE_a were obtained and plotted in Figure 6.14. It can be observed, just as from the FEM results, that MSE decreased with cutting depth and then leveled. Meanwhile, MSE_a also varied with depth, albeit with a smaller change. From the fact that the vertical forces or, weights on bit, were much larger than the cutting forces, it follows that the cutting was similar to that from a blunt cutter, and friction between the cuter and the rock surface was significant even though the cutter was initially sharp with small chamfer.

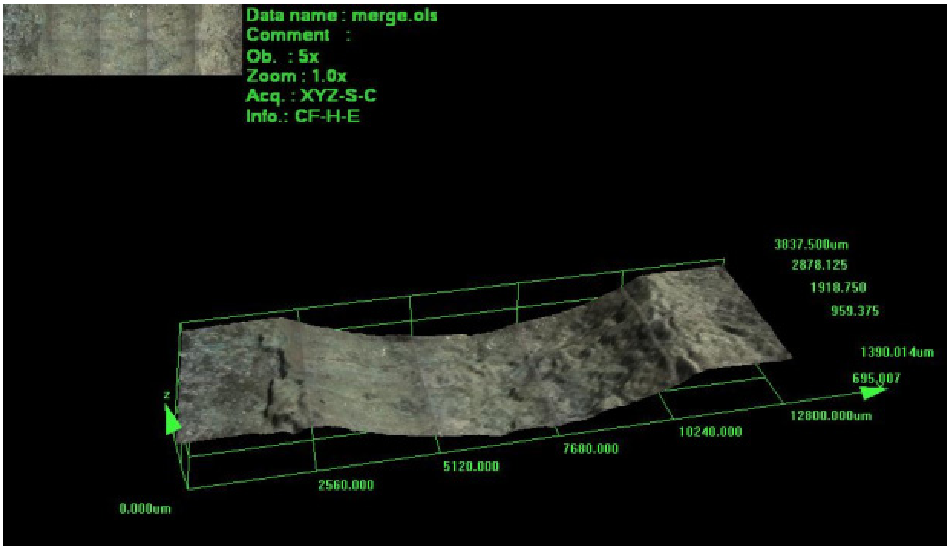

Figure 6.13 Confocal image of a typical section after cutting in UDS[115].

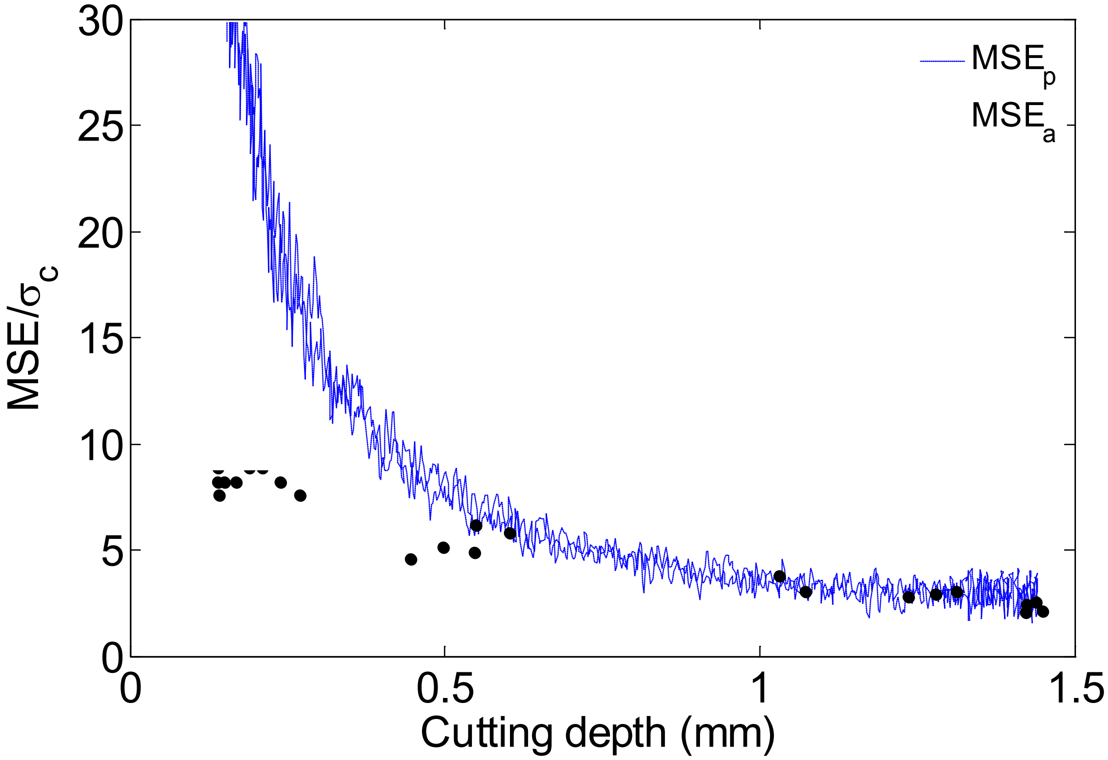

Figure 6.14 Evolution of MSE with cutting depth in UDS

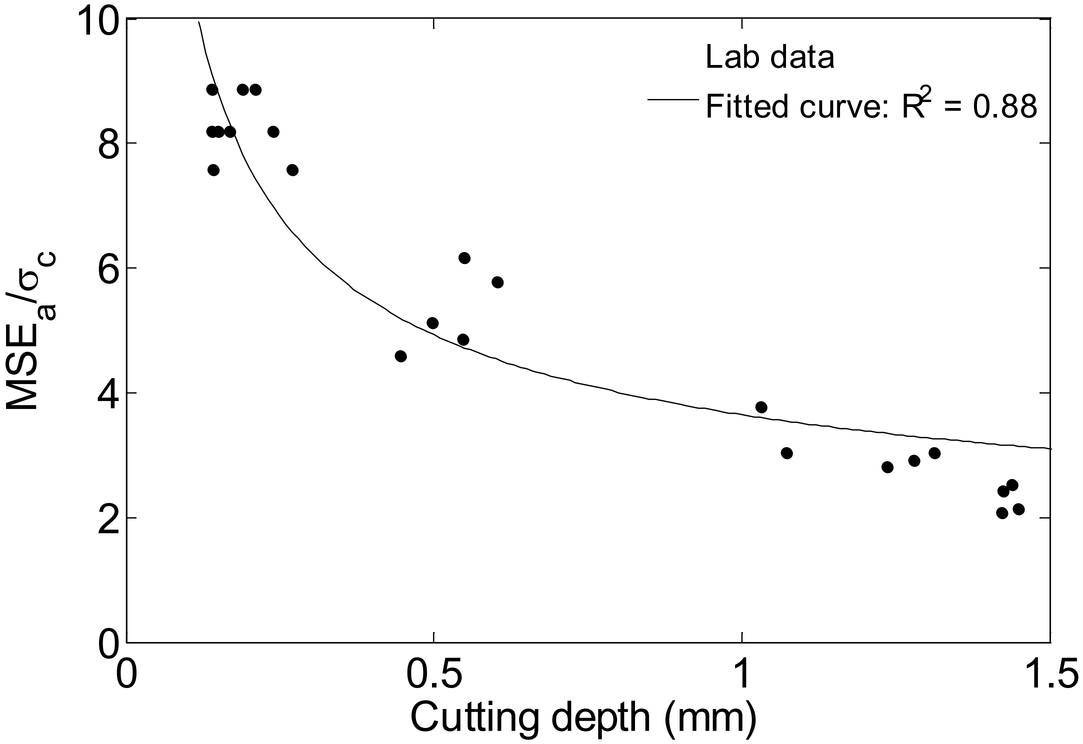

Figure 6.15 An interpretation of the MSE_a with depth in UDS

When fitting the UDS MSE_a data to Eq. (6.12), a good match was found with $\beta_1 = 2.56, \beta_2 = 0.57, R^2 = 0.88$, as shown in Figure 6.15. Here the MSE was normalized with the confined compressive strength of Carthage marble $\sigma_c \approx 317MPa$ under the confining pressure of 103MPa[9].

The fitting result $\beta_2 \approx 0.57$ suggests substantial wear during cutting under high pressure condition. The wear length in the bottom of cutter was determined to be approximate 3 times of the original value after cutting with $d_f = 1.5mm$, as illustrated by:

$$\frac{l_f}{l_0} \approx \frac{3}{2} d_f \left(\frac{1}{\beta_2} - 1 \right) + 1 \approx 2.7 \tag{6.17}$$

The shape of cutter before and after cutting are shown in Figure 6.16[10]. Even though the final wear length after cutting couldn't be accurately determined, Figure 6.16 clearly show the bottom of cutter severely wore after cutting.

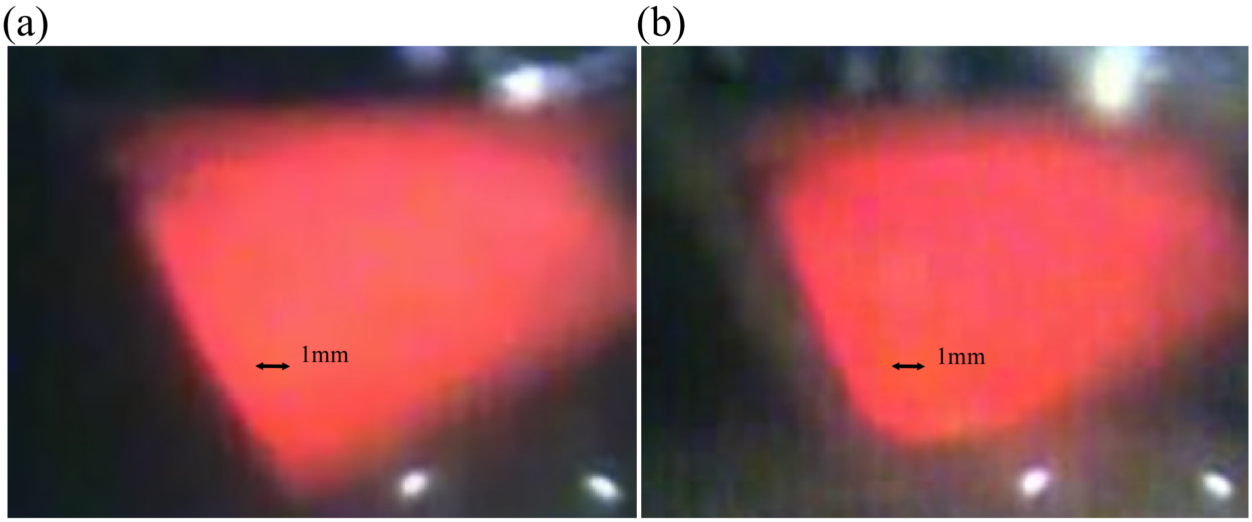

Figure 6.16 The shape of the cutter in UDS (a) before cutting (b) after cutting [10]

By comparing the results of cutting low strength rock under ambient pressure and that of cutting high strength rock under high pressure condition, it shows that the MSE is much larger in the latter case. As the proposed model is associated with $\sigma_c, \beta_1, \beta_2$, thus it suggested that the extra energy consumed is mainly due to the following factors among others:

(1) The strength of rock increases under high pressure condition, and gave a larger σ_c;

(2) Cutting high strength rock under high pressure leads to severe wear in the cutter, that resulted in a smaller β_2;

(3) The friction coefficient is larger in high pressure condition[116, 117], and the contact stress is also expected to be larger. As β_1 is approximately proportional to the friction coefficient, the normalized contact stress, and the inverse of β_2, thus high pressure will results in larger β_1.

6.6 FULL BIT DRILLING TEST

In a laboratory drilling test, the actual cut volume, even though unknown, was not expected to vary significantly from the projected volume. This is mainly because the extra cutting volume beyond the edge of bit is small compared to the volume that the bit traced. Extensive laboratory drilling tests have been carried out by TerraTek[9] under contract from DOE, to improve the drilling performance under high pressure high temperature condition. The tests involved different rocks, drilling bits and drilling fluids. A set of data from the drilling test was studied. The tested rock is Crab Orchard Sandstone, which had a confined compressive strength of $\sigma_c \approx 593 MPa$ under the confining pressure of 76MPa[9]. The MSE obtained is presented in Figure 6.17.

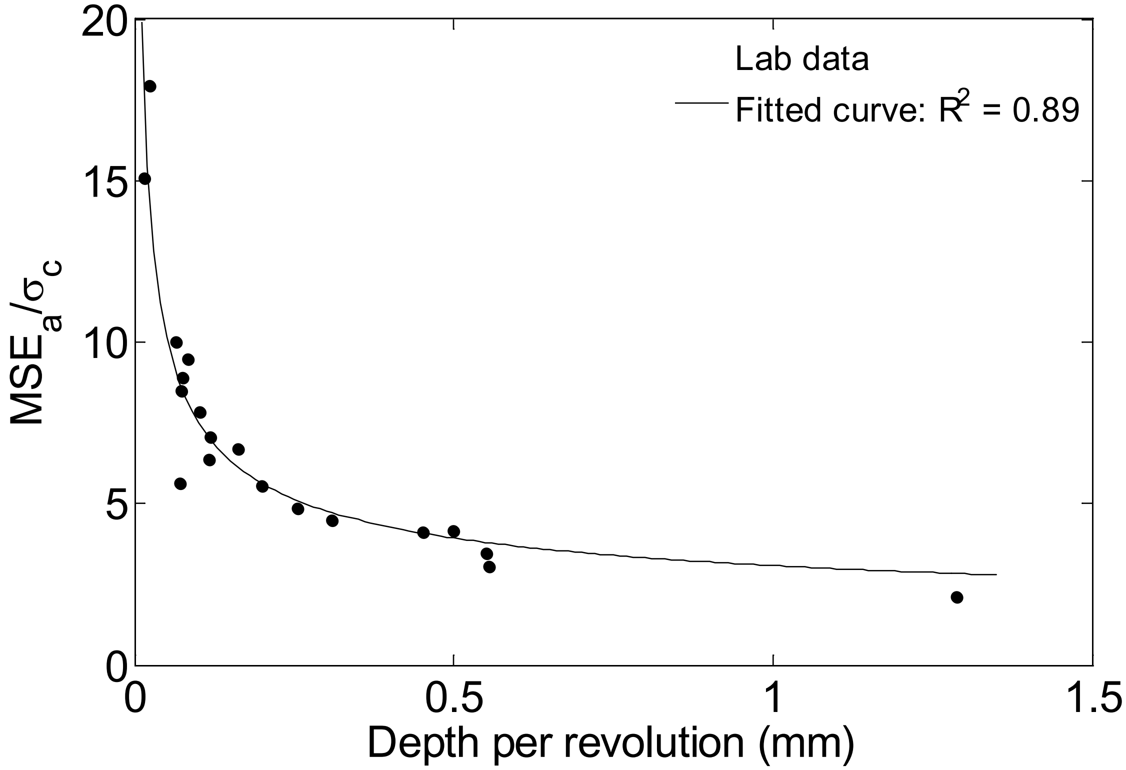

Figure 6.17 Evolution of MSE with depth per revolution with full drilling bit

The projected volume of the rock removed was calculated by multiplying the cross area of the drilling bit and the average depth per revolution. It was observed that MSE of the full drilling bit has a similar trend to that of a single cutter, in the sense that MSE decreased with depth and then almost leveled. Again, Eq. (6.12) provided a good match with the data with $\beta_1 = 2.08, \beta_2 = 0.49, R^2 = 0.89$. Even though the mechanics of the drilling process by a full drilling bit is much more complex than that of a single cutter, the relationship between MSE and cutting depth was found to follow a similar equation.

6.7 CONCLUSIONS

A simple model between the MSE and cutting depth for a circular cutter was proposed, by considering the wear evolution of the wear surface. The derivation was an extension to Detournay and Defourny's cutting model for a rectangular cutter with fixed wear length. Numerical simulation and laboratory tests have been successfully carried out to study the effect of cutting depth on MSE, and the results matched well with the proposed model.

In the FEM analysis, when a sharp cutter is used, the MSE would be constant if the actual cut volume is used in its calculation, and the MSE obtained is approximately equal to the uniaxial compressive strength.

In the laboratory test of cutting soft rock under ambient pressure environment, the rate of wear increase was negligible, and the initial wear length is thus approximately constant. Even though the small chamfer had large influence on MSE at small depths, its impact diminished at larger cutting depth, since the MSE leveled off at the value approximately equaled to the uniaxial compressive strength.

In the laboratory test of cutting hard rock under high pressure environments, the rate of wear increase is not negligible. The evolution of cutter wear makes the normalized MSE much larger compared with those from cutting soft rock under ambient pressure condition.

This simple model proposed also applies to the drilling by a full bit, and may serve as an approximation when a theoretical relationship between MSE and ROP is not available.

7.0 THE MECHANICS OF ROCK DRILLING

7.1 INTRODUCTION

A full drilling bit consists of multiple cutters have been used for drilling for more than a century[109]. The cutters were originally made of steel, and the invention of PDC cutter in 1970s significantly improves the drilling efficiency. The two most important factors in characterizing the drilling efficiency is through the use of MSE and ROP as discussed. To increase the drilling efficiency and decrease the drilling cost are the main objectives for a bit design to strive to achieve. A bit design covers a spectrum of issues from the selection of the bit body material, cutter placement pattern and density, bit profile, back rake, side rake and hydraulic horsepower, among other factors [12]. The interaction between drilling bit and rock is a complex process, and the main methodologies to study the interaction include analytical models[13, 16], laboratory and field tests [1, 9, 12], and numerical modeling.

Due to complex mechanism of bit rock interaction under High Temperature High Pressure (HTHP) condition the analytical models were typically derived for ambient pressure condition[13, 16]. Even so, further simplifications were necessary, because of the complicated geometry and discrete properties of drilling bit, the complicated contact interaction between cutters and rock.

Laboratory and field tests are the most widely used methods to evaluate the efficiency of drilling under various conditions[1, 9, 12], because they could render reliable results in the actual drilling process, with the inclusion of HTHP, complicated bit geometry, and other factors. A major drawback of physical tests is that they are expensive.

Compared with analytical models and physical tests, numerical modeling has many advantages: it is able to accommodate complicated geometry of the bit, to extensively study the key parameters influencing the drilling efficiency, all at a relatively low cost. To make the numerical modeling reliable, the numerical procedure and parameters employed should be carefully calibrated with results from physical tests.

In this Chapter, some analytical models and important results in physical tests were first reviewed[9, 13, 16], and a prototype numerical drilling bit was initiated. The objectives were to demonstrate that a detailed mechanical modeling of a drilling bit was feasible.

7.2 ANALYTICAL MODELS

Based on the 2D cutting model [15], Detournay et al. developed a 3D model for a PDC drilling bit[16]. Instead of considering explicitly the cutter shape and the cutter distribution on a bit, this 3D model introduced a bit constant to represent the geometry impact of the bit. A full set of equations were established by relating Weight on Bit (WOB), ROP, Torque on Bit (TOB), and angular velocity, Ω, of the bit rotation. The dynamic parameters WOB and TOB are conjugate to the kinematic parameters ROP and Ω [16] . However, the two kinematic parameters can be combined by redefining ROP as depth of penetration per revolution. By so doing, only three independent parameters need to be considered. The dynamic parameters WOB and TOB could then be expressed as functions of the kinematic parameters ROP [16].

$$WOB = WOB(ROP), TOB = TOB(ROP) \tag{7.1}$$

Figure 7.1 shows a typical PDC drilling bit, the idealized bit in a 3D model, as well as corresponding cutter in 2D [15, 16, 118]. The frictional effect is represented in the 2D by a flat length, *l*. In this simplified representation, a rotation of the 2D cutting model [15]. becomes the basis for the rotation of a 3D model [16]. This is carried out by scaling WOB and TOB with the radius of the drilling bit, *a*, and the two sets of parameters were related as[16]:

To make the interface law of 2D model [15] readily be used in the 3D model, the WOB and TOB were scaled based on the radius of the drilling bit, *a*, and introduces an equivalent 2D model subjected to a vertical force denoted as *wob*, and a horizontal force denoted as *tob*. The equivalence of a 2D and 3D models are established as follows, [16]:

$$wob = \frac{WOB}{a}, tob = \frac{2TOB}{a^2}, ROP = d \tag{7.2}$$

On the other hand, the MSE incurred by a drilling bit includes two parts, coming from TOB and WOB respectively, and it may be expressed as [31],

$$MSE = \frac{TOB * 2\pi + WOB * ROP}{\pi a^2 * ROP} \tag{7.3}$$

As the angular displacement associated with TOB is typically much larger than the vertical displacement associated with WOB, the work associated with WOB is negligible, and the MSE for a drilling bit could be simplified as:

$$MSE \approx \frac{2TOB}{a^2 * ROP} = \frac{tob}{d} \tag{7.4}$$

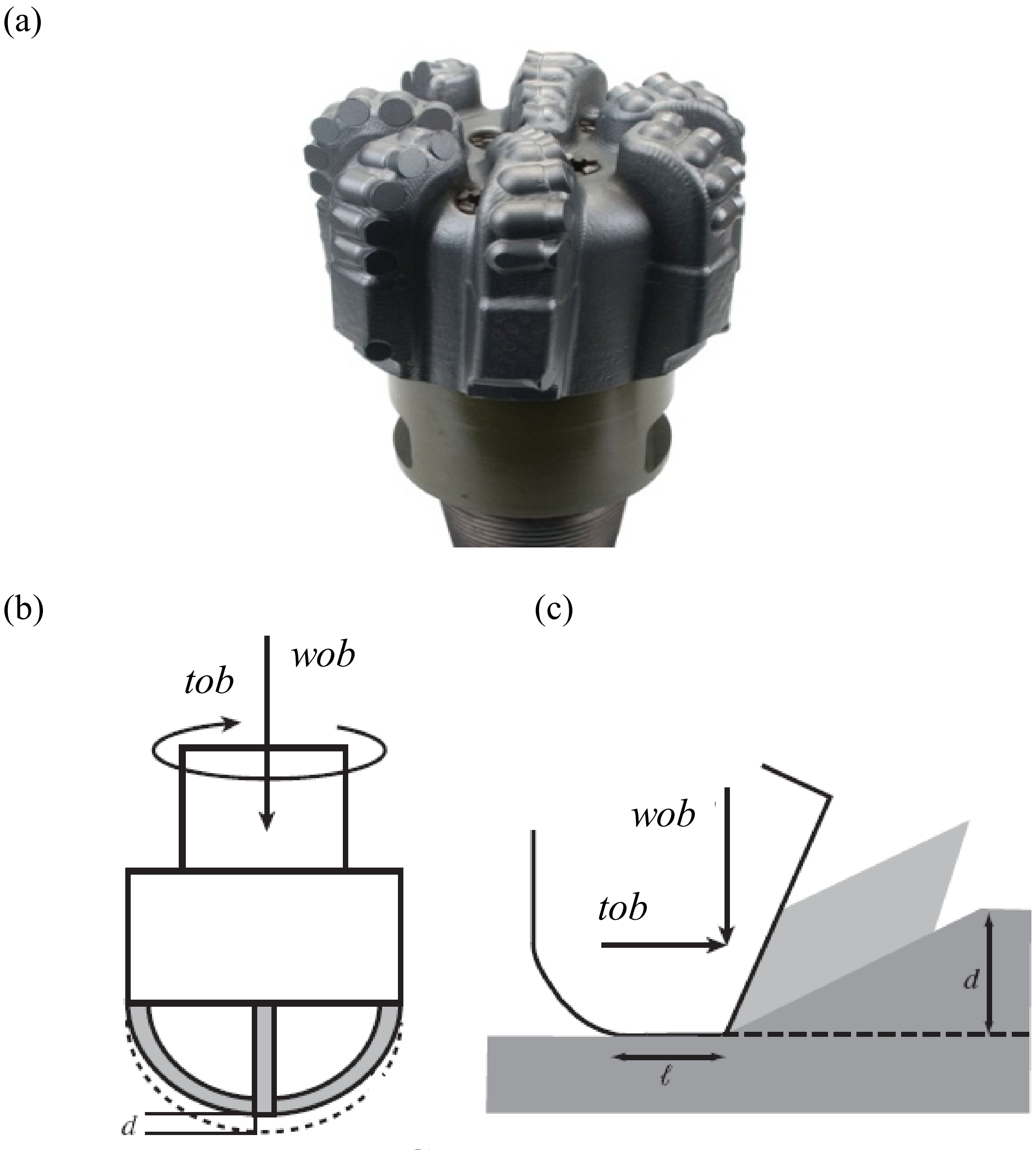

Figure 7.1 3D model for a PDC bit (a) a real PDC drilling bit (b) a simplified PDC bit (c) the equivalent 2D model[15, 16, 118]

As the TOB is a function of ROP, the MSE could also be expressed as function ROP. The 3D model of Detournay et al. considered the existence of three drilling phases as the drilling progressed in depth. They reasoned that the contact conditions between the drilling bit and rock changed as the depth of drilling increased, and as a result different relationships between TOB and ROP emerged[16]. In phase I, the wear friction, represented by the flat length increases linearly with the depth, then it becomes constant in the phase II, and it is more complicated in phase III for instance the poor cleaning may increase the flat length, while vibration may reduce it[16]. The general trend of *wob* and *tob* in the first two phases, which is of interests to the study, were similar and shown in Figure 7.2(a) [16]. A corresponding relationship between MSE and depth has been derived based on Eq (7.4) and a general trend is depicted in Figure 7.2(b).

It is clear that MSE is decreases with depth in phase II, which covers the typical range of depth in the actual drilling process. This trend agrees with the laboratory drilling test[9]. However, in phase I when the drilling bit is not in full contact with the rock, the 3D model suggested the MSE be constant. This, however, deviates with the laboratory drilling results, likely due to the unsatisfactory the assumption that the contact length increases linearly with depth in phase I.

(a)

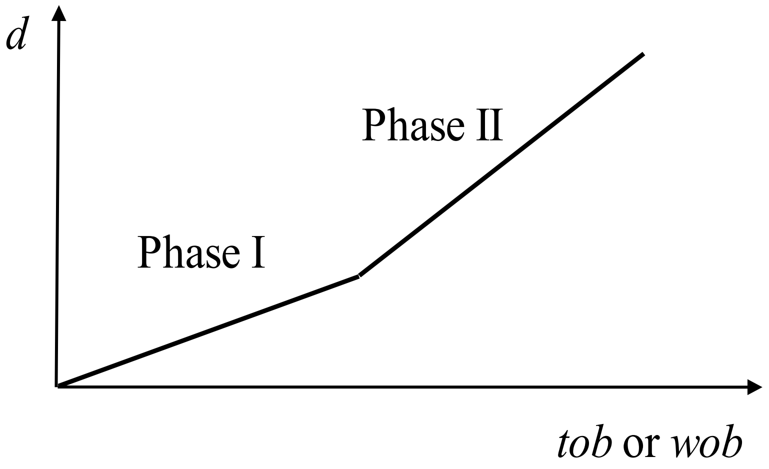

(b)

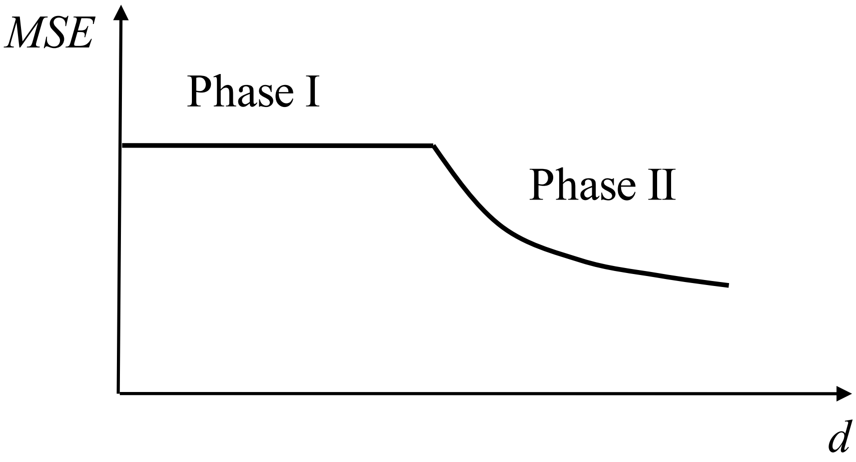

Figure 7.2 The performance of a drilling bit (a) general evolution of wob and tob over depth (b) general evolution of MSE over depth[16]

For a roller cone bit, Franca[13] derived a theoretical model. The general ideas are the same with the analytical model for the PDC bit: including the bit constant for the geometry of bit, the rate independent interface law between cutter and rock, the scaling of dynamic parameters between 3D and 2D models, and three phases in the drilling process[16]. Comparing with the PDC drilling bit in which cutters are fixed, the cutters are movable in the roller cone bi. Figure 7.3(a) shows a typical roller cone bit with three cones[118]. Due to the motion of cutters, the indentation introduced an extra process besides cutting and friction, as shown in Figure 7.3(b). The cutters on each cone are spirally placed along the radius of the bit, as shown in Figure 7.3(c), and it was simplified that all the cutters were aligned on one cone, as shown in Figure 7.3(d) [119]. The model also predicts the dependence of WOB and TOB on the ROP, and some laboratory tests were conducted under ambient pressure condition to support the model.

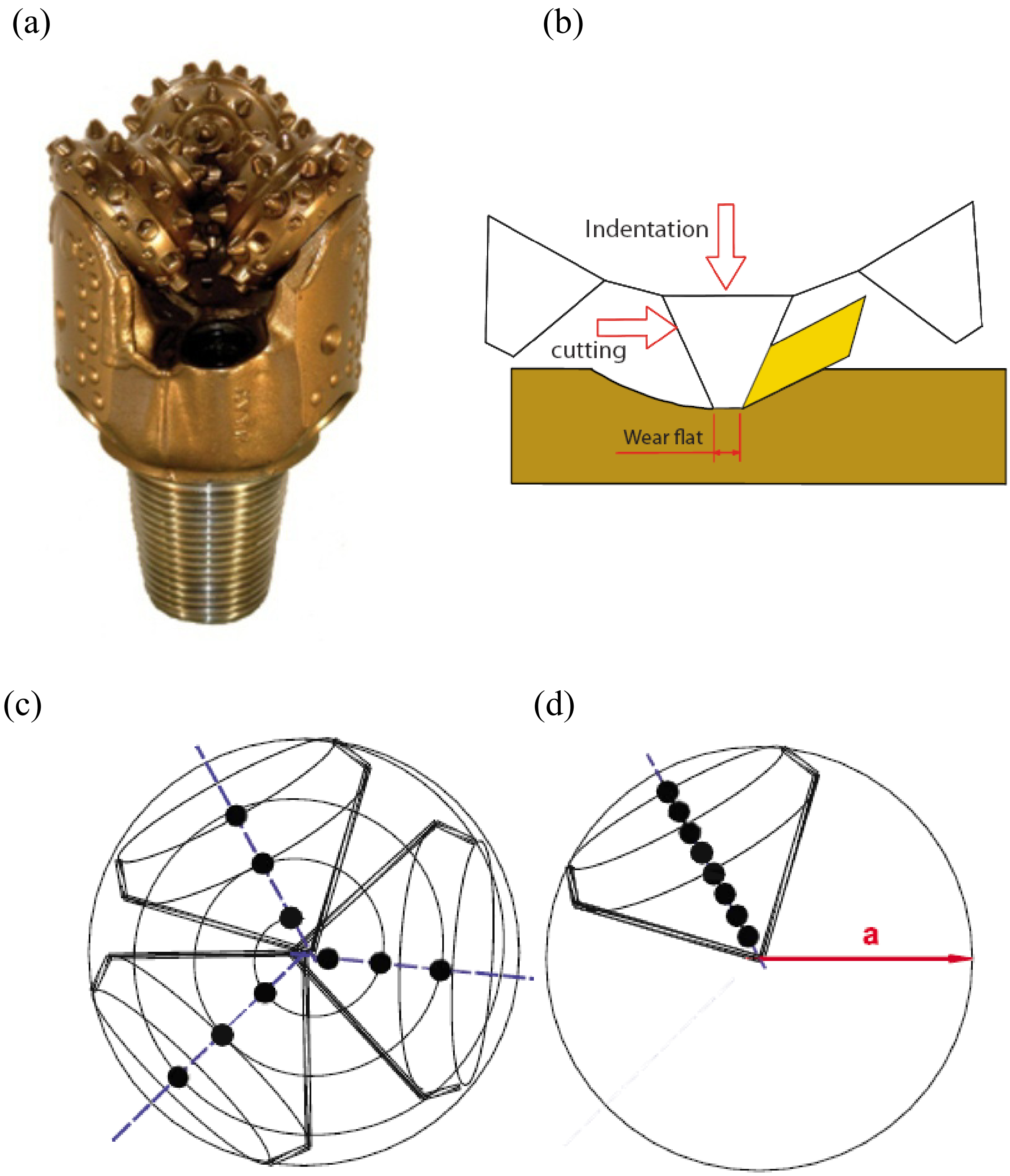

Figure 7.3 3D model for a roller cone bit (a) a real roller cone bit (b) three process for a roller cone bit (c) sketch of a roller cone (b) sketch of a simplied roller cone[13, 118, 119]

7.3 LABORATORY TESTS

Extensive laboratory tests of rock drilling under high pressure have been conducted by TerraTek [9]., and several factors were studied, including the influence of bit type, rock type, drilling mud, angular velocity. Figure 7.4 shows a layout of the test and several drilling bits used. Some typical results tested on Crab Orchard Sandstone under the confining pressure of 76MPa were analyzed here. The evolution of scaled *wob* and *tob* on depth per revolution is summarized in Figure 7.5, and the evolution of normalized MSE on depth is summarized in Figure 7.6.

The depths the laboratory tests carried out correspond to the first two phases as defined by the Detournay et al. model[16]. However, no clear boundary can be distinguished between phase I and phase II from the data. This implies that the transition from phase I to phase II is likely to be a gradual process. The *wob* and *tob* obtained did increasing with the depth, as predicted by the model. Within the likely range of phase I, the rates of increase in both *wob* and *tob* were nonlinear contrast to the linear assumption adopted in the model. Moreover, the MSE is obtained from the test results showed a steady decrease with depth in phase I range, instead of being constant as predicted in the model. A follow up investigation at this point would be worthwhile undertaking.

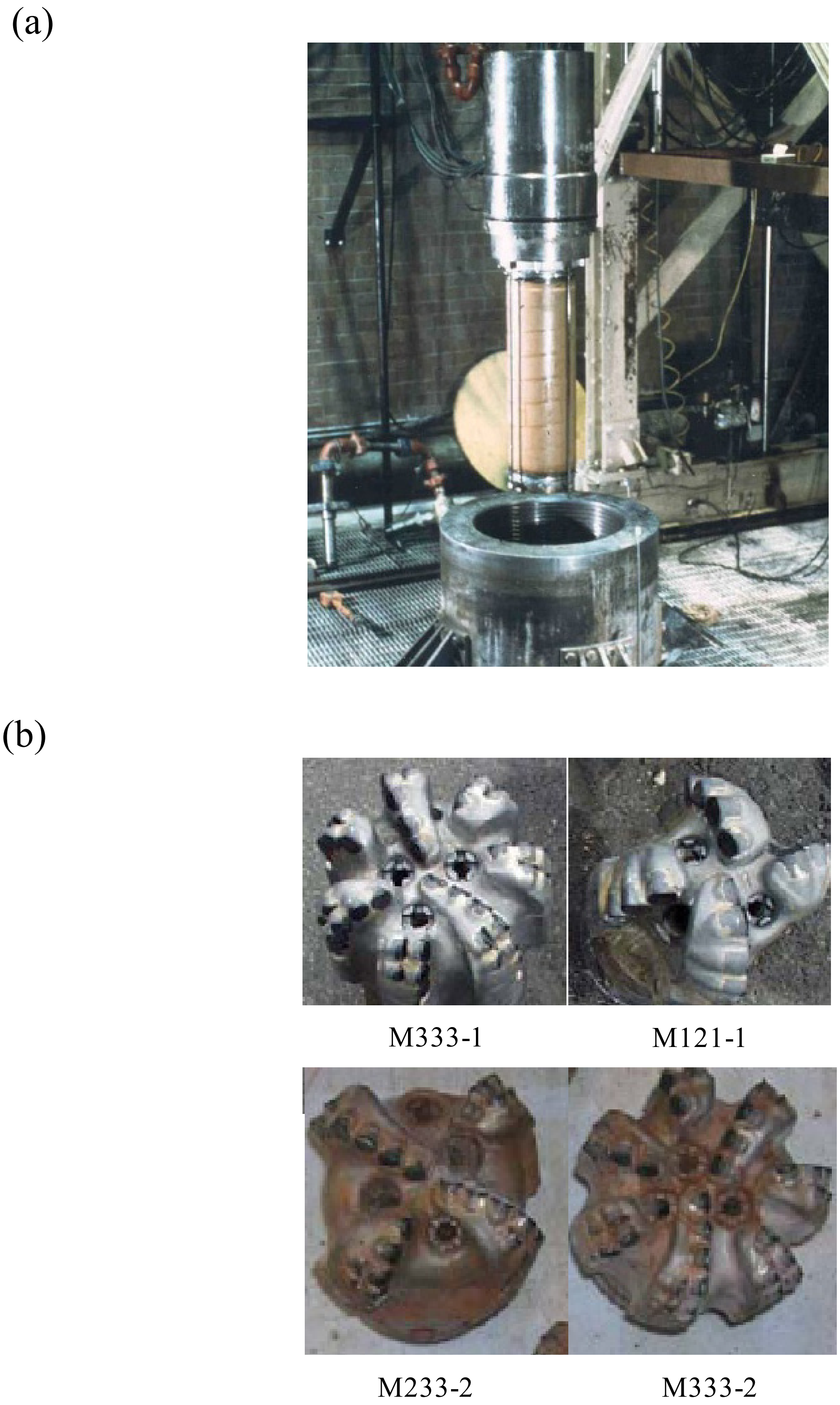

Figure 7.4 Laboratory drilling test under high pressure by TerraTek (a) Experiment set up (b) four typical PDC bits used in the test[9]

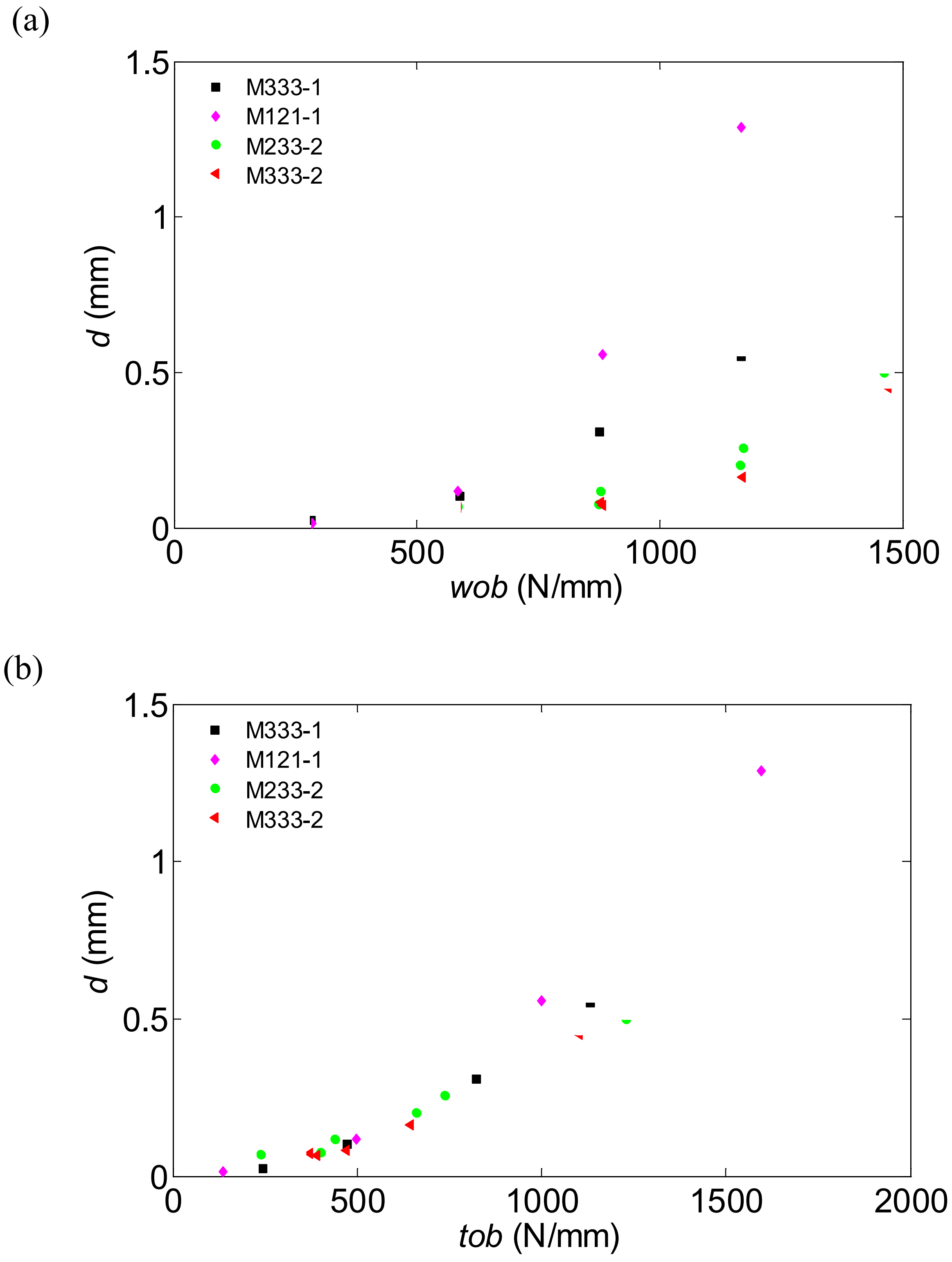

Figure 7.5 Laboratory test result of rock drilling under high pressure (a) relation between *wob* and *d* (b) relation between *tob* and *d*[9]

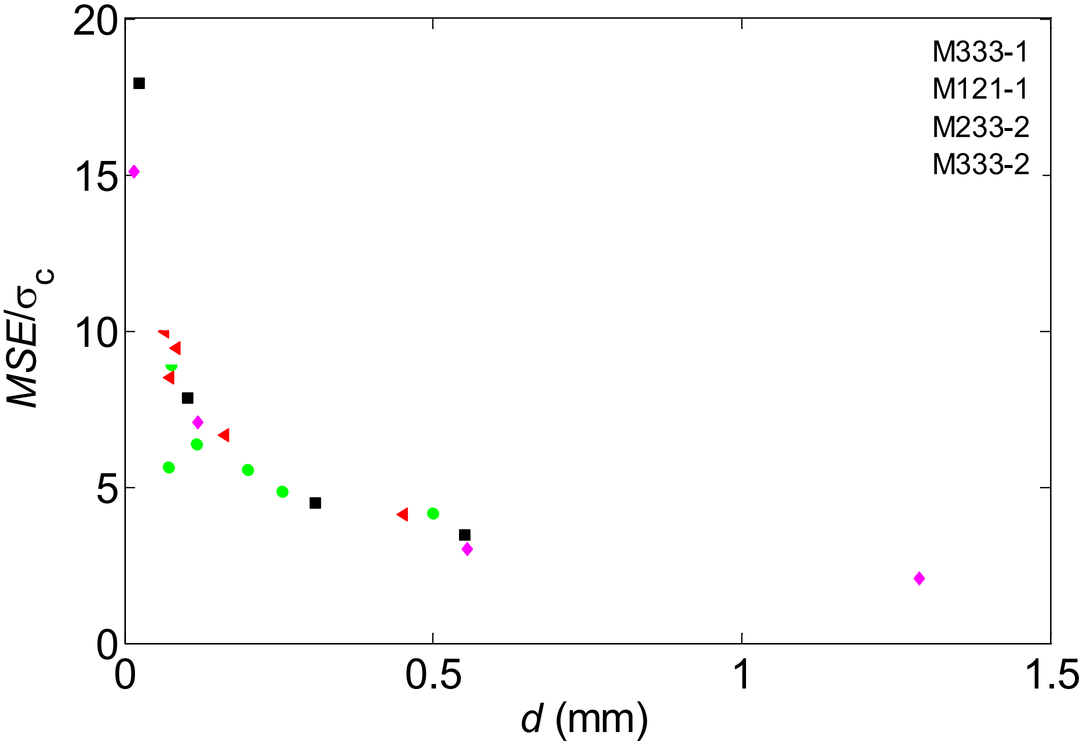

Figure 7.6 Relationship between normalilzed *MSE* and *d* in laboratory drilling test under high pressure[9]

7.4 NUMERICAL MODELING

The mechanics between the rock and a full drilling bit is one of the main objectives in this study. Due to the complexity of this problem, this study considers only the ambient pressure pressure condition should be deemed as only at the early phase of modeling the mechanics of rock drilling by a full PDC bit.

In this study, a drilling bit model is built following the design as presented in Figure 7.1 (a) as a base. The diameter of a PDC drilling bit typically ranges from 75 to 900mm, and a much scaled down model was built in for FEM analysis to save computation cost, as showed in Figure 7.7. The full drilling bit model was composed of several single disc cutters and blades on which the cutters are mounted. The diameter of the bit was 12mm, and the diameter of a single cutter is 1.45mm. Each cutter makes a 15^{o} rake angle from vertical. The cylindrical rock model and initial set up is illustrated in Figure 7.8(a). The diameter and height of the cylindrical rock sample were set to be 14mm and 4mm, respectively. The average FEM mesh size for the rock was finer within the depth of interest and the mesh size was around 0.27mm. Altogether 160,114 elements were employed for the rock and 6,799 elements were employed for the drilling bit.

Two different boundary conditions could be applied to this virtual drilling bit, namely, the kinematic controlled boundary, and the weight-on-bit controlled boundary. In the kinematic controlled boundary, the ROP and angular velocity Ω were imposed, and the TOB and WOB were measured; while in the weight-on-bit controlled boundary, the angular velocity Ω and WOB were imposed, and the TOB and ROP were measured[16]. Kinematic controlled boundary was preferred as it was more sTable[16], thus it was adopted in the present computation.

In the analysis, the bit moved along a helical trajectory. This is achieved by pushing downward at a velocity of 0.5mm/ms and at the same time rotating at an angular velocity Ω of 4rad/ms. This resulted in a ROP of 0.79mm per revolution. A snapshot of damage in the rock during the drilling process is showed in Figure 7.8(b). The resulting WOB and TOB computed for one revolution were shown in Figure 7.9.

One significant drawback of the study was that the FEM mesh was not dense enough, in that a cutter might only in contact with about four elements, while in the circular groove cutting studty 70 elements were in contact with the cutter. Thus a follow up study using super computer will be necessary to get quantified results.

Additionally, several simplifications were used in the preliminary modeling of rock cutting. The cutters were ideally sharp without wear flat. The model cutting was carried out under ambient pressure condition, without considering the typical HTHP in real drilling. The bit was a small scale model, how to scale the problem still needs further study.

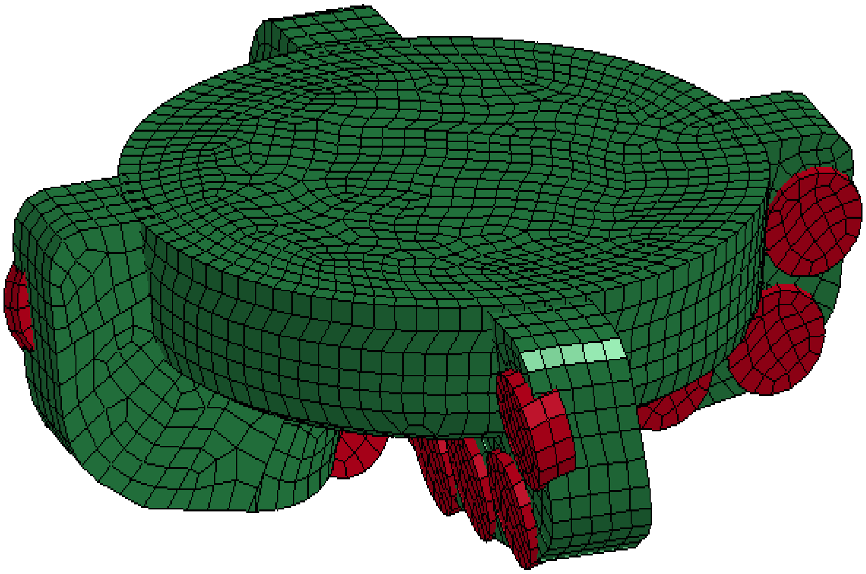

Figure 7.7 The modeled small scale drilling bit

(a)

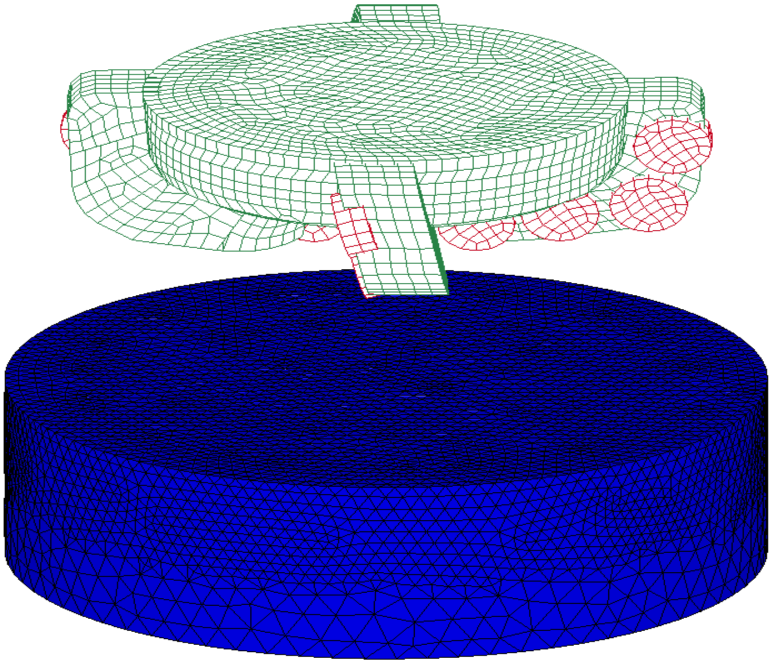

(b)

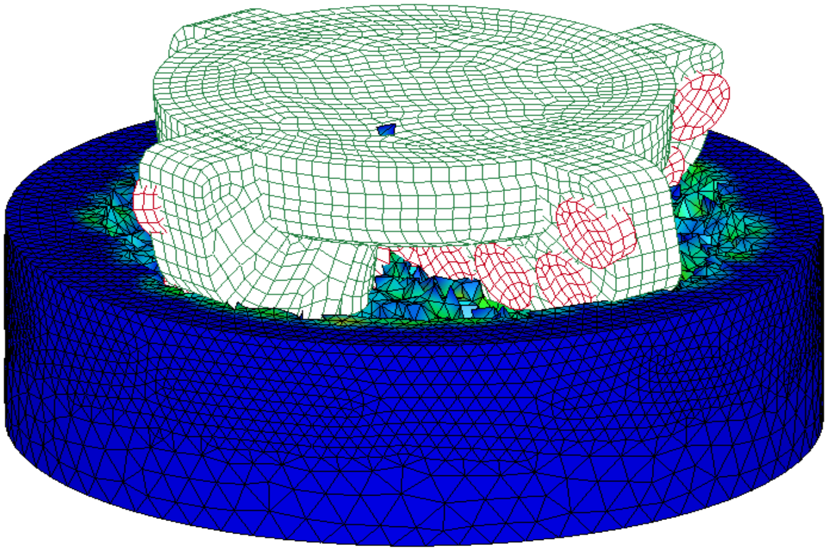

Figure 7.8 Drilling by a full drilling bit (a) geometry and mesh (b) a snapshot of damage during the drilling process

(a)

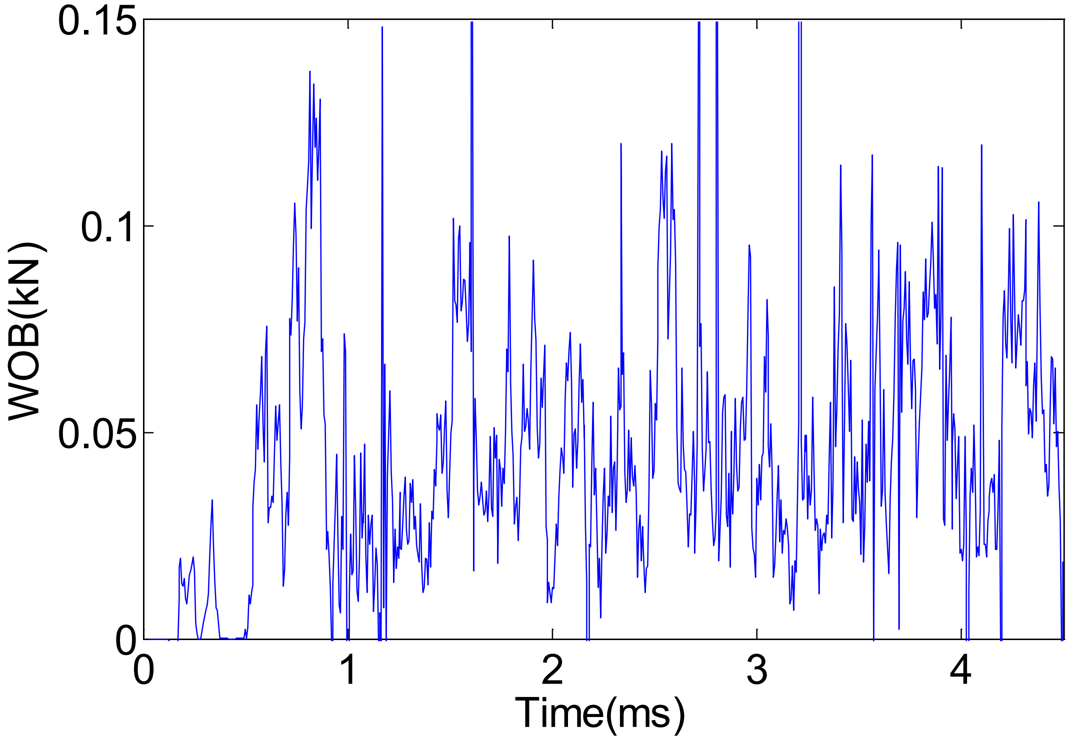

(b)

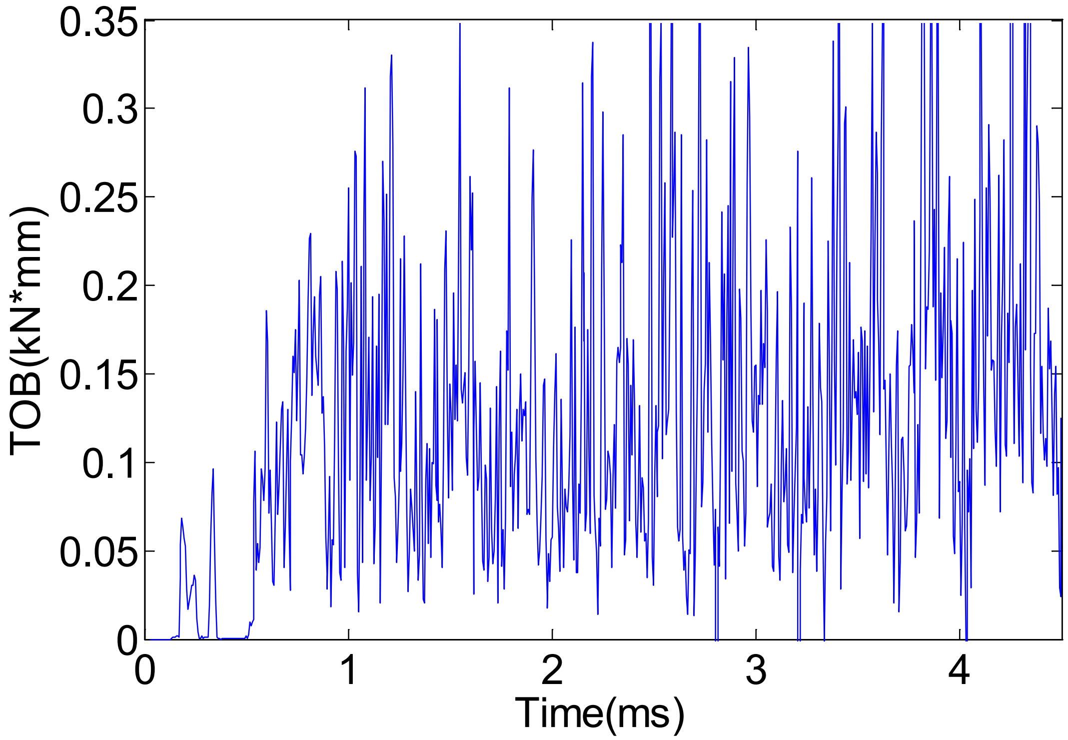

Figure 7.9 Modeled response of drilling bit under kinematic boundary condtion (a) WOB (b) TOB

7.5 CONCLUSIONS

Literatures shows extensive works have been done understand the mechanics of drilling bit, with analytical methods and physical tests. The available analytical models presently some limitations, because they are typically derived based on the mechanics of a single cutter while neglecting the interaction among cutters. The simplifications introduced in the analytical models also lead to some discrepancies compared with physical tests. Physical tests are a good way to study the performance of a full bit, but it is too expensive. Numerical simulation offers many benefits in studying this complicated problem. This study demonstrated the feasibility of such effort, but much work is still required before the modeling results can represent a real drilling process.

It is conceivable that a good way to study the complicated mechanism of the bit rock interaction would be to combining the advantages of all these methods.

8.0 CONCLUSIONS

8.1 MAIN CONTRIBUTIONS

The main contributions in this study are presented below.

(1)This study built on the Jaime's damage-based Finite Element Method(FEM) modeling of rock cutting. Based on previous experiences on linear rock cutting by a single Polycrystalline Diamond Compact(PDC) cutter, this study first extended the modeling to the circular cutting by a single cutter, then further initiated the modeling of rock drilling by a full drilling bit with multiple cutters.

(2)The FEM modeling has been shown to reproduce an important feature observed in laboratory test, namely, the MSE obtained approximately is equaled to the uniaxial compressive strength in the ductile mode in groove cutting when the cutter width to cutting depth ratio was large.

(3) The damage model in crack modeling has been shown to be compatible with the cohesive model in the modeling of the size effect of quasibrittle materials under mode I loading. The damage model was also successfully used to model the size effect of rock cutting under general setting.

(4) Using the cutting depth as a measure of size, Bažant's simple size effect law was shown to interpret the failure mode transition process in rock cutting well.

(5) The characteristic length is known to be linked to the critical transition depth, and its influence on the critical depth is studied through FEM modeling. Further, guided by FEM modeling results, few test data and some empirical equations, a relationship defining the critical depth as a function of the unconfined compression strength was derived.

(6) A simple model on the relationship between MSE and ROP was derived on ductile mode of cutting with the inclusion of the evolution of cutter wear, and it has been used to interpret the results in cutting high strength rock under high pressure.

8.2 FUTURE WORK

Recommendations for future work are presented herein.

(1) As the current analytical models in rock cutting are either focusing on ductile mode or on brittle mode, there has been a lack of a unified model. Based on the finding of this study that Bažant's simple size effect law fits well with all the data both in numerical simulation and in laboratory test, it might be feasible to develop a simplified analytical model covering the whole spectrum of cutting depths of interests. This would be a desirable undertaking for future work.

(2)The crack propagation in rocks is a complex problem, and even the fundamentals on the shear and compression fractures are not well understood. With the advance in the singularity modeling, a numerical study that differentiates the merits of different fracture criteria would be useful and timely. Such type of study has the potential of clarifying the ambiguities of defining damage in three-dimensional stress space.

(3)Since the deep oil drilling is carried out in High Temperature and High Pressure (HTHP) environment, research in such area is in urgent need. Even though there is solid laboratory evidence that the MSE is also related to the compressive strength at a high pressure environment as the study has shown, the data points are simply too few to make sound conclusion. Research on HTHP cutting test would cast light on a better understanding of the underlying mechanics, and also on the adequacy of the numerical tool including the present damage model.

(4) Clearly, the current analytical model relating the Mechanical Specific Energy(MSE) and Rate of Penertarion(ROP) for a full PDC drilling bit has room for improvement. It is essentially important to revisit the assumptions to improve the model.

(5) A small scale drilling bit model was presented in this study. Even with 160,114 elements employed in the rock sample, a much larger number of elements are needed for the analysis. A follow up study using high speed supercomputer is needed. Also, it is not clear how the model would be scaled up, and an investigation in this respect is desirable. An immediate extension would be to study the impact of the drilling rod and its transmission of force and moment to the drilling bit. To study the effect of drilling fluid and drilling pressure, however, may require the work to be carried out in an FEM-based program where the source code can be manipulated. This poses a hurdle that might not be easily overcome. On the other hand, a decouple approach, linking one fluid mechanics code with one solid mechanics code, would be feasible. This would be worthwhile endeavor until a fully coupled code can be developed.

BIBLIOGRAPHY

1. Dupriest, F.E. and W.L. Koederitz, Maximizing drill rates with real-time surveillance of mechanical specific energy, in SPE/IADC Drilling Conference. 2005: Amsterdam, the Netherlands.

2. Glowka, D., *Use of single-cutter data in the analysis of PDC bit designs: part 1- development of a PDC cutting force model.* Journal of Petroleum Technology, 1989. **41**(8): p. 797-799.

3. Chaput, E., *Observation and analysis of hard rocks cutting failure mechanisms using PDC cutters*. 1991, Imperial college of science.

4. Nicodeme, P., *Transition between ductile and brittle mode in rock cutting*, in *Rapport de stage d'option scientifique*. 1997, Ecole Polytechnique.

5. Richard, T., et al. *The scratch test as a means to measure strength of sedimentary rocks*. in *SPE/ISRM Rock Mechanics in Petroleum Eng. Conference*. 1998. Trondheim, Norway.

6. Richard, T., *Determination of rock strength from cutting tests*. 1999, University of Minnesota: Minneapolis, MN.

7. Dagrain, F., E. Poyol, and T. Richard. *Strength logging of geomaterials from scratch tests*. in *Proceedings of the Rock Engineering Theory and Practice*. 2004.

8. Kaitkay, P. and S. Lei, *Experimental study of rock cutting under external hydrostatic pressure.* Journal of Materials Processing Technology, 2005. **159**: p. 206-213.

9. TerraTek, *Improving deep drilling performance*. 2008, TerraTek company: Salt Lake City.

10. Zhang, W., et al. *The Initial Single Cutter Test of the NETL Ultra Deep Drilling Simulator*. in *45th US Rock Mechanics/Geomechanics Symposium*. 2011.

11. Hamrick, T.R., B. Kang, and W. Zhang. *Effect of elevated temperature and pressure on axial forces in rock drilling*. in *The 45th U.S. Rock Mechanics Symposium / Geomechanics Symposium*. 2011. San Francisco, CA, USA: Curran Associates, Inc.

12. Kerr, C., *PDC drill bit design and field application evolution.* Journal of petroleum technology, 1988. **40**(3): p. 327-332.

13. Franca, L.F., *Drilling Action of Roller-Cone Bits: Modeling and Experimental Validation.* Journal of Energy Resources Technology. Transactions of the ASME, 2010. **132**(4).

14. Nishimatsu, Y., *The mechanics of rock cutting.* Int J Rock Mech Min Sci & Geomechanics Abstracts, 1972. **9**(2): p. 261-270.

15. Detournay, E. and P. Defourny, *A phenomenological model for the drilling action of drag bits.* Int J Rock Mech Min Sci, 1992. **29**(1): p. 13-23.

16. Detournay, E., T. Richard, and M. Shepherd, *Drilling response of drag bits: theory and experiment.* Int J Rock Mech Min Sci, 2008. **45**(8): p. 1347-1360.

17. Atkins, A., *The science and engineering of cutting: the mechanics and processes of separating, scratching and puncturing biomaterials, metals and non-metals*. 2009: Butterworth-Heinemann.

18. Atkins, A., *Modelling metal cutting using modern ductile fracture mechanics: quantitative explanations for some longstanding problems.* International Journal of Mechanical Sciences, 2003. **45**(2): p. 373-396.

19. Huang, H. and E. Detournay, *Intrinsic length scales in tool-rock interaction.* International Journal of Geomechanics, 2008. **8**(1): p. 39-44.

20. Tulu, I. and K. Heasley. *Calibration of 3D Cutter-Rock Model With Single Cutter Tests*. in *in The 43th U.S. Rock Mechanics Symposium & 4th U.S. - Canada Rock Mechanics Symposium*. 2009. Asheville, North Carolina.

21. Guo, H., *Rock cutting using fracture mechanics principles*. 1990, University of Wollongong.

22. Huang, H., *Discrete element modeling of tool-rock interaction*. 1999, University of Minnesota.

23. Mendoza, J.A., *Modeling rock cutting using DEM with crushing particles*. 2010, University of Pittsburgh.

24. J-S Lin, et al., *Numerical modeling of rock cutting*, in *12th ISRM Congress*. 2011: Beijing, China.

25. Saouma, V.E. and M.-J. Kleinosky. *Finite Element Simulation Of Rock Cutting: A Fracture Mechanics Approach*. in *The 25th U.S. Symposium on Rock Mechanics (USRMS)*. 1984. Evanston, IL: American Institute of Mining, Metallurgical, and Petroleum Engineers Inc.

26. Ingraffea, A.R., *Theory of crack initiation and propagation in rock.* Fracture mechanics of rock, 1987: p. 71-110.

27. Liu, H.Y., S.Q. Kou, and P.A. Lindqvist, *Numerical simulation of the fracture process in cutting heterogeneous brittle material.* International journal for numerical and analytical methods in geomechanics, 2002. **26**(13): p. 1253-1278.

28. Yu, B., *Numerical simulation of continuous miner rock cutting process*. 2005, West Virginia University: Morgantown,WV.

29. Jaime, M.C., et al. *Finite Element Modeling of Rock Cutting*. in *The 44th U.S. Rock Mechanics Symposium and 5th U.S.-Canada Symposium*. 2010. Salt Lake City, Utah, USA: Curran Associates, Inc.

30. Fontoura S.A.B.da, et al., *Rock mechanics aspcts of drill bit rock interaction*, in *12th ISRM Congress*. 2011: Beijing, China.

31. Teale, R., *The concept of specific energy in rock drilling.* Int. J. Rock Mech. Min. Sci., 1965. **2**: p. 57-73.

32. Gurney, C., Y. Mai, and R. Owen, *Quasistatic cracking of materials with high fracture toughness and low yield stress.* Proceedings of the Royal Society of London. A. Mathematical and Physical Sciences, 1974. **340**(1621): p. 213-231.

33. Puttick, K.E., *The correlation of fracture transitions.* Journal of Physics D: Applied Physics, 1980. **13**(12): p. 2249-62.

34. Irwin, G.R., *Fracture.* Encyclopaedia of physics, 1958. **VI**.

35. Bažant, Z.P., *Size effect in blunt fracture: concrete, rock, metal.* Journal of Engineering Mechanics, 1984. **110**(4): p. 518-535.

36. Bažant, Z.P. and J. Planas, *Fracture and size effect in concrete and other quasibrittle materials*. 1997: CRC.

37. Che, D., et al., *Issues in Polycrystalline Diamond Compact cutter-rock interaction from a metal machining point of view—part II: bit performance and rock cutting mechanics.* Journal of Manufacturing Science and Engineering, 2012. **134**: p. 064002.

38. Palaniswamy, K. and W. Knauss, *On the problem of crack extension in brittle solids under general loading.* Mechanics today, 1978. **4**: p. 87-148.

39. Erdogan, F. and G. Sih, *On the crack extension in plates under plane loading and transverse shear.* Journal of basic engineering, 1963. **85**: p. 519.

40. Murray, Y.D., *User manual for LS-DYNA concrete material model 159*. 2007, U.S. Department of transportation, Federal Highway Administration Mclean.

41. Detournay, E. and A. Drescher. *Plastic flow regimes for a tool cutting a cohesive-frictional material*. in *Proceeding 4Th Int. Symp. On Numerical Methods in Geomechanics (NUMOG IV). Balkema: Rotterdam*. 1992.

42. Bažant, Z.P. and M.T. Kazemi, *Determination of fracture energy, process zone length and brittleness number from size effect, with application to rock and conerete.* International Journal of Fracture, 1990. **44**(2): p. 111-131.

43. Bažant, Z.P. and P.A. Pfeiffer, *Determination of fracture energy from size effect and brittleness number.* ACI Materials Journal, 1987. **84**(6).

44. Bažant, Z.P., R. Gettu, and M.T. Kazemi. *Identification of nonlinear fracture properties from size effect tests and structural analysis based on geometry-dependent R-curves*. in *International Journal of Rock Mechanics and Mining Sciences & Geomechanics Abstracts*. 1991: Elsevier.

45. Fathy, A.M., *Application of fracture mechanics to rocks and rocky materials*. 1992, Universidad Politecnica de Madrid: Madrid, Spain.

46. Bažant, Z.P. and M.T. Kazemi, *Size effect on diagonal shear failure of beams without stirrups.* ACI Structural Journal, 1991. **88**(3): p. 268-276.

47. Bažant, Z. and P. Pfeiffer, *Shear fracture tests of concrete.* Materials and Structures, 1986. **19**(2): p. 111-121.

48. Belytschko, T., Y.Y. Lu, and L. Gu, *Element-free Galerkin methods.* International Journal for Numerical Methods in Engineering, 2005. **37**(2): p. 229-256.

49. Lin, J.-S., *A mesh-based partition of unity method for discontinuity modeling.* Computer Methods in Applied Mechanics and Engineering, 2003. **192**(11): p. 1515-1532.

50. Hillerborg, A., M. Modeer, and P.E. Petersson, *Analysis of crack formation and crack growth in concrete by means of fracture mechanics and finite elements.* Cement and Concrete Research, 1976. **6**(6): p. 773-781.

51. Planas, J., G.V. Guinea, and M. Elices, *Generalized size effect equation for quasibrittle materials.* Fatigue & Fracture of Engineering Materials & Structures, 1997. **20**(5): p. 671-687.

52. Bittencourt, T., A. Ingraffea, and J. Llorca, *Simulation of arbitrary, cohesive crack propagation.* Fracture mechanics of concrete structures, 1990: p. 339-350.

53. Moës, N. and T. Belytschko, *Extended finite element method for cohesive crack growth.* Engineering Fracture Mechanics, 2002. **69**(7): p. 813-833.

54. Cusatis, G. and E.A. Schauffert, *Cohesive crack analysis of size effect.* Engineering Fracture Mechanics, 2009. **76**(14): p. 2163-2173.

55. Bažant, Z.P. and Q. Yu, *Size-effect testing of cohesive fracture parameters and nonuniqueness of work-of-fracture Method.* Journal of Engineering Mechanics, 2011. **137**(8): p. 580-588.

56. Bažant, Z.P. and B.H. Oh, *Crack band theory for fracture of concrete.* Materials and Structures, 1983. **16**(3): p. 155-177.

57. Hallquist, J.O., *LS-DYNA Keyword user's manual.* 2009, Livermore Software Technology Corporation: Livermore, CA.

58. Hibbit, K. and I. Sorenson, *ABAQUS Analysis User s Manual.* Links, 2005.

59. Diehl, T., *Using ABAQUS cohesive elements to model peeling of an epoxy-bonded aluminum strip: A benchmark study for inelastic peel arms.* 2006.

60. Turon, A., et al., *An engineering solution for mesh size effects in the simulation of delamination using cohesive zone models.* Engineering Fracture Mechanics, 2007. **74**(10): p. 1665-1682.

61. Tomar, V., J. Zhai, and M. Zhou, *Bounds for element size in a variable stiffness cohesive finite element model.* International Journal for Numerical Methods in Engineering, 2004. **61**(11): p. 1894-1920.

62. Béton, C.E.-I.d., *CEB-FIP model code 1990: design code. No. 213-214. .* 1993, Telford: Telford.

63. Atkinson, B.K. and P.G. Meredith, eds. *Experimental fracture mechanics data for rocks and minerals*. Fracture mechanics of rock, ed. B.K. Atkinson. 1987, Academic Press: London. 477-525.

64. Bésuelle, P., J. Desrues, and S. Raynaud, *Experimental characterisation of the localisation phenomenon inside a Vosges sandstone in a triaxial cell.* International Journal of Rock Mechanics and Mining Sciences, 2000. **37**(8): p. 1223-1237.

65. Hashida, T., *Fracture toughness evaluation and hydraulic fracturing of rock.* 1984, Tohoku University: Sendai, Japan.

66. Hashida, T. and H. Takahashi, *Simple determination of the effective Young's modulus of rock by the compliance method.* J. Test. Eval., 1985. **13**(1): p. 77.

67. Planas, J. and M. Elices, *Size effect in concrete structures: Mathematical approximations and experimental validation.* Cracking and Damage', edited by J. Mazars and ZP Bažant (Elsevier, London, 1989), 1988: p. 462-476.

68. Bažant, Z.P., M.T. Kazemi, and R. Gettu. *Recent studies of size effect in concrete structues*. in *Transactions of the tenth international conference on structural mechanics in reactor technology*. 1989.

69. Pastor, J., et al. *Nueva expresión del factor de intensidad de tensiones para la probeta de flexión en tres puntos*. in *Anales de Mecánica de la Fractura ('A new expression for the stress intensity factor of a three-point bend specimen', in Spanish.)*. 1995.

70. Gross, B., J.E. Srawley, and W.F. Brown, *Stress-intensity factors for a single-edge-notch tension specimen by boundary collocation of a stress function*. 1964, National aeronautics and space administration cleveland OH lewis research center.

71. Guinea, G., J. Planas, and M. Elices, *Correlation between the softening and the size effect curves.* In: Size Efect in Concrete Structures (Edited by H. Mihashi, H. Okamura and Z. P. Bagant), pp. 233-244. E&FN Spon, London., 1994.

72. Bažant, Z.P., *Instability, ductility, and size effect in strain-softening concrete.* Journal of the Engineering Mechanics Division, 1976. **102**(2): p. 331-344.

73. He, W., Y.F. Wu, and K.M. Liew, *A fracture energy based constitutive model for the analysis of reinforced concrete structures under cyclic loading.* Computer Methods in Applied Mechanics and Engineering, 2008. **197**(51–52): p. 4745-4762.

74. Carpinteri, A., et al., *Cohesive crack model description of ductile to brittle size-scale transition: dimensional analysis vs. renormalization group theory.* Engineering Fracture Mechanics, 2003. **70**(14): p. 1809-1839.

75. Camanho, P.P., C. Davila, and M. De Moura, *Numerical simulation of mixed-mode progressive delamination in composite materials.* Journal of composite materials, 2003. **37**(16): p. 1415-1438.

76. Dugdale, D., *Yielding of steel sheets containing slits.* Journal of the Mechanics and Physics of Solids, 1960. **8**(2): p. 100-104.

77. Petersson, P., *Crack growth and formation of fracture zones in plain concrete and similar materials*, in *Report TrBm21006.* . 1981, Lund Institute of Technology: Lund, Sweden: Division of Building Materials.

78. Xu, X.P. and A. Needleman, *Numerical simulations of fast crack growth in brittle solids.* Journal of the Mechanics and Physics of Solids, 1994. **42**(9): p. 1397-1434.

79. Planas, J. and M. Elices, *Shrinkage eigenstresses and structural size-effect.* Fracture mechanics of concrete structures, 1992: p. 939-950.

80. Hillerborg, A., *The theoretical basis of a method to determine the fracture energy Gf of concrete.* Materials and Structures, 1985. **18**(4): p. 291-296.

81. Irwin, G.R., *Analysis of stresses and strains near the end of a crack traversing a plate.* J. appl. Mech., 1957.

82. Hucka, V. and B. Das, *Brittleness determination of rocks by different methods.* Int J Rock Mech Min Sci & Geomechanics Abstracts, 1974. **11**: p. 389-392.

83. Jaime, M. and J.S. Lin, *Finite element modeling of rock cutting and its associated fragmentation process.* manuscript in preparation, 2013.

84. Whittaker, B., R. Singh, and G. Sun, *Rock Fracture Mechanics Principles,Design and Applications* Elsevier. 1992.

85. Li, V.C., ed. *Mechanics of shear rupture applied to earthquake zones*. Fracture mechanics of rock, ed. B.K. Atkinson. 1987, Academic Press: London. 351-428.

86. Shen, B. and O. Stephansson, *Modification of the G-criterion for crack propagation subjected to compression.* Engineering Fracture Mechanics, 1994. **47**(2): p. 177-189.

87. Gunsallus, K.L. and F. Kulhawy. *A comparative evaluation of rock strength measures*. in *Int J Rock Mech Min Sci & Geomechanics Abstracts*. 1984: Elsevier.

88. Bhagat, R.B., *Mode I fracture toughness of coal.* Geotechnical and Geological Engineering, 1985. **3**(3): p. 229-236.

89. Harison, J.A., B.O. Hardin, and K. Mahboub, *Fracture toughness of compacted cohesive soils using ring test.* Journal of geotechnical engineering, 1994. **120**(5): p. 872-891.

90. Haberfield, C. and I. Johnston. *Relationship between fracture toughness and tensile strength for geomaterials*. in *12th International Conference on Soil Mechanics and Foundation Engineering*. 1989. Rio de Janiero, Brazil.

91. Zhang, Z.X., *An empirical relation between mode I fracture toughness and the tensile strength of rock.* Int. J. Rock Mech. Min. Sci., 2002. **39**: p. 401-406.

92. Zhang, Z., et al., eds. *The relationship between the fracture toughness and tensile strength of rock* Strength theories: applications, development & prospects for 21st century, ed. M. Yu. 1998, Science Press: Beijing/NewYork. 215-9.

93. Khan, K. and N. Al-Shayea, *Effect of specimen geometry and testing method on mixed mode I–II fracture toughness of a limestone rock from Saudi Arabia.* Rock mechanics and rock engineering, 2000. **33**(3): p. 179-206.

94. Yu, Y., *Measuring properties of rock from the site of permanent shiplock in three Gorges project*. 2001, Yangtze River Scientific Research Institute

95. Nordlund, E., C. Li, and B. Carlsson, *Mechanical properties of the diorite in the prototype repository at. Aspo HRL-laboratory tests*, in *International Progress Report, IPR-99-25, SKB*. 1999.

96. Bilgin, N., S. Eskikaya, and T. Dincer. *The performance analysis of large diameter blast hole rotary drills in turkish coal enterprises*. in *2nd International Symposium on Mine Mechanization and Automation*. 1993.

97. Clark, G.B., *Principles of rock drilling.* 1979, Colorado School of Mines: Colorado.

98. Howarth, D., *Review of rock drillability and borability assessment methods.* Institution of Mining and Metallurgy Transactions. Section A. Mining Industry, 1986. **95**.

99. Howarth, D., *The effect of pre-existing microcavities on mechanical rock performance in sedimentary and crystalline rocks.* Int J Rock Mech Min Sci & Geomechanics Abstracts, 1987. **24**: p. 223-233.

100. Kahraman, S., *Rotary and percussive drilling prediction using regression analysis.* Int J Rock Mech Min Sci, 1999. **36**(7): p. 981-989.

101. Kahraman, S., *Correlation of TBM and drilling machine performances with rock brittleness.* Engineering Geology, 2002. **65**: p. 269-283.

102. Kahraman, S., C. Balcı, and N. Bilgin, *Prediction of the penetration rate of rotary blast hole drills using a new drillability index.* Int J Rock Mech Min Sci, 2000. **37**(5): p. 729-743.

103. Prasad, U. and H. Christensen, *Fracture Toughness of Rocks and its Use in Drill Bit Selection* in *AADE National Technical Conference and Exhibition*. 2005: Houston, Texas.

104. Schmidt, R.L., *Drillability studies: percussive drilling in the field*, in *Report of investigations 7984*. 1972.

105. Selim, A.A. and W.E. Bruce, *Prediction of penetration rate for percussive drilling*, in *Report of investigations 7396*. 1970.

106. Yagiz, S., *Assessment of brittleness using rock strength and density with punch penetration test.* Tunnelling and Underground Space Technology, 2009. **24**(1): p. 66-74.

107. Yarali, O. and E. Soyer, *The effect of mechanical rock properties and brittleness on drillability.* Scientific research and essays, 2011. **6**(5): p. 1077-1088.

108. Dagrain, F. and T. Richard, *On the influence of PDC wear and rock type on friction coefficient and cutting efficiency.* EUROROCK 2006: Multiphysics coupling and long term behaviour in rock mechanics, 2006.

109. Besson, A., et al., *On the cutting edge.* Oilfield Review, 2000. **12**(3): p. 36-57.

110. Appl, F., C.C. Wilson, and I. Lakshman, *Measurement of forces, temperatures and wear of PDC cutters in rock cutting.* Wear, 1993. **169**(1): p. 9-24.

111. Moseley, S., K.P. Bohn, and M. Goedickemeier, *Core drilling in reinforced concrete using polycrystalline diamond (PCD) cutters: Wear and fracture mechanisms.* International Journal of Refractory Metals and Hard Materials, 2009. **27**(2): p. 394-402.

112. Challamel, N. and H. Sellami, *Application of yield design for understanding rock cutting mechanism*, in *SPE/ISRM Rock Mechanics in Petroleum Engineering, 8-10 July 1998, Trondheim, Norway*. 1998.

113. Richard, T., C. Coudyzer, and S. Desmette. *Influence of Groove Geometry And Cutter Inclination In Rock Cutting*. in *The 44th U.S. Rock Mechanics Symposium and 5th U.S.-Canada Symposium*. 2010. Salt Lake City, Utah, USA: Curran Associates, Inc.

114. Zhou, Y., et al. *Modeling groove cutting in rocks using finite elements*. in *The 45th U.S. Rock Mechanics Symposium / Geomechanics Symposium*. 2011. San Francisco, CA, USA: Curran Associates, Inc.

115. Zhou, Y., et al. *Mechanical specific energy versus depth of cut*. in *The 46th U.S. Rock Mechanics Symposium / Geomechanics Symposium*. 2012. Chicago, IL, USA: Curran Associates, Inc.

116. Byerlee, J., *Friction of rocks.* Pure and applied Geophysics, 1978. **116**(4): p. 615-626.

117. Almenara, R. and E. Detournay. *Cutting experiments in sandstones with blunt PDC cutters*. in *Proceedings of the International Society of Rock Mechanics Symposium EuRock*. 1992.

118. Available from: http://www.trenchlessonline.com/index/webapp-stories-action?id=662.

119. Warren, T., *Factors affecting torque for a roller cone bit.* Journal of petroleum technology, 1984. **36**(9): p. 1500-1508.